

**Mechanical Coupling via the Membrane Fusion
SNARE Protein Syntaxin-1A: A Molecular Dynamics
Study**

Dissertation
zur Erlangung des Doktorgrades
der Mathematisch-Naturwissenschaftlichen Fakultäten
der Georg-August-Universität zu Göttingen

vorgelegt von
Volker Knecht
aus Kaiserslautern

Göttingen, 2003

D7

Referent: Prof. Dr. A. Zippelius

Korreferent: PD Dr. H. Grubmüller

Tag der mündlichen Prüfung: 28.03.2003

Bibliografische Information Der Deutschen Bibliothek

Die Deutsche Bibliothek verzeichnet diese Publikation in der Deutschen Nationalbibliografie; detaillierte bibliografische Daten sind im Internet über <<http://dnb.ddb.de>> abrufbar.

Dissertation, Universität Göttingen, 2003

ISBN 3-89820-521-5

Dieses Werk ist urheberrechtlich geschützt.

Alle Rechte, auch die der Übersetzung, des Nachdruckes und der Vervielfältigung des Buches, oder Teilen daraus, vorbehalten. Kein Teil des Werkes darf ohne schriftliche Genehmigung des Verlages in irgendeiner Form reproduziert oder unter Verwendung elektronischer Systeme verarbeitet, vervielfältigt oder verbreitet werden.

This document is protected by **copyright**.

No part of this document may be reproduced in any form by any means without prior written authorization of Mensch & Buch Verlag.

© MENSCH & BUCH VERLAG, Berlin 2003

Nordendstr. 75, 13156 Berlin • ☎ 030 - 45 49 48 66

<http://www.menshundbuch.de> • info@menshundbuch.de

Contents

1	Introduction	3
1.1	Membrane fusion	3
1.2	SNARE proteins	6
1.2.1	Fusion model	6
1.2.2	Structure of SNARE proteins	9
1.3	Mechanical coupling	11
2	Molecular Dynamics Simulation Methods	15
2.1	Principle	15
2.2	Computing Trajectories	19
2.2.1	Integration method and time step	19
2.2.2	Lipid and solvent environment	20
2.2.3	System boundaries	22
2.2.4	Temperature and pressure coupling	23
2.2.5	Improving efficiency	25
2.2.6	Minimization and equilibration	27
2.2.7	Accelerated traversing of energy barriers	28
2.2.8	Restraints	30
2.3	Analysis Methods	31
2.3.1	Analysis of individual snapshots	31
2.3.2	Thermodynamics: Free energy calculations	33

2.4	Statistical accuracy and significance	35
2.4.1	Analytical confidence estimates	37
2.4.2	Numerical confidence and significance estimates	40
3	Room Temperature Simulation Results	45
3.1	Pilot studies: absent and simplified lipid environment	45
3.2	Peptide with explicit lipid environment	49
3.2.1	Lipid environment	50
3.2.2	Peptide insertion	53
3.2.3	Modeling	53
3.2.4	Equilibration	54
3.2.5	Production runs	55
3.2.6	Linker stiffness	57
3.2.7	Effects of acidic lipids	58
3.2.8	Effects of prolongation	59
3.2.9	Linker embedding	60
3.2.10	Hydrogen bonds	62
3.2.11	Hydrophobic anchoring of the TM helix	62
3.2.12	TM helix tilt and structure	64
3.2.13	Immersion depths of individual residues	65
4	Simulated Annealing Results	69
4.1	Convergence	72
4.2	Linker stiffness	73
4.3	Linker structure	76
4.4	Effects of acidic lipids	78
4.5	Effects of prolongation	80
4.6	Hydrogen bonds	81
5	Summary	85

Chapter 1

Introduction

Membrane fusion is an essential step in synaptic transmission and all processes in eukaryotic cells that involve vesicular transport.¹ In all these cases membrane fusion is likely promoted by the so-called SNARE proteins, which form *trans*-complexes between the membranes.² It is an open question and controversially discussed^{3,4} whether the SNARE proteins just pin the membranes together, or, additionally, exert a force to the membranes, which induces local bending of the membranes towards each other. The present work (see also publication⁵) contributes to this discussion by means of molecular dynamics simulations.⁶

This chapter will give a brief introduction to SNARE-mediated membrane fusion and an overview to the studies carried out in this work. Sec. 1.1 describes the structure of membranes and the role of membrane fusion in the cell. A review on SNARE proteins is given in Sec. 1.2. Section 1.3 works out the questions addressed in this thesis and outlines the performed simulation studies.

1.1 Membrane fusion

Membranes are sheet-like structures, typically, 50 Å thick, that form closed boundaries around cells (plasma membrane) and the different compartments (organelles) of eukaryotic cells.¹ They are built up from molecules which consist of a water soluble (hydrophilic) and a water insoluble (hydrophobic) part. These *amphiphatic* molecules, when placed in water, spontaneously aggregate such that their hydrophilic parts are exposed to water, and their hydrophobic parts are hidden from water (see textbooks^{1,7}).

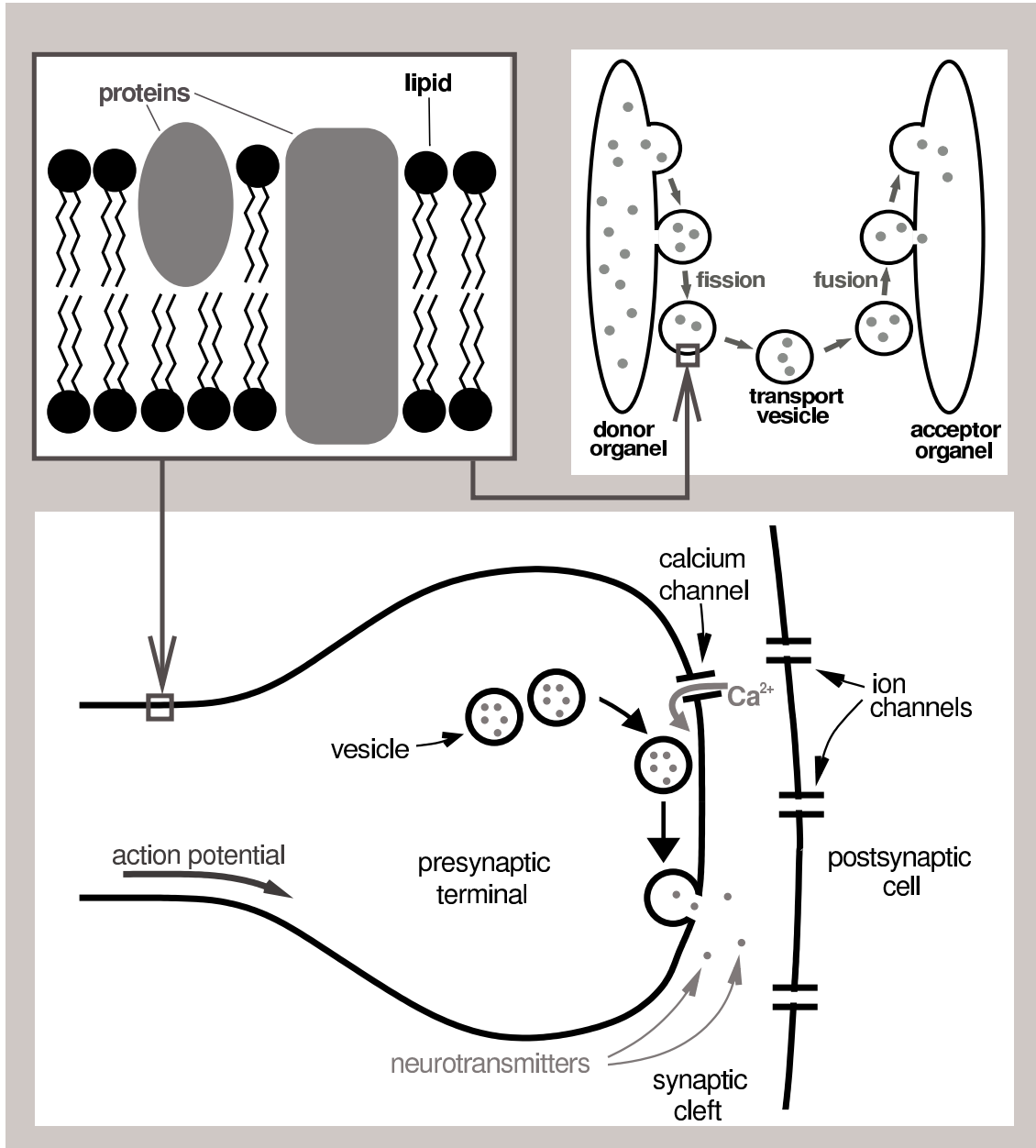


Figure 1.1: Molecular structure (*top left*) and topological transformations (*top right* and *bottom*) of biological membranes. The top right figure shows membrane fission and fusion in intracellular transport, the bottom figure indicates the role of membrane fusion in synaptic transmission. For explanations see text.

As sketched in Fig. 1.1 *top left*, the main constituents of biological membranes are lipids (*black*) and proteins (*gray*) which in biological membranes are found in weight ratios between 4:1 and 1:4.⁷ Most lipids in membranes are phospholipids. They consist of a polar, and therefore hydrophilic, headgroup (*black circles*), which can be zwitterionic or negatively charged, and two nonpolar, and thus hydrophobic,

hydrocarbon chains (fatty acid residuals). In aqueous solution, they aggregate to form bilayers.

Proteins are linear polymers of polar and nonpolar amino acid residues, linked together in a specific sequence which determines their three-dimensional structure (cf. Sec. 1.2.2).^{7,8} Membrane proteins are incorporated in membranes with their nonpolar surfaces buried within the hydrophobic core of the bilayer.

Membranes are often regarded as two-dimensional solutions of oriented lipid and protein molecules. It should, however, be noted that the different molecular species are not necessarily distributed homogeneously; domain formation is often observed and assumed to be important for the biological function of membranes.⁹

The merging of two membranes into a single one is an elementary process in the life of an eukaryotic cell. As shown in Fig. 1.1 *top right*, the transport of molecules (*gray circles*) from a donor to an acceptor organelle within the cell proceeds via membrane-bounded transport vesicles, which 'bud' from donor organelles, migrate to an acceptor organelle and fuse with the target membrane to inject their cargo into this organelle. The fusion of intracellular vesicles with the plasma membrane allows the release of molecules from the cell (exocytosis). These can be waste, cell products, or messenger molecules which transmit signals from one cell to another.¹

Special messenger molecules are neurotransmitters in chemical synapses (Fig. 1.1 *bottom*). As sketched in the figure, a chemical synapse is a contact site between two nerve cells (neurons) where the neurotransmitters transduce signals in one direction from the presynaptic to the postsynaptic cell. In the presynaptic terminal, a change in the electric potential between the intra- and the extracellular side of the plasma membrane, the action potential, induces the opening of calcium channels, and calcium influx triggers the fusion of synaptic vesicles with the plasma membrane. Thereby neurotransmitters are released into the synaptic cleft, diffuse towards the postsynaptic membrane, and dock to specific receptors. This triggers the opening of ion channels, and an action potential is created in the postsynaptic cell.

Obviously, it is essential for synaptic transmission that synaptic membrane fusion does not occur spontaneously, but is triggered by an action potential. More generally, the integrity of the cell and its individual compartments can only be maintained if membrane fusion is strongly controlled. Spontaneous fusion is prohibited by the general membrane structure: As soon as two membranes come into close proximity, i.e., within distances of a few Ångström, they strongly repel each other, mainly

because water tightly bound to the hydrophilic surface of the membrane must be displaced.¹⁰ Also the induced suppression of lipid protrusions and the strong interaction of negative lipid charges and lipid dipoles contribute to the repulsion.¹¹ Therefore, membrane fusion requires specific promoters.

1.2 SNARE proteins

A number of proteins have been identified as potential membrane fusion factors which operate in concert.^{12–24} In particular, SNARE proteins are likely key promoters for all intracellular membrane fusion events (see reviews^{2,23,25–42}).

The SNARE proteins that were identified first are involved in synaptic transmission. These are the best characterized members of this protein family. Specific sets of SNARE proteins have also been found in other vesicular transport pathways.^{26,30} SNAREs have remained highly conserved during evolution; they are present in all eukaryotic cells 'from yeast to man'.^{25,43}

Although it is unclear if additional proteins act after interference from the SNAREs, but before the native fusion event,^{40,42,44,45} SNAREs are the best candidates for effecting the fusion reaction.⁴¹ The current model of SNARE-mediated membrane fusion and respective experimental evidence are reviewed in more detail in Sec. 1.2.1. The structure of the SNARE proteins is described in Sec. 1.2.2.

1.2.1 Fusion model

The term 'SNARE (SNAP repceptor) proteins' was introduced to name the — initially unknown — targets of the soluble enzymatic protein NSF (N-ethylmaleimide sensitive factor), which is essential for transport vesicle fusion,^{12,13} and its co-factor SNAP (soluble NSF attachment protein).¹⁴ The SNAP receptors were purified from brain membrane fractions¹⁶ and identified as a set of three known proteins (see Fig. 1.2 *top I*): Synaptobrevin II (*gray*; henceforth called synaptobrevin), which is anchored in synaptic vesicle membranes,⁴⁶ SNAP-25 (synaptosome-associated protein of 25kDa, *light gray*), which is attached to the presynaptic membrane,⁴⁷ and syntaxin (*black*), which is concentrated in the zones of the presynaptic membrane at which synaptic vesicles dock.⁴⁸ Syntaxin also binds calcium-dependently to

the synaptic vesicle membrane protein synaptotagmin, the major calcium receptor for neuronal exocytosis.¹⁵

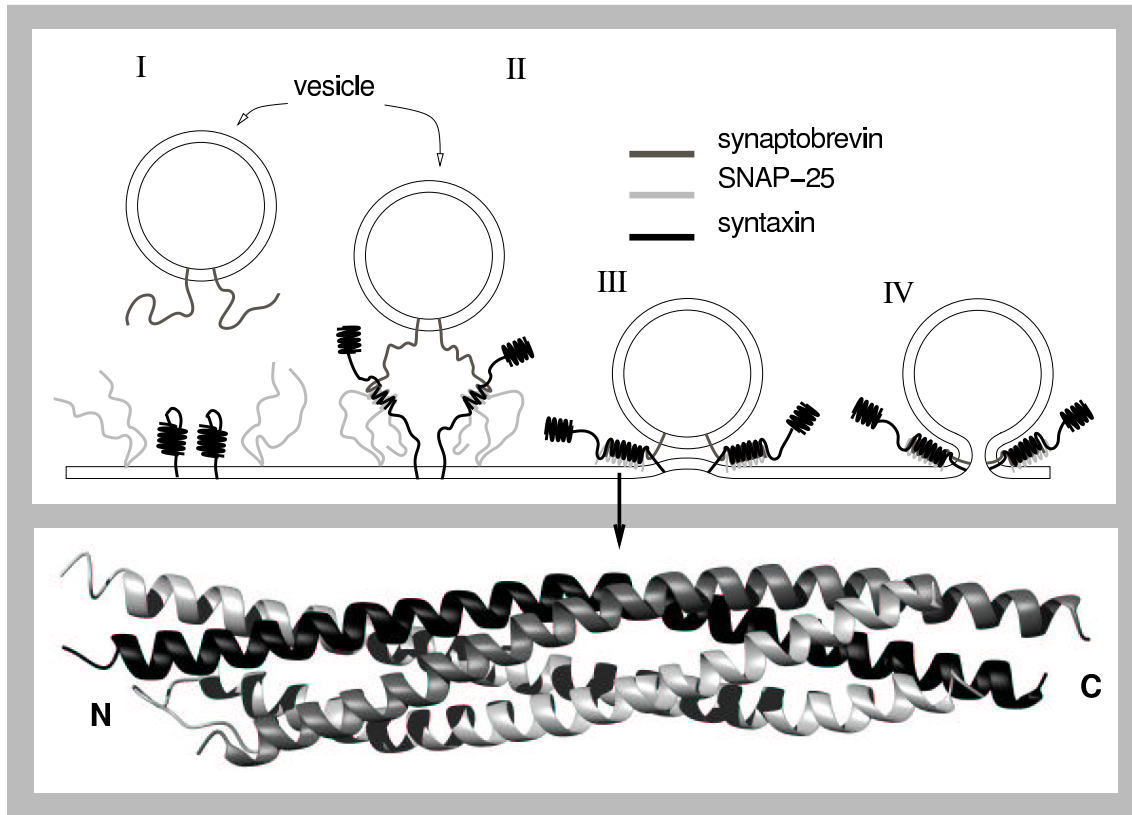


Figure 1.2: Function and structure of SNARE proteins. *Top*: Zipper model for SNARE-promoted membrane fusion. Syntaxin (*black*), SNAP-25 (*light gray*), and synaptobrevin (*gray*) assemble in a zipper-like fashion (*II*, *III*), thus pulling the vesicle towards the target membrane, until a fusion pore is created (*IV*). *Bottom*: X-ray structure of the synaptic SNARE complex in ribbon representation.

Independent evidence for the relevance of synaptobrevin, SNAP-25, and syntaxin for synaptic fusion came from the finding that their selective cleavage by the toxins tetanus and botulinum⁴⁹ inhibits neuronal exocytosis.⁵⁰ In squid nerve terminals, the cleavage of synaptobrevin by tetanus irreversibly blocked neurotransmitter release, while the number of synaptic vesicles increased.²⁷

Synaptobrevin, SNAP-25, and syntaxin form a complex (SNARE complex) with 1:1:1 stoichiometry before SNAP and NSF bind.⁵¹ As indicated in Fig. 1.2 *top I*, in their monomeric form, synaptobrevin (*gray*) and SNAP-25 (*light gray*) are unstructured,^{52–54} whereas syntaxin (*black*) shows significant content of helical structure.⁵² SNARE complexes form before Ca^{2+} -triggered membrane fusion.^{55,56} Upon com-

plex formation, helical structure is induced in synaptobrevin and SNAP-25, and the helicity of syntaxin increases (see Fig. 1.2 *top II, III*), and energy is released.⁵² In yeast homologs of the neuronal SNARE proteins, assembly begins distal to the membrane surfaces and proceeds towards them.⁵⁷ Each of the interacting domains exhibits seven-residue sequence repeats (heptad repeats) $a - g$ characteristic for helix bundles, in which the a and d positions generate a hydrophobic helical contact surface.⁵⁸ The SNARE complex forms a long rod of $120 - 140 \text{ \AA}$ length;⁵⁹ its two transmembrane (TM) anchors, contributed by syntaxin and synaptobrevin, both reside at the same end of the complex^{60,61} (see Fig. 1.2 *top, III*). The complex is disassembled upon consumption of ATP (adenosinetriphosphate) by NSF.⁵¹

For the *in vitro* fusion of artificial phospholipid bilayers with incorporated SNARE proteins (proteoliposomes) carried out by Rothman and co-workers, the presence of syntaxin/SNAP-25 and synaptobrevin in disjoined vesicle populations was required and sufficient for vesicle fusion monitored by lipid-⁶² and content-mixing.⁶³ This suggests that the SNARE proteins provide a minimal fusion machinery.

These findings also suggest that, upon SNARE complex formation, the membranes are pulled towards each other (see Fig. 1.2 *top*), and the released energy is used to promote the fusion process (zipper model of SNARE-mediated membrane fusion):^{26,27,42} In step I, the SNARE proteins are in their monomeric form; SNAP-25 and synaptobrevin are unstructured (random-coil-like), whereas syntaxin adopts a closed conformation* which is arrested by the protein nSec1 (*not shown*).^{20,38} In step II, nSec1 is released from syntaxin and syntaxin undergoes a conformational change.³⁸ Syntaxin, SNAP-25 and synaptobrevin assemble in a zipper-like fashion from the membrane-distant N- to the membrane-proximate C-termini; thereby the vesicle is pulled towards the plasma membrane.^{27,64} In step III, the SNARE complex is nearly completely formed, and the vesicle is tightly bound to the plasma membrane.²⁷ Several of these complexes are arranged in a circular array.⁶⁵ At this point, no fusion pore is observed yet; this state is arrested by synaptotagmin¹⁵ (*not shown*), which acts as a molecular clamp and prohibits the full assembly of the SNAREs close to the TM anchors.⁶⁶ In step IV, due to a change in the voltage between the intra- and the extracellular side of the plasma membrane, voltage-dependent calcium channels open. The inflowing calcium binds to specific binding sites of synaptotagmin,

*In the following “configuration of a protein” denotes an exactly determined spatial structure, i.e., a single point in the configuration space; “conformation” of a protein denotes a structure *ensemble* around an average structure.

which thereupon releases the SNAREs. Proceeding SNARE complex assembly finally promotes the formation of a fusion pore and thus membrane fusion. After fusion is complete, both TM domains of the SNARE complexes are anchored in the same membrane. These (*cis*-complexes) are disassembled by NSF and SNAP to enable the SNAREs to promote further fusion events.

1.2.2 Structure of SNARE proteins

Like all proteins (see textbooks^{7,8,67-69}), SNARE proteins are built up from amino acid residues (Fig. 1.3 *gray boxes*, 'aa') which are covalently linked to form polypeptide chains. Each residue consists of an amide (NH) and a carbonyl (CO) group, as well as a hydrogen and a C_α carbon atom, from which a side group (R_i) branches off. The atoms shown explicitly in Fig. 1.3 (*left*) form the backbone. The residues are connected via pseudo double bonds between the NH and CO groups (peptide bonds, *solid and dotted lines*), which force these groups into a planar conformation; only rotations around the (single) $N-C_\alpha$ and the $C_\alpha-C$ bonds (torsion angles ϕ and ψ , respectively) occur. Nature uses mainly twenty different amino acids; their side chains vary in size, shape, polarity, and charge.

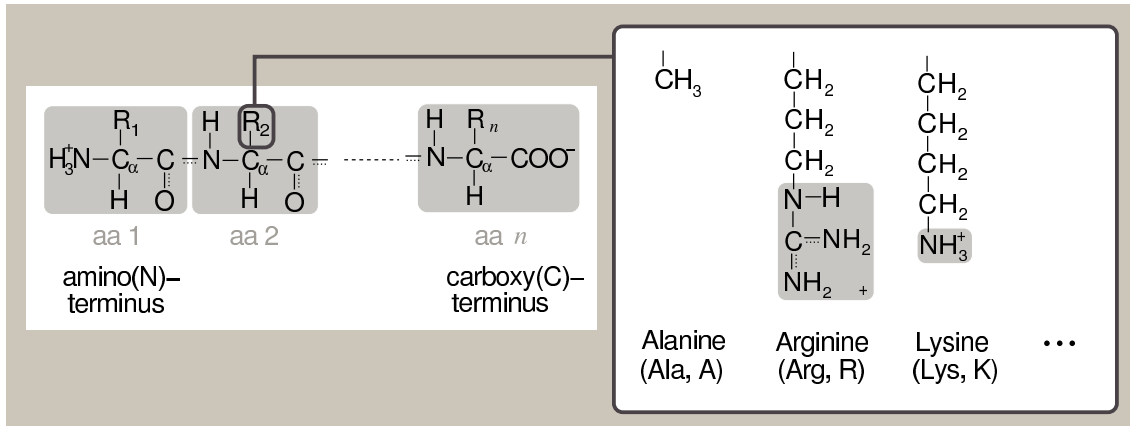


Figure 1.3: Chemical structure of proteins. The general structure is shown on the left. The side chains R_i of the amino acids alanine, arginine, and lysine, which play a central role in this work (see Sec. 1.3), are shown on the right. For arginine and lysine the gray boxes indicate the charged groups. There are 17 further normal amino acids in proteins, for which the side chains are not shown here.

Note that the amino(N)-terminus of the protein is a hydrogen acceptor (*base*); at neutral pH, which is the typical cytosolic pH, it binds an excess proton (NH_3^+), and

therefore is positively charged. Inversely, the carboxy(C)-terminus is a proton donor (*acid*) and, at neutral pH, releases a proton, thus being negatively charged (COO^-).

Fig. 1.2 *bottom* shows the structure of the cytosolic core of the synaptic complex of *rattus norvegicus*; it was resolved by x-ray crystallography,⁷⁰ is consistent with the results from the experimental and sequence studies mentioned above, and supports the sketched fusion model. In the figure, ribbons or thin strings indicate the backbone of the individual proteins (ribbon representation). This backbone is predominantly helical (*ribbon*), only short segments are unstructured (*strings*). Syntaxin (*black*) and synaptobrevin (*gray*) each contribute a single helix, whereas SNAP-25 (*light gray*) contributes two helices, to form a twisted four-helix bundle (four-stranded coiled-coil), with the N-termini ('N') of all helices residing at the same end of the complex. For each helix, the backbone winds around the respective helical axis from the N- to the C-terminus in a right-handed manner, and each backbone CO group (*not shown*) extends parallel to the respective helix axis, forming a hydrogen bond to the NH group four amino acids towards the C-terminus of the helix (right-handed α -helix). The side chains (*not shown*) extend to the outside of each helix.

Fig. 1.4 gives a more schematic view of the SNARE complex in the context of the fusion model and also shows regions of the proteins which are not present in the x-ray structure. The helices of the core complex are shown as long rectangles, synaptobrevin in magenta, SNAP-25 in blue, and the syntaxin core helix (H3 helix) in cyan. The two SNAP-25 helices are connected via a long loop (*blue line*) which is covalently attached to fatty acid chains inserted in the proximate lipid layer of the membrane.⁷¹ The N-terminal domain of syntaxin (Habc domain) (*not shown*) forms a three helix bundle which is connected to the H3 helix by an unstructured linker.³⁸

The hydrophobic TM anchors of the complex (*tilted rectangles*) contributed by syntaxin (*yellow*) and synaptobrevin (*magenta*) have been predicted from sequence analyses to consist of 19 (95–113) and 22 (266–287) residues and are assumed to be in α -helical conformation,⁷⁰ as the formation of helices allows to efficiently shield the polar NH and CO groups of the protein backbone from the hydrophobic environment.¹ With a predicted length of 28.5 and 33 Å, respectively, these helices are expected to fully span the hydrophobic core of the associated membrane.⁷⁰ The assumption that the TM domains are α -helical is also supported by the fact that in this conformation the TM residues of syntaxin and synaptobrevin essential for

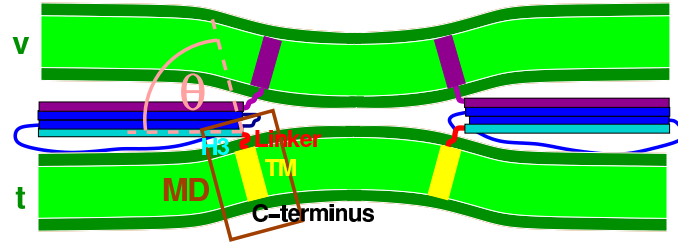


Figure 1.4: Fully assembled *trans*-complex formed by synaptobrevin (*magenta*) and SNAP-25 (*blue*), the H3 helix of syntaxin (*cyan*), a linker region (*red*), the transmembrane (TM) domains (*tilted rectangles*) of syntaxin (*yellow*), and synaptobrevin (*magenta*), which exerts mechanical force onto the vesicle (*'v'*) and the target (*'t'*) membrane and pulls them towards each other. Here the H3 helix tilt θ (*pink*) is studied by molecular dynamics (MD) simulations; the brown box marks the simulation system. The hydrophobic regions of the two membranes are colored green, their polar regions dark green.

homodimerization of these proteins form a continuous contact surface.⁷²

1.3 Mechanical coupling

Do SNARE proteins play a passive or an active role in membrane fusion? Do they just pin two membranes together, which eventually fuse spontaneously? Or do they exert additional forces upon the membranes which disturbs their local structure or locally bends them towards each other to promote their fusion? In the latter case, the TM anchors and, in particular, the anchor-proximate regions of the SNARE proteins would have to transduce the required energy from the cytosolic core complex into the membrane.

It has been suggested⁴ that the local membrane structure might be disturbed in the following way. For SNARE *trans*-complexes, inter-membrane repulsion will pull on the SNARE anchors and thereby displace them from the bilayer, dragging out associated lipids towards the contact area between the two bilayers; hydrophobic attraction of lipids from opposing layers⁷³ could then lead to the first interbilayer contact. This view is supported by the results of proteoliposome fusion experiments carried out by Rothman and co-workers (Sec. 1.2); in these experiments replacing TM domains of SNAREs by lipid anchors did not affect vesicle docking, but inhibited fusion, as long as the lipid anchors did not meet certain minimal hydrophobicity

requirements.⁴

It has further been proposed,⁶² that the membranes could be locally bend towards each other as shown in Fig. 1.4,⁶² assuming the local membrane plane remains nearly perpendicular to the TM anchor. This setting requires that the membrane-proximate regions of synaptobrevin (Fig. 1.4 *magenta*) and syntaxin (*red*, 'linker') are mechanically sufficiently stiff upon bending to conformationally couple the respective TM and cytosolic domains. In particular, the energy available for membrane juxtaposition is limited by the amount required to increase the H3 helix tilt angle θ (*pink*) from its equilibrium value to the one required for SNARE complex assembly. Thus, the mechanical flexibility of the linker is crucial for the fusion mechanism.

For synaptobrevin, the α -helical domain of the synaptic fusion complex x-ray structure ('core domain') extends into the TM domain by two residues; this suggests that core and TM domain form a continuous α -helix, which is expected to be stiff upon bending.⁷⁴ *Trans*-complex assembly would lead to significant strain within this helix. Membrane bending and final merger allowed the synaptobrevin helix to gradually relax to an unbent state.³

For syntaxin, the H3 helix is separated from the TM helix by a 5-residue linker (*red*) of unknown structure (residues 261–265). Its amino acid sequence reads ARKKK, where A stands for alanine, which is hydrophobic, R for arginine, and K for lysine. Both R and K are basic, and therefore, at neutral pH, positively charged. Fig. 1.3 *right* shows the side chains of these residues; for arginine and lysine, the gray boxes indicate the charged groups. The only information on the linker structure comes from recent spin-label EPR (electron parametric resonance)⁷⁵ measurements by Shin and co-workers⁷⁶ which provided some evidence for a partially unstructured linker. It is, however, possible that the linker mutations required for site-directed spin-labelling,⁷⁵ as well as the spin label itself, change the linker structure. Therefore, it is unclear if a similar mechanism holds for syntaxin as it does for synaptobrevin.

To study the role of the linker stiffness, Rothman and co-workers carried out *in vitro* fusion experiments in which they aimed to reduce the linker stiffness by inserting a five-residue sequence containing two tandem proline residues into the linker region.³ The proline disfavors the α -helical conformation due to sterical hindrance by its side chain which is linked to both the C_α and the nitrogen atom of the backbone;⁸ therefore it was assumed that the prolines would disrupt the hypothetical continuous H3-linker-TM helix.³ Indeed the proline mutation reduced the *in vitro* fusion rate,

but only by 50%.³

It should be noted that proteoliposome fusion occurs on timescales orders of magnitude longer than synaptic fusion,⁷⁷⁻⁷⁹ and therefore might involve a different mechanism.^{30,42} However, in a yeast vacuole fusion assay, a 6-residue insertion between the expected core and the TM domain of a syntaxin homologue also led to a 50% decrease in fusion efficiency.⁸⁰ A similar proline mutation of synaptobrevin had virtually no effect on the proteoliposome fusion rate.³

It is, however, unclear if the proline insertions actually reduce the linker stiffness. Apart from its helix-breaking character, proline can also rigidify the protein backbone; for proline-homopolymers, e.g., only the extended conformation of the backbone is sterically accessible.⁸

The results from the proteoliposome and yeast vacuole fusion experiments suggest that either a stiff linker is not required for fusion, or, alternatively, that sufficient conformational coupling can also be provided by a non-helical linker. The present work intends to discriminate between these two possibilities by means of molecular dynamics (MD) simulations. The method of MD simulations describes the dynamics of molecular systems by numerically integrating the Newtonian equations for all respective atoms. Such an atomistic description of the linker dynamics aims to (1) predict the linker helicity and (2) estimate the linker stiffness. In particular, it aims to (3) clarify if a possibly non-helical linker could also provide substantial conformational coupling.

Additional questions arose in the course of the study and were also addressed: (4) Which factors (e.g., lipid composition, environment, sequence) determine the mechanical properties of the linker? (5) Is the TM domain sufficiently perpendicular to the membrane plane as required for induced membrane-bending? (6) Is the TM domain anchored well enough within the membrane to withstand the high inter-membrane repulsion forces which tend to pull the TM domain out of the membranes?

To address these questions, we have carried out multi-nanosecond MD simulations of the relevant region (Fig. 1.4, *box*) comprising a C-terminal part of syntaxin (*cyan, red, and yellow*) embedded within a lipid bilayer (*green*) and explicit solvent environment (*not shown*).

A first guess for the linker helicity was obtained from free dynamics simulations at a physiological temperature (room temperature simulations), assuming that the protein in its native environment folds downhill on the free energy landscape. An

upper limit for the linker stiffness was estimated from the equilibrium fluctuations of the angle θ between the H3 helix and the bilayer normal (H3 helix tilt).

Additionally, to more efficiently sample the conformational space of the linker, annealing simulations were performed, starting from structures obtained from appropriately restrained high temperature simulations. From the resulting sets of final structures, the linker helicity was estimated; from the fluctuation of the H3 helix tilt angles, a lower bound for the linker stiffness was obtained.

To study effects of the lipid environment on linker helicity and bending stiffness, two different lipid compositions were chosen, yielding a neutral and an acidic (negatively charged) bilayer. Furthermore, a prolonged mutant created for a technical issue unexpectedly decreased the linker stiffness, and therefore was also studied systematically. For both the wild type and the mutant, as well as for both lipid compositions, room temperature as well as annealing simulations were performed.

The anchoring and orientation of the TM domain in the bilayer were studied in the room temperature simulations by analyzing the translation of the TM helix along the bilayer normal and its respective tilt.

The work is structured as follows: Chap. 2 lists the employed molecular dynamics simulation and analysis methods, including methods for confidence estimation and devised bootstrap hypothesis tests. Chap. 3 describes the room temperature, and Chap. 4 the annealing simulations. Finally, Chap. 5 summarizes the results of the work, discusses implications for the fusion model, and suggests experiments to validate the obtained results.

Chapter 2

Molecular Dynamics Simulation and Analysis Methods

The method of molecular dynamics (MD) simulation⁶ is used to describe the dynamics of systems comprising typically between 10^3 and 10^6 interacting atoms. In the present work, systems comprising between 14,000 and 22,000 atoms were simulated on timescales of several nanoseconds.

This chapter lists the employed MD simulation methods. After an introduction to the principles of MD simulations (Sec. 2.1), the used methods for calculation (Sec. 2.2) and analysis (Sec. 2.3) of MD trajectories are described.

2.1 Principle

To describe the dynamics of a molecular many-particle system exactly, the time-dependent Schrödinger equation

$$i\hbar\partial_t\psi(\mathbf{R},\mathbf{r},t) = \hat{H}\psi(\mathbf{R},\mathbf{r},t) \quad (2.1)$$

has to be solved, where \mathbf{r} and \mathbf{R} denote the electron and the nuclei positions, respectively, and the Hamilton operator \hat{H} describes the kinetic and potential energy of the system. Three approximation steps allow to solve this equation for systems of 10^3 – 10^6 atoms.⁸¹

1. Born-Oppenheimer approximation

The first step, the *Born-Oppenheimer Approximation*,⁸² exploits the fact that nuclei masses are three to four orders of magnitude larger than the electron mass and assumes that the electron wave function $\psi_e(\mathbf{r}; \mathbf{R})$ instantaneously follows the nuclei positions and thus obeys the time-independent Schrödinger equation

$$\hat{H}_e \psi_e(\mathbf{r}; \mathbf{R}) = E_e(\mathbf{R}) \psi_e(\mathbf{r}; \mathbf{R}), \quad (2.2)$$

where the nuclei positions enter only as parameters. Here the electron Hamilton operator

$$\hat{H}_e = \hat{T}_e + \hat{V}_{\text{NN}} + \hat{V}_{\text{Ne}} + \hat{V}_{\text{ee}} \quad (2.3)$$

is the sum of respective nuclei(N) and electron(e) interactions \hat{V} , and the kinetic contributions \hat{T}_e . The nuclei thus move in an effective potential given by the ground state energy $E_e(\mathbf{R})$ of Eq. 2.2; their motions thus follows the time-dependent Schrödinger equation

$$i\hbar \partial_t \psi_N(\mathbf{R}, t) = (\hat{T}_N + E_e(\mathbf{R})) \psi_N(\mathbf{R}, t). \quad (2.4)$$

2. Classical description of nuclei dynamics

In the second step, the dynamics of the nuclei is described in the classical approximation, i.e. Eq. 2.4 is replaced by the *Newtonian equations of motion* for classical point masses,

$$m_i \frac{d^2}{dt^2} \mathbf{R}_i = -\nabla E_e(\mathbf{R}_1, \dots, \mathbf{R}_N), \quad i = 1, \dots, N, \quad (2.5)$$

where m_i and \mathbf{R}_i denote mass and position of the i -th nucleus.

The classical description is a good approximation for non-bonded heavy atoms at room temperature. For light atoms or low temperatures, quantum effects become essential, such as the tunneling of hydrogen atoms and the superfluidity of liquid helium. But even the motion of heavy atoms at room temperatures is not properly described once they are involved in covalent or hydrogen bonds and thus oscillate in harmonic or quasi-harmonic potentials. For a harmonic oscillator, a classical description only holds when the thermal energy kT is much larger than the spacing $\hbar\omega$ of its discrete energy levels. At physiological temperatures (300 K), this condition is only fulfilled for vibration periods $\tau \gg 160$ fs. As can be seen from Tab. 2.1,

bond stretching and bond angle bending modes, as well as librations of water molecules* involve shorter vibration periods and, hence, are generally in the ground state. One consequence is that the energy exchange with the environment is usually overestimated in the classical description. The conformational motions of interest here, however, take place on picosecond⁸³ or longer timescales and can therefore be described well within classical mechanics.

type of vibration	T [fs]
bond stretching	10–24
bond angle bending	20–40
libration of water molecules	50–80
hydrogen bond stretching	170–700

Table 2.1: Typical vibration periods in molecules and hydrogen-bonded liquids.⁸⁴ Compare $h/kT = 170$ fs at 300 K.

Using the Born-Oppenheimer approximation and a classical description of nuclei dynamics allows to describe systems of several hundred atoms on timescales of about 10 ps.⁸⁵ Therefore studies like the present one require a further approximation.

3. Force field

In studies as the present one, where no chemical reactions are involved, the effective potential $E_e(\mathbf{R}_1, \dots, \mathbf{R}_N)$ in Eq. 2.5 can be approximated by a semi-empirical function, the so-called *force field*. It describes covalent forces caused by the change in length of a chemical bond (Fig. 2.1 A), the bending of an angle between two bonds (B), the out-of-plane deflection of aromatic carbon atoms (C), and the torsion of bonds (D, *dihedral terms*). The associated potentials are chosen harmonic (A – C) or periodic (D), respectively. Also non-covalent interactions are considered: A Lennard-Jones⁸⁶ potential (E) models the Pauli repulsion which prevents atoms from penetrating each other, and induced dipole attraction, collectively termed *van der Waals interactions*. The electrostatic interaction between partially charged atoms is described by the Coulomb potential (F). The total potential is the sum of all these individual interaction terms.

*rotational vibrations whose frequency is determined by the moment of inertia of a water molecule and forces working on this mode, which are mainly due to hydrogen bonds

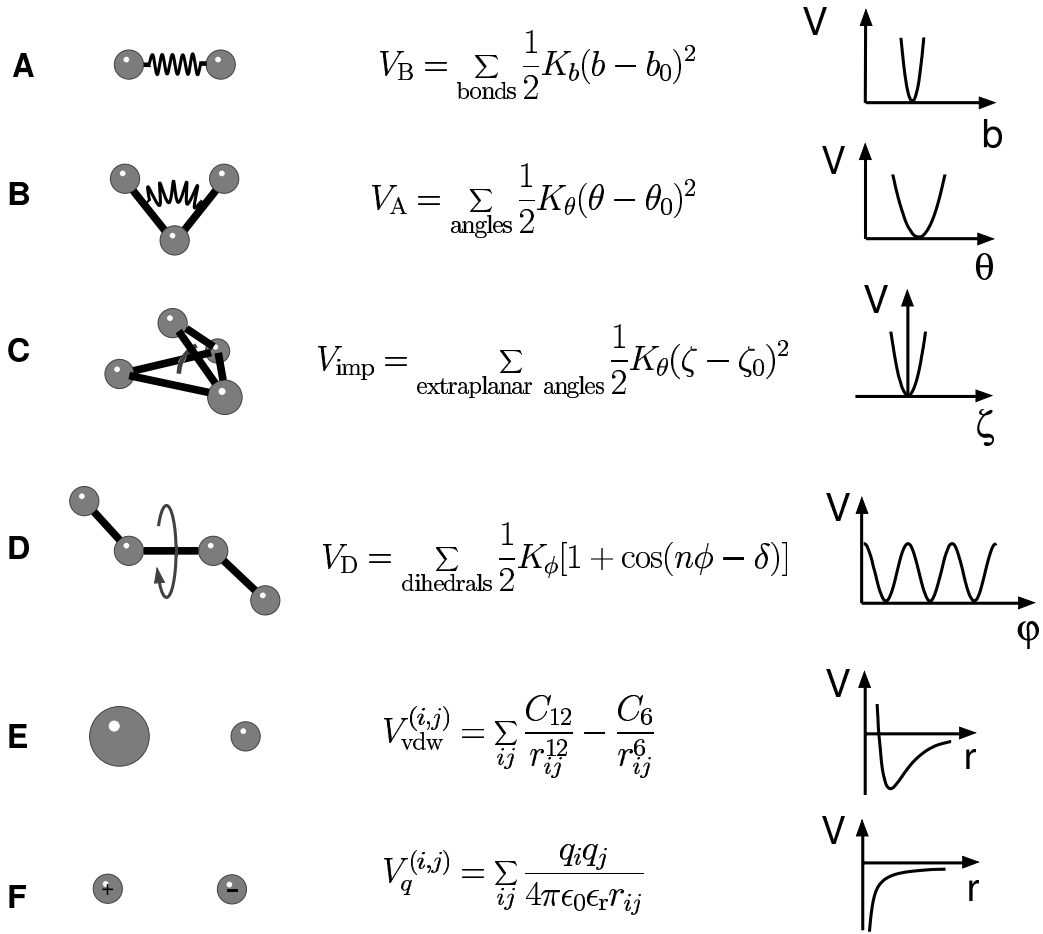


Figure 2.1: Energy contributions of a typical molecular dynamics force field. (A) bond-length and (B) bond-angle vibrations, (C) out-of-plane deflections of aromatic carbons, (D) the torsion of bonds, (E) van der Waals, and (F) Coulomb interactions. The respective inter-atomic interactions are illustrated on the left, the used energy terms are shown in the middle, and the functional dependencies are sketched on the right.

The parameters of the force field (Fig. 2.1), i.e., equilibrium values (b_i , θ_0 , ζ_0), force coefficients (K_i), Lennard-Jones parameters (C_{12} , C_6), and partial charges (q_i), are determined by a combination of *ab initio* calculations and by fitting to experimental data such as crystal structure, infrared spectra, free energies of solvation etc. in a self-consistent manner (see review⁸¹). The parameterization is done for small simple molecules regarded as the elementary building blocks of large molecules; in the case of proteins the parameters are optimized for individual amino acids and short peptides.

A series of different force fields has been developed (CHARMM,⁸⁷ GROMOS,⁸⁸

AMBER,⁸⁹ OPLS,⁹⁰ JUMNA,⁹¹ SPASIBA,⁹² CFF,⁹³ MM3,⁹⁴ etc.) which differ in the type of described molecules for which they are optimized and the number of considered degrees of freedom. In the present work, the GROMOS-87⁸⁸ force field was used with a small modification concerning the interaction between water-oxygen and carbon atoms.⁹⁵ It has been developed for the simulation of biomolecules in an explicit aqueous environment.

2.2 Computing Trajectories

Based on the methods introduced in the preceding section, MD trajectories were calculated numerically. All presented simulations were performed with the GROMACS simulation package,⁸⁴ version 2.1. The used methods are described in this section: Sec. 2.2.1 depicts the employed integration method. In Sec. 2.2.2, various ways to model the lipid and solvent environment of a protein are discussed, and the choice of the atomistic model is justified. The chosen boundary conditions are specified in Sec. 2.2.3. Sec. 2.2.4 describes how an isothermal/isobaric ensemble is generated. Sec. 2.2.5 sketches used techniques to improve the efficiency of MD calculations.

MD simulations usually imply a minimization and equilibration phase, whose relevance is explained in Sec. 2.2.6. To improve the conformational sampling, a method was used to accelerate the traversing of energy barriers (simulated annealing⁹⁶), as described in Sec. 2.2.7. Restraints which were imposed to stabilize the simulation system are described in Sec. 2.2.8.

2.2.1 Integration method and time step

The Newtonian equations (Eq. 2.5) are numerically solved iteratively in small time steps Δt . In the present work, the *leap-frog* algorithm⁹⁷ was employed. It is of second order in Δt and time-reversible, and preferable to second order Runge-Kutta methods,⁹⁸ as the expensive force calculation is only performed once per integration step. The algorithm calculates positions \mathbf{r} at time t and velocities \mathbf{v} at time $t - \frac{\Delta t}{2}$,

$$\mathbf{v}(t + \frac{\Delta t}{2}) = \mathbf{v}(t - \frac{\Delta t}{2}) + \frac{\mathbf{F}(t)}{m} \Delta t \quad (2.6)$$

$$\mathbf{r}(t + \Delta t) = \mathbf{r}(t) + \mathbf{v}(t + \frac{\Delta t}{2}) \cdot \Delta t \quad (2.7)$$

The time step Δt is typically chosen about a factor of ten smaller than the period of the fastest vibrations in the system. As mentioned in Sec. 2.1 these are bond-stretching vibrations with periods down to 10 fs, limiting Δt to 1 fs. Larger time steps are possible by, e.g., applying constraints, as described in Sec. 2.2.5. The discretized equations of motion 2.6 and 2.7 are modified to model the effect of a heat bath and to treat the system in the isobaric ensemble (Sec. 2.2.4).

2.2.2 Lipid and solvent environment

As will also be seen in this study, structure and dynamics — and hence the function — of a protein are strongly influenced by its environment,^{5,99,100} which therefore must be described thoroughly. In the presented simulations, the lipid and solvent environment of the protein was simulated explicitly (see Fig. 3.3). This involved high computational cost, requiring 98% of the total simulation time; hereof 70% was spent on the solvent environment. Available mean field models for membrane and solvent effects may save computational power, but suffer from severe limitations, as discussed in the following.

Implicit solvent models

Solvated proteins have the tendency to minimize their nonpolar surface, i.e., they tend to bury their hydrophobic residues in their interior; this *hydrophobic effect*¹⁰⁰ is also essential for the formation and the stability of lipid bilayers (Sec. 1.1). It has been modeled for proteins by energy terms proportional to the solvent accessible area of solute atoms or groups of atoms, respectively.^{101–106} Furthermore, the partial charges of a protein (or lipid headgroups) are screened from each other due to the alignment of water molecules; this effect has been described by a distance-dependent dielectric function $\epsilon_r(r)$ (cf. Fig. 2.1 *F*). Such implicit models, however, are inaccurate and thus may lead to wrong conformations of simulated peptides or proteins. To name an example, a model using surface area terms as well as a dielectric function¹⁰⁷ appears to artificially favor helices with backbone hydrogen bonds between residues i and $i + 5$, the — extremely rare — π -helices, over those with bonds between residues i and $i + 3$, the — very common — α -helices^{107,108} (Sec. 1.2.2).

Furthermore, ions in physiological concentrations lead to an additional dielectric screening. This effect has been described implicitly by solving the Poisson-Boltzmann (PB) equation at each point of the simulation system.^{109,110} The computational expense spent on solving the PB equation has been reduced by updating the potential only every 200 integration steps.¹⁰⁹ Comparisons of electrostatic potentials calculated by a finite-difference Poisson-Boltzmann approach, however, differed from potentials calculated from MD simulations with an explicit solvent environment by at least $0.4 \text{ kcal mol}^{-1} \text{ e}^{-1}$, likely reflecting the limited accuracy of the implicit model.¹¹¹

Implicit lipid models

Even more difficult than implicit solvent models are implicit lipid models; yet a number of models have been developed; see review.¹¹² Treating solvent and bilayer as a continuum, while choosing a dielectric constant of $\epsilon_r \approx 80$ for the aqueous phase, the low electrostatic screening of the bilayer core has been described by assigning $\epsilon_r \approx 2$ to a slab of about 30 \AA thickness.¹¹³ The discontinuous change of the electrostatic screening between the aqueous and the lipidic phase, however, yields a poor description of the interface. An appropriate smoothing function is recommendable, but to the author's knowledge has not been used yet.

The lipid headgroups and the water produce an electrostatic potential profile within the interface, which has been modeled by an appropriate mean field expression in the force field, derived by solving the one-dimensional Poisson-Boltzmann equation.¹¹⁴ The hydrophobicity of the bilayer has been described by assigning an energy to each protein atom defined as the free energy difference of the atom in lipid and in water;¹¹⁵ here the hydrophobicity was assumed to vary along the axis of the bilayer normal, with an exponential smoothing function in the interfacial region.

Available mean field models of lipid membranes, however, cannot describe the destabilization of internal hydrogen bonds of the peptide by hydrogen bond formation to the surrounding lipid headgroups, an effect which strongly affected the conformational and mechanical properties of the peptide studied in this work (see Chaps. 3 and 4); therefore the usage of an explicit bilayer model of the membrane was essential.

Chosen atomistic model

For the solvent environment, water was chosen, with the SPC (*simple point charge*) water force field.¹¹⁶ Also ions were added; their type (Cl^- or Na^+) and number were mostly chosen such as to compensate the net charge of the peptide-membrane system ('charge compensation'). In one case, excess ions were added and K^+ rather than Na^+ ions were used to mimic the intracellular conditions of typical mammalian cells,¹ and, in particular, to obtain a physiological concentration of $[\text{KCl}] = 0.154 \text{ M}$, ('intracellular salt conditions').

For the lipid environment, two mixtures of three typical phospholipid species were simulated, yielding a neutral and a negatively charged (acidic) bilayer (see Sec. 3.2.1).

2.2.3 System boundaries

When the solvent and lipid environment of the protein is simulated explicitly, appropriate boundary conditions have to be chosen to minimize artifacts from the system boundaries. Molecules can be prevented from evaporation by a 'wall' of atoms which are fixed¹¹⁷ or harmonically restrained at stationary positions. Alternatively, an appropriate boundary potential may be applied, which additionally counterbalances the surface tension.¹¹⁸ Atoms close to the wall layers were subjected to stochastic dynamics to account for the energy exchange with the environment.¹¹⁷

In the present work, short-range artifacts due to the special treatment of boundary regions were avoided by using *periodic* boundaries. These also facilitate pressure coupling (see Sec. 2.2.4). For periodic boundaries, the simulation volume represents a space-filling box which is surrounded by translated copies of itself. The box can be a cuboid, a dodecahedron, or a truncated octahedron. As asserted for Ewald summation of Coulomb forces (cf. Sec. 2.2.5), the periodicity of the system can introduce long-range artifacts such as the artificial stabilization of α -helices; these are kept small by choosing sufficiently large box dimensions.¹¹⁹

In the present work, for the simulation of explicit lipid environments, a rectangular box was chosen. Here the box size was chosen such that the surface-to-surface distance of the peptide and its nearest periodic images ('peptide-peptide distance') was at least 14 \AA in the direction of the bilayer normal and $45\text{--}50 \text{ \AA}$ in the bilayer plane. For pilot simulations of a peptide without lipid environment, a dodecahedron

box was used to minimize the system size. Here the box size was chosen such to obtain a peptide-peptide distance of at least 14 Å in all directions. As a measure for the range of electrostatic interactions, the Debye screening length^{120 †}

$$l = \frac{1}{F} \sqrt{\frac{\epsilon_0 \epsilon_r R T}{z c}}, \quad (2.8)$$

of the chosen concentrations c of monovalent ions $|z| = 1$ is determined to 14 Å. Therefore a certain shielding of the peptide from its nearest periodic images can be assumed, and artifacts from the periodicity of the system are expected to be small.

2.2.4 Temperature and pressure coupling

For systems which evolve accordingly to the Newtonian equations of motion (Eq. 2.5), the energy is conserved and depends on the initial conditions only; therefore, with increasing simulation time the ensemble of structures of a respective trajectory will approach a micro-canonical ensemble[‡]. A protein and its immediate lipid and solvent environment, however, continuously exchange energy with the surroundings, such that the temperature, rather than the energy, remains constant (canonical ensemble). In addition, force truncation and discretization errors introduce random forces which heat up the system. Therefore it is necessary to control the temperature T of the system, which should remain close to a given target temperature T_0 . To this aim, the system is coupled to a heat bath, for which various methods are available.

The *Nosé-Hoover thermostat*,^{122,123} e.g., induces a heat bath parameter as a new degree of freedom whose dynamics is driven by the deviation of the real system temperature from the heat bath temperature; here a respective 'inertia' parameter governs the strength of the coupling. This approach has the disadvantage that it produces a spurious oscillatory relaxation.

Therefore, in the present work, the *weak coupling scheme* of Berendsen¹²⁴ was used, which induces a strongly damped exponential relaxation of the temperature T towards a given target temperature T_0 , according to

$$\frac{dT}{dt} = \frac{T_0 - T}{\tau}, \quad (2.9)$$

[†]with the Faraday constant F and the gas constant R

[‡]assuming that a trajectory of infinite length will pass every phase space point equally frequent (ergodicity), or will pass arbitrarily close to every such point (quasi-ergodicity)¹²¹

with a time constant τ . This is done by scaling the velocities of each particle every step with a time-dependent factor λ given by

$$\lambda = \left[1 + \frac{\Delta t}{\tau_T} \left\{ \frac{T_0}{T} - 1 \right\} \right]^{1/2}, \quad (2.10)$$

The coupling time constant τ_T is related to the time constant τ of the temperature coupling according to

$$\tau = \frac{2C_V\tau_T}{N_f k_B}, \quad (2.11)$$

where C_V denotes the total heat capacity of the system, k_B Boltzmann's constant, and N_f the total number of degrees of freedom. The time constants τ_T and τ differ, because the scaling energy is partly redistributed between kinetic and potential energy. For the presented simulations, the protein, the different lipid species, the water, and the ions, were coupled separately to a heat bath of $T_0 = 300$ K, using a coupling time constant $\tau = 0.1$ ps. For the annealing simulations (see Sec. 2.2.7), temperatures T_0 of up to 1500 K were chosen.

Furthermore, biological systems are subjected to a constant pressure, which is usually 1 bar. Therefore in the present simulations isobaric ensembles were created; i.e., the pressure, rather than the volume, were kept constant. Similar to temperature coupling, an exponential relaxation of the pressure P to the target pressure $P_0 = 1$ bar was used (*Berendsen barostat*¹²⁴), according to

$$\frac{dP}{dt} = \frac{P_0 - P}{\tau_p}, \quad (2.12)$$

with a time constant of $\tau_p = 1$ ps. Thereto the coordinates were rescaled by a factor μ ,

$$\mu = 1 - \frac{\Delta t}{3\tau_p} \kappa \{P_0 - P\}. \quad (2.13)$$

every integration step. Here κ is the isothermal compressibility of the system. In the present work, the value for water at 1 atm and 300 K, $\kappa = 4.6e - 5 \text{ bar}^{-1}$, was used. The pressure P was calculated from the kinetic energy E_{kin} and the virial Ξ according to

$$P = \frac{2}{3V} (E_{\text{kin}} - \Xi), \quad (2.14)$$

where V denotes the volume of the system. The virial Ξ is defined as

$$\Xi = -\frac{1}{2} \sum_{i < j} (\mathbf{r}_i - \mathbf{r}_j) \cdot \mathbf{F}_{ij} \quad , \quad (2.15)$$

Here \mathbf{F}_{ij} denotes the force exerted from atom i on atom j .

For the simulations without explicit lipid environment, all directions were scaled equally. For the simulations *with* explicit lipid environment, the directions parallel and perpendicular to the bilayer plane (z axis and x/y directions, respectively) were scaled independently.

2.2.5 Improving efficiency

Molecular dynamics simulations are computationally highly expensive, therefore methods were applied to improve their efficiency. This was done by enlarging the time step, by using compound atoms, by applying an efficient method for the calculation of non-bonded forces, and by using parallel computers.

Enlarging the integration time step

Bond length constraints do not significantly alter the dynamics of proteins,¹²⁵ and, hence, were applied to enlarge the integration time step Δt (cf. Eqs. 2.6 and 2.7). Without bond stretching vibrations, the bending of the HOH bond angle remains as the fastest degree of freedom, with a period of 21 fs; hence an integration time step Δt (Eqs. 2.6 and 2.7) of 2 fs could be chosen. In the present work, for proteins and lipids the constraint algorithm LINCS¹²⁶ was used which, after an unconstrained integration step, rescales the bonds lengths to their average value. For water, the SETTLE algorithm was used which incorporates the constraints within the potential by means of Lagrange multipliers.¹²⁷

Angle constraints would remove vibrations with periods below 50 fs (Tab. 2.1) and, therefore, would allow to increase the time step to $\Delta t = 5$ fs. However, such constraints have been shown to affect conformational dynamics,¹²⁵ and, hence, were not used.

For most of the simulations, an increase of the time step to 4 fs was facilitated by enlarging the mass of hydrogen atoms from 1 (light hydrogen atoms) to 4 amu (heavy hydrogen atoms); the extra mass was subtracted from the associated heavy atoms.¹²⁸ Thus, the kinetics of the system are slightly slowed down, which, e.g., leads to an increase of water viscosity.¹²⁸ This artifact does not affect the present work, since here conformational distributions rather than kinetic properties are studied.

Further, the net gain in efficiency is only 15 % lower than expected from the time step increase by a factor of two.¹²⁸

Compound atoms

It has been shown that the dynamics and sterics of the nonpolar hydrogen atoms generally has no large influence on the structure and the dynamics of a protein.⁸⁷ Therefore in GROMOS-87, as in most force fields, atom groups such as CH, CH₂, or CH₃, are merged into *compound* atoms with respective total mass as well as adapted partial charges and van der Waals radii. In the presented simulations, particularly, 73 nonpolar hydrogen atoms per lipid molecule were incorporated into compound atoms.

Efficient calculation of non-bonded forces

To calculate the van der Waals (Fig. 2.1 *E*) and the Coulomb potential (*F*) all inter-atomic pair interactions have to be considered; this involves a computational expense which scales as $\mathcal{O}(N^2)$ with the the number N of atoms. In most of the presented simulations, the cost was reduced to $\mathcal{O}(N)$ by using a *cutoff* function.⁸⁷ Here only the force contributions from atoms within a predefined interaction radius r_1 (typically 10 Å) were considered; the list of pairs for which non-bonded interactions must be calculated (neighbor list) was updated every ten steps. This is a good approximation for the short-ranged van der Waals potential. For the long-ranged Coulomb forces, a *twin-range* approach^{84,129,130} was used. Here the forces between atoms within a shell $r_1 < r \leq r_2$ (with $r_2 = 18$ Å), which fluctuate more slowly than closer atoms, were only calculated during every neighbor list update. To avoid the creation of charges at the cutoff boundaries, groups of adjacent atoms with total charge 0 (e.g. water molecules, *charge groups*), were kept together.

For simulations of an ion-rich system, a more accurate — albeit computationally more expensive — calculation of the electrostatic forces was necessary. Since for the present work periodic boundary conditions were used, a lattice sum method could be employed. The *Ewald summation* was first introduced to calculate the long-range interactions of the periodic images in crystals.¹³¹ Here the slowly converging sum of all Coulomb interactions (Fig 2.1 *F*), which runs over all atom pairs (ij) and all periodic boxes, is replaced by two fast converging sums, one each in direct and in

reciprocal space, and a constant term. Thus short cutoffs can be used each for the direct and reciprocal sum (of the order of 10 Å and 10 wave vectors, respectively). The computational cost of the reciprocal sum scales as $\mathcal{O}(N^2)$ for the ordinary Ewald method, but only as $\mathcal{O}(N \log N)$ for the *particle-mesh Ewald* (PME)^{132,133} method. Here the charges are assigned to a grid ('charge grid') which then is subjected to a fast Fourier transformation. In the presented simulations, the PME method was used with a neighbor-list, Coulomb, and van der Waals cutoff $r_1 = r_2 = 9$ Å, and the charges were assigned to a grid with a lattice constant of 1.2 Å using cubic interpolation.

Parallelization

The run times of MD simulations can be considerably shortened by running each simulation on several processors in parallel. Here the atoms of the simulation system are distributed on the processors; this is done such that the required data transfer is minimized and the workload of the individual processors is maximized. The simulations of the present work were mainly run on clusters of 500 and 1000 MHz double processor PCs; for each simulation, two processors were used in parallel.

2.2.6 Minimization and equilibration

Minimization and equilibration have been carried out prior to the production simulation and serve to relax the system to an equilibrium for a given — usually physiological or room — temperature, in which the energy is equally distributed to all degrees of freedom. This relaxation is necessary, especially for the present work, for several reasons.

Most molecular dynamics simulations start from x-ray structures of macromolecules, which are determined at a limited resolution of 1.5–7 Å⁷⁵ (2.4 Å for the x-ray structure used in the present work⁷⁰). These are determined by fits to obtained electron density maps⁷⁵ and refined by simulated annealing and minimization procedures, in which the knowledge about covalent geometries is added.^{134,135} Nevertheless, due to trade-off between force field and goodness-of-fit to electron density maps the resulting structures can show abnorm bond lengths, considerable deformations of bond or torsion angles, and even overlaps of van der Waals spheres. In the present work, such

overlaps could also result from several modeling procedures which were necessary (see Secs. 3.1).

Such strains can lead to extremely high forces, which, for free MD, would destabilize the system. These strains were relaxed by a steepest descent on the energy landscape, until a local minimum was reached. In this iterative procedure, the step size, for which an initial value of 0.1 \AA was chosen, was adapted to the steepness of the potential; the descent was continued until the step size (in nm) converged to the machine precision.

Subsequent to the minimization, the system is coupled to a heat bath (Sec. 2.2.4), heated to the target temperature 300 K and subsequently equilibrated at this temperature. The equilibration is monitored by plotting relevant observables (see Sec. 2.3.1) versus time (see Secs 3.2.4 and 3.2.6). In a first step (see Chap. 3), equilibration was considered complete, when drifts of these observables were absent or small.

The absence of drifts, however, may indicate that the peptide has reached a metastable rather than a stable state: If the initial configuration of a simulated peptide is far away from its native structure, as it was possibly the case for the 5-residue syntaxin linker studied here, energy barriers might trap the peptide in a local free energy minimum distant from the native state. In this case, the peptide cannot reach equilibrium. Simulated annealing, which was used to facilitate the escape from local minima, is described in the next section.

From the part of the trajectory succeeding the minimization and equilibration phase, thermodynamical properties were calculated as sketched in Sec. 2.3.2.

2.2.7 Accelerated traversing of energy barriers

The structure and dynamics of polypeptides and proteins is governed by a high-dimensional, hierarchically ordered free energy landscape, which arises from the complex structure of these biomolecules.¹³⁶ A large number of nearly isoenergetic local minima, corresponding to the conformational substates of the proteins, are separated by energy barriers of different height. Localized motions usually involve the traversing of small energy barriers which can be overcome on picosecond timescales; collective motions involve higher energy barriers and rather occur on nano- or longer timescales.¹³⁷

Due to the system size of 20,000 atoms and the small integration time step of 4 fs, only nanosecond timescales were accessible for the simulations. During these small timescales only a small region of the accessible conformational space is sampled. This is called the *sampling problem* and is a general challenge for MD simulations; therefore a couple of methods have been developed to facilitate the traversing of energy barriers,^{96,138–146} e.g., MD in four spatial dimensions,¹³⁹ “conformational flooding”,¹⁴³ “self-guided MD”,¹⁴⁴ and “puddle skimming”,¹⁴⁶ see review.⁸¹

In some of these methods the acceleration is obtained by producing an unphysical distribution during a ‘sampling phase’, which then is relaxed towards a physiological distribution by slowly scaling an appropriate parameter during a ‘relaxation phase’.^{81,96,139} In the present work, the method of *simulated annealing*⁹⁶ was used, in which the sampling and the relaxation phase are effectuated by appropriately heating and cooling the system. Groups of annealing runs (‘annealing sets’) were performed for different solvated peptide-membrane systems. Each annealing set consists of a 1 ns sampling phase, during which the system is coupled to a heat bath of 1500 K (cf. Sec. 2.2.4, and see Fig. 2.2, *brown curve*). From the resulting trajectory, 27 structures (*green circles*) were chosen. Each of them was cooled down by decreasing the target temperature (Sec. 2.2.4) to 300 K linearly in time within a relaxation phase of 400 ps (*sloped blue lines*), and then equilibrated for further 200 ps (*horizontal blue lines*) at this temperature. The 27 final structures thus obtained (*red crosses*) were used for further analysis. The annealing simulations of this work are described in Chap. 4.

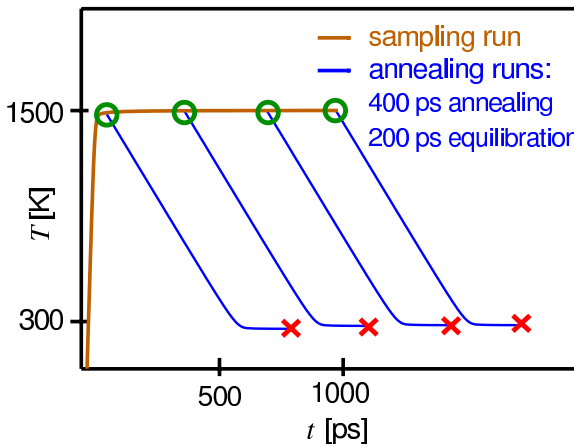


Figure 2.2: Procedure employed for each annealing set. From a 1 ns high temperature sampling run (*brown curve*), 27 snapshots (*green circles*) were selected, annealed for 400 ps, and subsequently equilibrated for 200 ps (*blue curves*). The final structures (*red crosses*) were kept for further analysis.

2.2.8 Restraints

In the presented simulations several restraints were used. Selected atoms were kept close to their initial positions \mathbf{r}_0 by subjecting them to a harmonic potential ('position restraint'),

$$V(\mathbf{r}) = \frac{k_{\mathbf{r}}}{2}(\mathbf{r} - \mathbf{r}_0)^2. \quad (2.16)$$

Here a force coefficient $k_{\mathbf{r}} = 358 \text{ kcal mol}^{-1} \text{ \AA}^{-2}$ was used, just small enough for the respective vibration period to exceed the chosen integration step width by at least a factor of eight.

Selected backbone dihedral angles were stabilized by defining supplementary dihedral contributions⁸⁴

$$V_d(\phi) = k_{\phi}[1 + \cos(\phi - \phi_0)] \quad (2.17)$$

for the peptide, with $\phi_0 = \alpha + 180^\circ$, α denoting the initial value of the dihedral, and a force constant of $k_{\phi} = 191 \text{ kcal mol}^{-1} \text{ deg}^{-2}$.

Selected helical peptide segments were stabilized by imposing the distance restraint potential implemented in GROMACS⁸⁴ on the $O_i - N_{i+3}$ atom pairs ('1-4 distance restraints'), which form hydrogen bonds within α -helices. Its shape can be seen in Fig. 2.3; it was chosen constant for distances smaller than the typical hydrogen bond distance 3 \AA — such that intact hydrogen bonds were not perturbed —, harmonic with a force constant $k_{\text{dr}} = 239 \text{ kcal mol}^{-1} \text{ \AA}^{-1}$ between 3 and 6 \AA , and linear for larger distances.

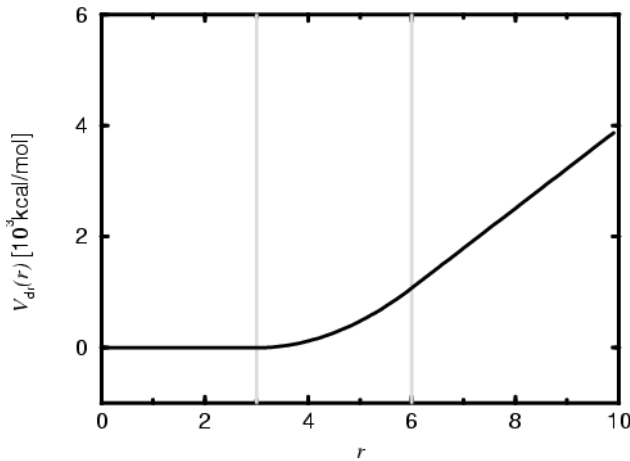


Figure 2.3: Distance restraint potential applied to backbone $O_i - N_{i+3}$ atom pairs ('1-4 distance restraints').

2.3 Analysis Methods

For the room temperature trajectories, the configuration of the system after every 400 fs, as well as the annealing final structures (Fig. 2.2 *red crosses*), were kept for further analysis. Based on data from individual structures as described in Sec. 2.3.1, thermodynamical properties were obtained as sketched in Sec. 2.3.2.

2.3.1 Analysis of individual snapshots

Observables

Fig. 2.4 shows the four focused observables. These are the H3 helix tilt θ and the TM helix tilt θ_{TM} with respect to the bilayer normal (z axis), the position z_{TM} of the center of mass of the TM helix C_α -atoms relative to the average z -position of the phosphor atoms of the bilayer, and the position z_{link} of the center of mass of the linker C_α -atoms relative to the average z -position of the phosphor atoms of the proximate monolayer.

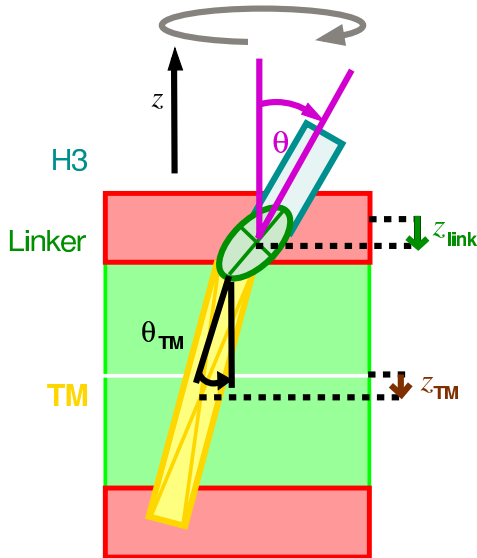


Figure 2.4: Reaction coordinates, H3 helix tilt angle θ , TM helix tilt θ_{TM} , TM helix position z_{TM} , and linker position z_{link} . The red rectangles indicate the polar regions, the green rectangle the hydrophobic core of the bilayer.

For a given peptide configuration, the helix orientations were determined by diagonalizing the covariance matrix

$$C = \langle (\mathbf{x} - \bar{\mathbf{x}})(\mathbf{x} - \bar{\mathbf{x}})^T \rangle \quad (2.18)$$

of respective C_α coordinates \mathbf{x} . The desired orientation was then given by the eigenvector associated to the largest eigenvalue.

Peptide helicity

The helicity of the linker and TM residues was analyzed using the criteria of Kabsch and Sander.¹⁴⁷ These base on the presence or absence of respective hydrogen bonds, as decided by an energetic cutoff criterion. This has the advantage that only a single decision parameter has to be chosen. In contrast, e.g., using backbone ϕ, ψ dihedrals (Fig. 1.3), four angles for a rectangle in the ϕ, ψ plane would have to be chosen.

The electrostatic energy E between a backbone carbonyl group C=O and a backbone amide group N-H was calculated by assigning partial charges to the C,O ($+q_1, -q_1$) and N,H ($-q_2, +q_2$) atoms,

$$E = q_1 q_2 \left(\frac{1}{r_{\text{ON}}} + \frac{1}{r_{\text{CH}}} - \frac{1}{r_{\text{OH}}} - \frac{1}{r_{\text{CN}}} \right) f, \quad (2.19)$$

with $q_1 = 0.42e$ and $q_2 = 0.20e$, e being the electron unit charge and r_{AB} the interatomic distance from A to B. The distances r are given in Å, the dimensional factor $f = 332$, and E is obtained in kcal/mol. While a strong hydrogen bond has a binding energy of about -3 kcal/mol, a generous cutoff is chosen which allows for bifurcated hydrogen bonds:¹⁴⁷ A hydrogen bond was assigned between the C=O group of residue i and N-H of residue j , if E was less than the cutoff,

$$\text{Hbond}(i,j) : \{ E < -0.5 \text{ kcal/mol} \}.$$

A hydrogen bond from CO(i) to NH($i+3$) formed a '4-turn', i.e.,

$$\text{4-turn}(i): \text{Hbond}(i,i+3).$$

Two consecutive 4-turns formed a minimal α -helix,

$$\alpha\text{-helix}(i, i+3): \{ \text{4-turn}(i-1) \text{ and } \text{4-turn}(i) \}.$$

In particular, this definition imposes no requirement on the the hydrogen bond state of residues $i+1$ and $i+2$.

Peptide-lipid hydrogen bonds

For ensembles of structures obtained from MD simulations at 300 K and sets of simulated annealing runs, the hydrogen bonds between the peptide and the surrounding lipid headgroups were determined using the program `g_hbond` of the GROMACS simulation package.⁸⁴ Hydrogen bonds were counted, as a geometric cutoff criterion, if the distance between the hydrogen atom and the acceptor was below 2.5 Å and the angle between hydrogen atom, donor and acceptor was below 60°.

2.3.2 Thermodynamics: Free energy calculations

As a measure for the bending stiffness of the linker, the free energy landscape $G(\theta)$ along the H3 helix tilt angle θ was determined from the equilibrium distribution $p(\theta)$ of θ in a free dynamics simulation according to

$$G(\theta) = -k_{\text{B}}T \ln p(\theta). \quad (2.20)$$

Here T denotes the temperature and k_{B} Boltzmann's constant. A broad or narrow distribution indicated a soft or stiff potential, respectively. Here, omitting a 3 ns equilibration phase, p was estimated from the final 2 ns of a 5 ns room temperature trajectory (5000 structures). This approach allowed to extract free energy landscapes $G(x)$ for several reaction coordinates x (Fig. 2.4) from a single simulation.

Eq. 2.20 was applied as follows: An appropriate range $[x_{\min}, x_{\max}]$ was divided into $\sqrt{n} + 1$ bins of equal width Δx , where n is the number of available structures of the given ensemble. From the relative frequencies p_i of structures for which x falls into the i -th bin, an estimate for the free energy landscape is obtained from a discretized version of Eq. 2.20,

$$G(x_i) = -k_{\text{B}}T \ln p_i, \quad (2.21)$$

where x_i denotes the center of bin i . To remove statistical noise, the energy landscape was smoothed by a Gaussian filter of width $\sigma = 5\Delta x$. Additionally, the associated stiffnesses were determined from harmonic fits,

$$G_{\text{H}}(x) = \frac{1}{2}k(x - \mu)^2, \quad (2.22)$$

to the free energy landscapes, obtained by computing average (equilibrium) values

$$\mu = \langle x \rangle \quad (2.23)$$

and variances

$$\sigma^2 = \langle (x - \mu)^2 \rangle \quad (2.24)$$

of the observable x . Effective stiffnesses k were obtained from these harmonic fits via

$$k = k_B T / \sigma^2. \quad (2.25)$$

For the tilt angle θ , Eqs. 2.21, 2.23, and 2.25 were also applied to sets of annealing final structures (Fig. 2.2, *red crosses*). Here no Gaussian smoothing for the free energy landscape $G(\theta_i)$ was performed.

To estimate how much the linker stiffness reduces the fusion energy barrier (and thereby increases the fusion efficiency), the energy $\Delta G = G(\theta_1) - G(\theta_0)$ required to bend the H3 helix from its average value θ_0 to the value $\theta_1 = 80^\circ$ needs to be calculated. Here θ_1 was chosen smaller than 90° assuming that an induced membrane bending reduces the energy that is actually transmitted to a small extent.

In the free dynamics simulations (see Chap. 3), however, not the whole range between θ_0 and θ_1 was sampled, and, accordingly, $G(\theta)$ could only be characterized close to the observed minimum. To extend the range of observed θ values towards regions which are rarely visited in the original Boltzmann ensemble, a bias potential (umbrella potential)¹⁴⁸ $V^*(\theta)$ could have been added to the original energy function to restrain θ close to a desired value $\hat{\theta}$; the sign-inverted ensemble-averaged value $-\langle \partial V^* / \partial \theta \rangle$ of the required restraint torque would then yield the respective mean torque of the original ensemble. The free energy landscape (potential of mean torque) could then be calculated by integrating the mean torque obtained from multiple simulations at discrete values of \hat{x} , or from appropriate time windows of a single simulation in which \hat{x} varies sufficiently slowly over the whole desired range.¹⁴⁹

This approach was not applied, as the θ values observed in the sets of annealing final structures were distributed over the whole range $[0^\circ, \theta_1]$, such that the calculation of ΔG did not require the usage of an umbrella potential. A harmonic function (Eq. 2.22) proved to be a reasonable approximation to $G(\theta)$ in the relevant angle interval, such that the tilt energy could be estimated from

$$\Delta G = \frac{1}{2} k (\theta_1 - \mu)^2. \quad (2.26)$$

Free energy of helix formation

For selected residues i , the probability p_i and free energy ΔG_i of helix formation was estimated from sets of annealing final structures (Fig. 2.2, *red crosses*) as follows: Using the criteria described above the number n_i of structures was determined for which one of the neighbors of the residue i was α -helical, and the number f_i of structures in which the residue i was α -helical itself. The free energy ΔG_i of helix formation was estimated via

$$\Delta G_i = -k_B T \ln \frac{p_i}{1 - p_i}, \quad (2.27)$$

with

$$p_i = f_i / n_i. \quad (2.28)$$

Hydrogen bonds and atomic positions

For the 2 ns production phase of free dynamics runs, the average z position $z_0 = \langle z \rangle$ of C_α and side-chain nitrogen and oxygen atoms with respect to the phosphor atoms of the linker-proximate lipid monolayer, and the average number $N_{\text{HB}} = \langle n_{\text{HB}} \rangle$ of hydrogen bonds between the peptide and lipid headgroups as well as respective fluctuations

$$\sigma_z = \langle (z - z_0)^2 \rangle^{1/2} \quad (2.29)$$

and

$$\sigma_{N,\text{HB}} = \langle (n_{\text{HB}} - N_{\text{HB}})^2 \rangle^{1/2} \quad (2.30)$$

were determined.

2.4 Statistical accuracy and significance

In contrast to the 5000 structures obtained from the room temperature ensembles, the annealing sets (Sec. 2.2.7) provided only 27 final structures, thus limiting the accuracy and resolution of the obtained free energy landscapes for the tilt angle θ according to Eq. 2.21, as well as the accuracy of the parameters of the harmonic fit (Eqs. 2.23 and 2.25), the tilt energies (Eq. 2.26), and free energies of helix formation (Eq. 2.27). That is, estimates $\gamma(\mathbf{x})$ (e.g., average tilt angles θ_0) were obtained from small samples $\mathbf{x} = (x_1, \dots, x_n)$ [e.g., arrays $(\theta_1, \dots, \theta_n)$ of tilt angles] and, thus,

are broadly distributed around the respective true value γ_0 . As a measure for the statistical accuracy of the estimate $\gamma(\mathbf{x})$, a range $[\gamma_-(\mathbf{x}), \gamma_+(\mathbf{x})]$ was determined which contains γ_0 with a high probability $1 - \alpha$ (see Fig. 2.5, *left*),

$$P(\gamma_-(\mathbf{x}) \leq \gamma_0 \leq \gamma_+(\mathbf{x})) = 1 - \alpha; \quad (2.31)$$

that is, if many samples \mathbf{x}' were drawn, the respective ranges $[\gamma_-(\mathbf{x}'), \gamma_+(\mathbf{x}')] would contain γ_0 in $(1 - \alpha) \cdot 100\%$ of all cases. Such a range is referred to as $(1 - \alpha)$ *confidence interval*. For the present work, $\alpha = 0.05$ was chosen.$

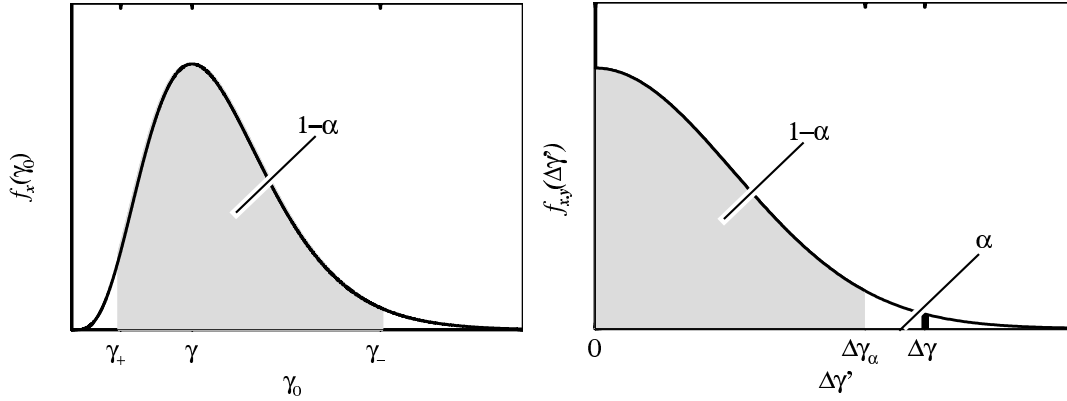


Figure 2.5: Confidence (*left*) and significance (*right*) estimation. For explanations see text.

Similarly, differences of estimates $\gamma(\mathbf{x})$ and $\gamma(\mathbf{y})$ obtained from different samples $\mathbf{x} = (x_1, \dots, x_n)$ and $\mathbf{y} = (y_1, \dots, y_n)$, i.e., different sets of annealing final structures, may either arise from statistical fluctuations or reflect a difference $\gamma_1 \neq \gamma_2$ of the real values, thus being *significant*. To discriminate between these two cases, *hypothesis tests* were performed. Here, under the *null hypothesis*

$$H_0 : \gamma_1 = \gamma_2, \quad (2.32)$$

from the single sample pair \mathbf{x} and \mathbf{y} , the expected distribution $f_{\mathbf{x},\mathbf{y}}(\Delta\gamma)$ (see Fig. 2.5 *right*) of the *test quantity*

$$\Delta\gamma(\mathbf{x}', \mathbf{y}') = |\gamma(\mathbf{x}') - \gamma(\mathbf{y}')| \quad (2.33)$$

(or a similar quantity sensitive to $\Delta\gamma$) for a long series of sample pairs $\mathbf{x}' = (x_1, \dots, x_n)$ and $\mathbf{y}' = (y_1, \dots, y_n)$, drawn from the same distributions as \mathbf{x} and \mathbf{y} , respectively, is estimated. If differences $\Delta\gamma(\mathbf{x}', \mathbf{y}')$ equal or larger than the one

actually observed, $\Delta\gamma(\mathbf{x}, \mathbf{y})$, rarely occur, i.e., with a probability lower than a predetermined small *error probability* (significance level) α (as it is the case in the figure), the hypothesis is rejected. The significance level α , for which H_0 is just rejected, is called the α -value of the performed test. It is a measure for the significance of observed parameter differences; small α -values indicate high, large α -values low significance.

Confidence intervals and statistical significances were calculated for estimates or pairs of estimates, respectively, obtained from sets of annealing final structures. Unlike subsequent structures from normal MD trajectories which are highly correlated, annealing final structures should, by construction, be hardly correlated. Therefore confidence and significance estimation could be performed using methods which base on the assumption that subsequent data points x_i and x_{i+1} of each sample \mathbf{x} are independent and obey the same underlying distribution.

Confidence intervals for the average tilt angle, the tilt stiffness, the free energies of tilt intervals, and the free energies of helix formation, were determined from accurate analytical methods (see Sec. 2.4.1). For tilt energies no analytical method was available, therefore a numerical method was applied.

For the hypothesis test on the equality of average tilt angles, the only available accurate analytical method, Student's t -test, required to assume equal tilt stiffnesses,¹⁵⁰ i.e., equal variances, and therefore was not appropriate for the present work. A modified Student's t -test for arbitrary variances is only valid for large sample sizes and, therefore, too, presumably inadequate for this work. Thus, a numerical hypothesis test was used instead. Numerical hypothesis tests were also used to test on the equality of tilt stiffnesses, free energies of tilt intervals, and the free energy of helix formation (see Sec. 2.4.2).

2.4.1 Analytical confidence estimates

For the analytical estimation of confidence intervals the *pivot method*¹⁵⁰ was used. Here, as the true parameter γ_0 was unknown, a *pivotal quantity* $\pi(\mathbf{x}', \gamma_0)$ was considered, whose distribution did not depend on γ_0 . From the distribution of π , a respective confidence interval $[\pi_-(\mathbf{x}'), \pi_+(\mathbf{x}')] was determined. Setting \mathbf{x}' equal to the observed sample \mathbf{x} , this interval for π was converted into a confidence interval for γ_0 .$

The confidence interval of π was not uniquely fixed by Eq. 2.31 and chosen such that the excluded tails of the distribution of π had equal weight,¹⁵⁰

$$P(\pi_0 \leq \pi_-(\mathbf{x})) = P(\pi_+(\mathbf{x}) \leq \pi_0) = \alpha/2. \quad (2.34)$$

Because the distributions of the chosen pivotal quantities are nearly symmetric (see Fig. 2.6), this interval has, to a good approximation, minimal length, and therefore yields a preferably accurate estimate.¹⁵⁰

The pivotal quantities used for analytical confidence estimates were

$$t = \sqrt{n} \frac{\mu - \mu_0}{\sigma}, \quad (2.35)$$

for the average tilt angle,

$$\chi^2 = \frac{(n-1)\sigma^2}{\sigma_0^2}, \quad (2.36)$$

for the tilt stiffness, and

$$\eta = \sqrt{\frac{n}{p_0(1-p_0)}}(p - p_0), \quad (2.37)$$

for the free energy of tilt intervals and helix formation. Here μ_0 denotes the true average, μ the empirical average according to Eq. 2.23 (with $x = \theta$), σ the empirical variance from Eq. 2.24, σ_0 the true variance, n the sample size, p the probability estimate (Eq. 2.14) used to calculate free energies (Eqs. 2.21 and 2.27), and p_0 the true probability value.

Assuming that the tilt angles obey a normal distribution, t (Eq. 2.35) obeys a Student's t -distribution with $n-1$ degrees of freedom,¹⁵⁰ with the probability density function⁹⁸

$$f_{n-1}^T(t) = \frac{\Gamma(\frac{n}{2})}{\sqrt{(n-1)\pi}\Gamma(\frac{n-1}{2})} \left(1 + \frac{t^2}{n-1}\right)^{-\frac{n}{2}}, \quad -\infty < t < \infty \quad (2.38)$$

(for the sample size $n = 27$ see Fig. 2.6, *left*) and χ^2 (Eq. 2.36) obeys a χ^2 -distribution with $n-1$ degrees of freedom,¹⁵⁰ with the probability density function⁹⁸

$$f_{n-1}^{\chi^2}(t) = \begin{cases} \frac{1}{\Gamma((n-1)/2)2^{(n-1)/2}} e^{-t/2} t^{(n-1)/2-1}, & 0 < t < \infty, \\ 0, & t \leq 0, \end{cases} \quad (2.39)$$

(see Fig. 2.6, *right*), where Γ denotes the gamma function,⁹⁸

$$\Gamma(x) = \int_0^\infty e^{-t} t^{x-1} dt. \quad (2.40)$$

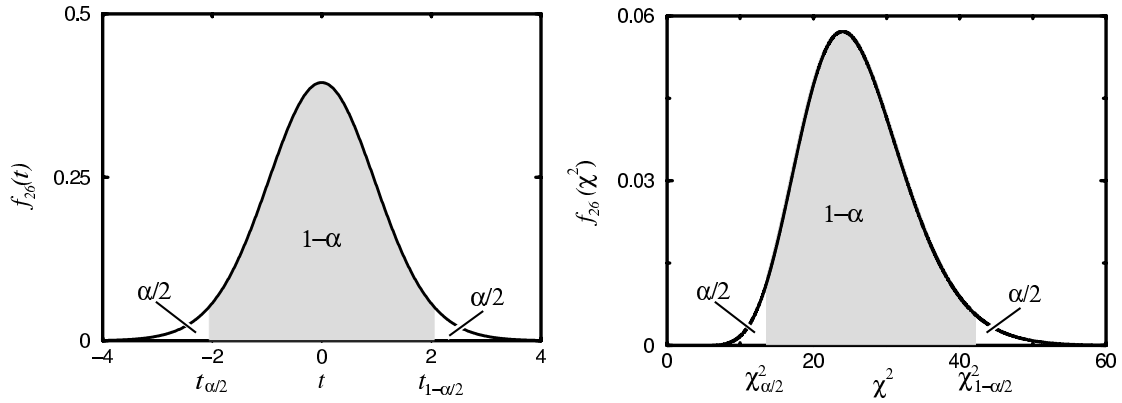


Figure 2.6: Probability density functions of Student's t -distribution (*left*) and χ^2 -distribution (*right*), each with 26 degrees of freedom. Also shown are the respective 0.025 ($\alpha/2$) and 0.975 ($1-\alpha/2$)-quantiles.

The probability estimates from Eq. 2.14 obey a binomial distribution. Assuming sufficiently large sample sizes, this distribution is approximated by a normal distribution with the center p_0 and the standard deviation $[n/p_0(1-p_0)]^{-1/2}$; within this *asymptotic* approximation, η (Eq. 2.37) obeys a normalized, centered normal distribution with the probability density function

$$\phi(t) = \frac{1}{\sqrt{2\pi}} e^{-\frac{1}{2}t^2}. \quad (2.41)$$

Equating the weights of the excluded tails for t ,¹⁵⁰ χ^2 ,¹⁵⁰ and η (Wilson score method¹⁵¹), respectively, yields the associated confidence intervals

$$[t_-, t_+], \quad t_{\pm} = \pm t_{n-1;1-\alpha/2}, \quad (2.42)$$

$$[\chi_-^2, \chi_+^2] = [\chi_{n-1,\alpha/2}^2, \chi_{n-1,1-\alpha/2}^2], \quad (2.43)$$

$$[\eta_-, \eta_+], \quad \eta_{\pm} = \pm \phi_{1-\alpha/2}. \quad (2.44)$$

Here $t_{n-1;1-\alpha/2}$ is the $(1-\alpha/2)$ quantile of the t -distribution, defined via¹⁵⁰

$$\int_{-\infty}^{t_{n-1,1-\alpha/2}} f_{n-1}^T(x) dx = 1 - \alpha/2, \quad (2.45)$$

and $\chi_{n-1,\alpha/2}^2$, $\chi_{n-1,1-\alpha/2}^2$, and $\phi_{1-\alpha}$ denote the respective quantiles of the χ^2 - and the centered normal distribution (cf. Figure). Using Eqs. 2.35 and 2.36, respectively, Eqs. 2.42 and 2.43 convert into the confidence limits

$$\mu_{\pm} = \mu \pm \frac{\sigma}{\sqrt{n}} t_{n-1,1-\alpha/2} \quad (2.46)$$

for μ_0 and

$$[\sigma_-^2, \sigma_+^2] = \left[\frac{(n-1)\sigma^2}{\chi_{n-1, 1-\alpha/2}^2}, \frac{(n-1)\sigma^2}{\chi_{n-1, \alpha/2}^2} \right] \quad (2.47)$$

for σ_0^2 .¹⁵⁰ The confidence limits p_{\pm} for p_0 are the solutions of the quadratic equation for p_0 obtained by squaring and equating Eqs. 2.37 and 2.44,¹⁵¹

$$p_{\pm} = \frac{2f + a^2 \pm a\sqrt{a^2 + 4f(1 - f/n)}}{2(n + a^2)}, \quad (2.48)$$

where $a = \phi_{1-\alpha/2}$. Note that the values p_{\pm} from Eq. 2.48, although derived within the asymptotic approximation, provide accurate confidence limits according to Eq. 2.31 for sample sizes n down to 5,¹⁵² and thus could be used for the present work.

The respective confidence interval for the stiffness k is obtained from Eq. 2.25 by replacing σ by its bounds σ_{\pm} ; the confidence limits for $G(\theta_i)$ and ΔG_i were calculated from Eqs. 2.21 and 2.27, respectively, by replacing p_i by its bounds p_{\pm} obtained from Eq. 2.48.

2.4.2 Numerical confidence and significance estimates

For numerical confidence and significance estimation the bootstrap method¹⁵³ was used. As sketched in Fig. 2.7 (*top*), its basic idea is to estimate the probability density distribution $f(x)$ underlying the individual data points x_i of a given sample $\mathbf{x} = (x_1, \dots, x_n)$ as a sum of equal-weighted delta functions at these data points (*gray bars*),

$$f(x) = \frac{1}{n} \sum_{i=1}^n \delta(x - x_i). \quad (2.49)$$

For confidence estimation, B synthetic samples \mathbf{x}_b^* (bootstrap replica) are generated from $f(x)$, each equal in size to the original sample \mathbf{x} , by sampling with replacement from \mathbf{x} . From the distribution $g(\gamma^*)$ (Fig. 2.7 *bottom*) of respective estimates $\gamma_b^* = \gamma(\mathbf{x}_b^*)$,

$$g(\gamma^*) = \frac{1}{B} \sum_{b=1}^B \delta(\gamma - \gamma_b^*), \quad (2.50)$$

a confidence interval $[\gamma_-, \gamma_+]$ is obtained via excluding tails of total weight α .

Similarly, for hypothesis tests, B pairs of samples \mathbf{x}^* and \mathbf{y}^* , each equal in size to the original samples \mathbf{x} and \mathbf{y} , respectively, are generated via sampling with replacement from appropriately modified data sets $\tilde{\mathbf{x}}$ and $\tilde{\mathbf{y}}$ (see below) to determine an empirical distribution of the test quantity $\Delta\gamma(\tilde{\mathbf{x}}^*, \tilde{\mathbf{y}}^*)$.

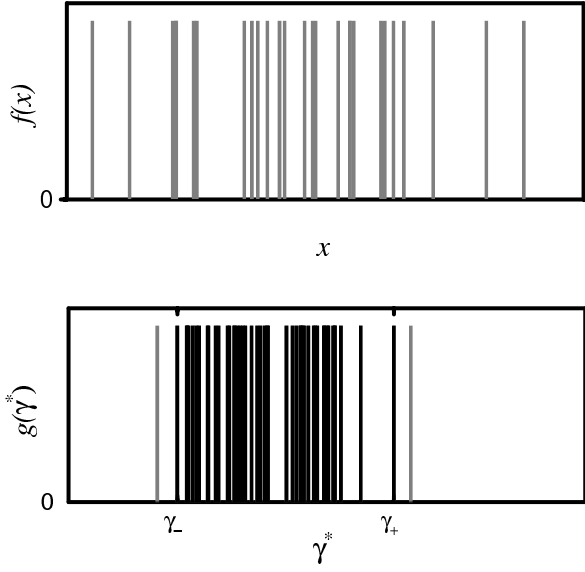


Figure 2.7: Numerical confidence estimation via bootstrap method. *Top:* Empirical distribution $f(x)$ of measured observable x . *Bottom:* Distribution $g(\gamma^*)$ of replications $\gamma_b^* = \gamma(\mathbf{x}_b^*)$ obtained from $B = 50$ bootstrap replica \mathbf{x}_b^* . The bars indicate delta functions according to Eq. 2.49 (*top*) or Eq. 2.50 (*bottom*), respectively. The values γ_- and γ_+ yield the limits of a 95% confidence interval.

Confidence intervals $[\Delta G_-, \Delta G_+]$ for tilt energies ΔG (Eq. 2.26) were estimated from an empirical distribution of estimates $\Delta G(\mathbf{x}^*)$, obtained from $B = 5000$ bootstrap replica \mathbf{x} via excluding tails with weights $\alpha/2$ each. To verify that convergence was reached, varying numbers of replica were considered.

Hypothesis tests for parameters of harmonic fit

To test on the equality of average tilt angles and tilt stiffnesses, respectively, a bootstrap test on the equality of means¹⁵³ was used. To obtain a theoretical foundation of this test, a general frame for such bootstrap hypothesis tests was created, in which the used bootstrap mean test could be embedded as a special case.

Consider the following case. Given two samples $\mathbf{x} = (x_1, \dots, x_n)$ and $\mathbf{y} = (y_1, \dots, y_m)$ of a continuous variable, the null hypothesis H_0 that the underlying distributions of \mathbf{x} and \mathbf{y} match in a parameter γ (cf. Eq. 2.32) shall be tested. To determine the distribution of a test quantity t (Eq. 2.33) under this null hypothesis, bootstrap replica of \mathbf{x} and \mathbf{y} are created from two respective distributions of the form 2.49. To fulfill the null hypothesis, however, the δ functions are not located at the original values x_i and y_i of the data points, but at shifted values \tilde{x}_i and \tilde{y}_i , such that the resulting distributions will match in the value of γ . The γ values of the distribution are expected to match if the transformed 'samples' $\tilde{\mathbf{x}} = (\tilde{x}_1, \dots, \tilde{x}_n)$ and $\tilde{\mathbf{y}} = (\tilde{y}_1, \dots, \tilde{y}_m)$ are chosen such that the respective γ estimates are equal,

$$\gamma(\tilde{\mathbf{x}}) = \gamma(\tilde{\mathbf{y}}). \quad (2.51)$$

Simultaneously, $\tilde{\mathbf{x}}$ and $\tilde{\mathbf{y}}$ must only minimally deviate from the original samples \mathbf{x} and \mathbf{y} . Therefore, using the Lagrange multiplier method, the sets $\tilde{\mathbf{x}}$ and $\tilde{\mathbf{y}}$ are chosen such as to minimize the function

$$L(\tilde{\mathbf{x}}, \tilde{\mathbf{y}}, \lambda, \mu, \nu) = \sum_{i=1}^n (\tilde{x}_i - x_i)^2 + \sum_{i=1}^m (\tilde{y}_i - y_i)^2 + \lambda[\gamma(\tilde{\mathbf{x}}) - \mu] + \nu[\gamma(\tilde{\mathbf{y}}) - \mu]. \quad (2.52)$$

Sampling by replacement from $\tilde{\mathbf{x}}$ and $\tilde{\mathbf{y}}$, the empirical distribution of the test quantity,

$$t(\tilde{\mathbf{x}}^*, \tilde{\mathbf{y}}^*) = |\gamma(\tilde{\mathbf{x}}^*) - \gamma(\tilde{\mathbf{y}}^*)|, \quad (2.53)$$

is determined. The fraction of samples for which t exceeds the observed value yields the desired significance.

For $\gamma = \langle x \rangle$, the transformed samples read

$$\tilde{x}_i = x_i - \langle x \rangle + \mu, \quad \tilde{y}_i \text{ similar}, \quad (2.54)$$

with

$$\mu = \frac{n\langle x \rangle + m\langle y \rangle}{n + m}. \quad (2.55)$$

This reproduces the bootstrap hypothesis test on the equality of means found in the literature,¹⁵³ if the test quantity is modified to

$$t(\tilde{x}, \tilde{y}) = \frac{|\langle \tilde{x} \rangle - \langle \tilde{y} \rangle|}{\{[\langle (\tilde{x} - \langle \tilde{x} \rangle)^2 \rangle + \langle (\tilde{y} - \langle \tilde{y} \rangle)^2 \rangle]/n\}^{1/2}}. \quad (2.56)$$

This test was applied to sample pairs $\{\theta\}, \{\tilde{\theta}\}$ to test on the equality of average tilt angles ('bootstrap mean test'); for stiffnesses, it was applied to the absolute deviations from the mean, $\{|\theta - \langle \theta \rangle|\}, \{|\tilde{\theta} - \langle \tilde{\theta} \rangle|\}$ ('bootstrap variance test'). In both cases, 30,000 bootstrap replica were generated. To check for convergence, varying numbers of replica were considered.

Probability test

For differences in the helicity of the individual linker residues (Eq. 2.27), a modified bootstrap test for the equality of probabilities ('bootstrap probability test') was devised: For two structure samples of sizes n_1 and n_2 , let the studied residue be in helical conformation in k_1 and k_2 cases, respectively, yielding probability estimates $p_i = k_i/n_i, i = 1, 2$. With the null hypothesis that the underlying probabilities are equal, the expression

$$p = \frac{k_1 + k_2}{n_1 + n_2} \quad (2.57)$$

provides the best probability estimate. That estimate was subsequently used to generate bootstrap samples, thus yielding empirical distributions for k_1 and k_2 and, therefore, also for the test quantity $t = |p_1 - p_2|$. Hence the significance was estimated similarly as above.

Statistical independence of successive tilt angles

To check to what extent the tilt angles θ_i and θ_{i+1} of successive annealing start structures (Fig. 2.2, *green circles*) can be considered statistically independent, the (auto-)correlation coefficient r ,

$$r = \frac{\sum_i (\theta_i - \langle \theta \rangle_0)(\theta_{i+1} - \langle \theta \rangle_1)}{[(\sum_i (\theta_i - \langle \theta \rangle_0)^2)(\sum_i (\theta_{i+1} - \langle \theta \rangle_1)^2)]^{1/2}}, \quad (2.58)$$

with $\langle \theta \rangle_0 = \sum_i \theta_i / (n - 1)$ and $\langle \theta \rangle_1 = \sum_i \theta_{i+1} / (n - 1)$, was calculated. The significance of the calculated correlation coefficients was assessed by a 'bootstrap correlation test' for the null hypothesis of uncorrelated data. Bootstrap samples were generated by randomly permuting the θ_i , and the significance was estimated similarly as above from the obtained distribution of the test quantity $t = |r|$. A similar procedure was applied to the tilt angles of successive annealing final structures (Fig. 2.2, *red crosses*).

Chapter 3

Room Temperature Simulation Results

In this chapter room temperature simulations are presented which were performed to predict the structure and stiffness of the syntaxin linker. Based on the assumption that the linker in its native environment folds downhill on the free energy landscape, the linker was modeled in an arbitrary initial conformation and expected to drift towards its native structure during a subsequent molecular dynamics simulation.

Sec. 3.1 describes a pilot study in which the relevance of the membrane to the linker properties was checked by simulations without membrane environment and with a simplified membrane model, respectively. Sec. 3.2 presents the main simulations which were carried out with an explicit lipid and solvent environment. Here, two different lipid compositions were chosen, yielding a neutral and an acidic bilayer. Furthermore, besides the wild type peptide, also a prolonged mutant was simulated. From these simulations, free energy landscapes for relevant observables, such as helix tilts and peptide position within the membrane, were obtained.

3.1 Pilot studies: absent and simplified lipid environment

The linker structure is presumably influenced by the adjacent peptide regions, the cytosolic H3, and the TM domain. As each of these is α -helical, the associated backbone dipoles (the CO and NH groups) are aligned and create a considerable total

dipole moment pointing towards the N-terminus; this helix dipole could stabilize an α -helical linker conformation. Also adjacent side chains could strongly influence the linker conformation via electrostatic as well as steric interactions. Therefore, besides the linker itself, linker-adjacent H3 and TM segments were included within the simulation system. In addition to that the solvent environment was considered to strongly influence the linker conformation (Sec. 2.2.2); thus an explicit solvent environment was chosen.

Just from first principles it could not be decided, if the lipid environment affects the linker structure, too, and, therefore, should be included within the production simulations. To decide this question, two simulations of 2 ns length each were carried out (Tab. 3.1); the first without lipid bilayer, the second using a simplified bilayer model described below. Here a peptide with a truncated TM domain (WT^S) was used. It comprised 22 residues (253–274), including eight H3 residues (253–260), the five linker residues (261–265), and 9 TM residues (266–274) resulting in 234 peptide atoms, and a net peptide charge of +7 e. The peptide sequence is given in Tab. 5.1. The conformations of two linker residues (Ala-261 and Arg-262) obtained from these simulations were used to model a linker start structure that was improved in subsequent simulations with explicit lipid environment.

Table 3.1: Simulation systems used in pilot study

Simulation system	Peptide	Bilayer Model	N_w	Ions	N_a	a	\times	b [Å]	\times	c
WT ^S /–	WT ^S	–	3036	7 Cl [–]	9353	51.3	\times	51.3	\times	51.3
WT ^S /VdW	WT ^S	VdW	4874	7 Cl [–]	14863	59.9	\times	59.9	\times	59.9

The peptide WT^S (residues 253–274) was simulated without (‘–’) and with a simplified (‘VdW’) bilayer model. Given are the respective number of water molecules (N_w), the number of atoms (N_a), and the initial size ($a \times b \times c$) of the dodecahedron box with angles 60°, 60°, and 90°.

Fig. 3.1 helps the reader to keep track of the various simulations and their interdependencies both for the pilot runs as well as for the subsequent equilibrium (Sec. 3.2) and annealing runs (Chap. 4). To obtain a start structure (see Fig. 3.2 *top left*), protein data bank (PDB)¹⁵⁴ data (where available) and modeling were combined (see Fig. 3.1, *green boxes*). The H3 helix was taken from chain F of the x-ray structure,⁷⁰ PDB entry 1sfc (*green arrows* from ‘PDB’-box). Because the x-ray structure

only contains heavy atoms, polar hydrogen atoms were added using the program `pdb2gmx` of the GROMACS package.⁸⁴

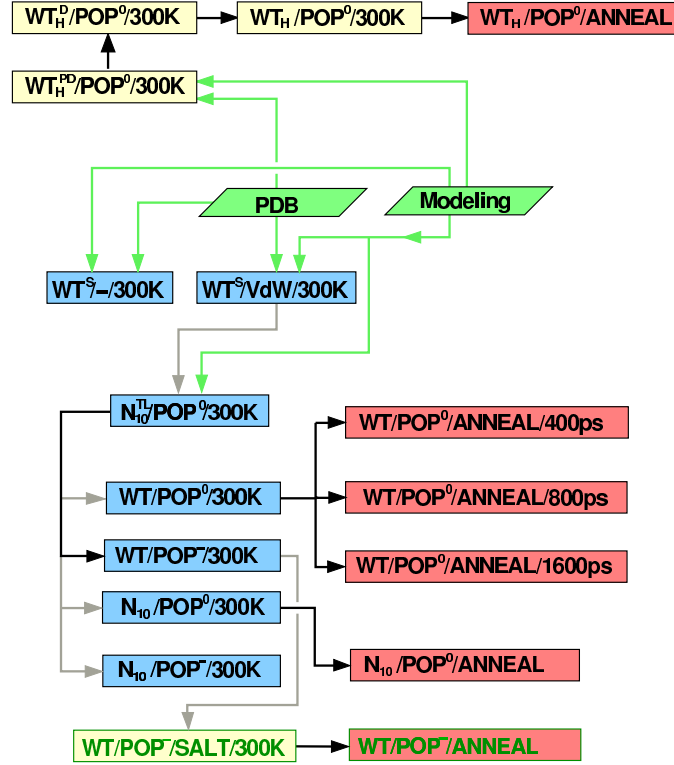


Figure 3.1: Overview of simulation runs and their mutual interdependencies. Blue (or yellow) and red boxes denote room temperature runs at $T = 300$ K (also tagged '300K'), and annealing sets ('ANNEAL'), respectively; green fonts indicate simulations with intracellular salt conditions. Green arrows denote input from the protein data bank or major modeling steps; black and gray arrows indicate that a final configuration has been used as a starting configuration for a subsequent simulation, either without (*black*) or with (*gray*) modification. For nomenclature and specification of the various simulation systems, see Tabs. 3.1, 3.4, and 3.5.

The TM domain was modeled as a right-handed α -helix, choosing the values $\phi = -60^\circ$ (see Fig. 1.3) for the angle between the plane containing the atoms C, N, C_α and that containing N, C_α , C, and $\psi = -50^\circ$ for the angle between the N- C_α -C and the C_α -C-N plane. The linker was modeled in a more extended (' β -like') conformation. For the side-chain dihedral angles, the default settings of the used molecular editor, INSIGHTII,¹⁵⁵ were used.

For the $WT^S/-/300K$ -simulation without lipid environment (Fig. 3.1 *blue box, left column*), periodic boundary conditions were chosen. The box dimensions were chosen such that minimum distance of 7 Å between the centered peptide and the bound-

ary was obtained; to minimize the number of solvent molecules which had to be simulated, a dodecahedron box was used. After solvation, 7 Cl^- ions were inserted for charge compensation, placed at energetically favorable positions ('Coulomb criterion'). In order to mimic the helix-stabilizing effect of the membrane (cf. Sec. 1.2.1), the secondary structure of the TM helix was stabilized by 1-4 distance restraints (Sec. 2.2.8). Similarly, to include the stabilizing effect of the coiled-coil helices which were present in the crystal structure but not included within the simulation system (Secs. 3.1 and 3.2.2), 1-4 distance restraints were also imposed on the H3 helix.

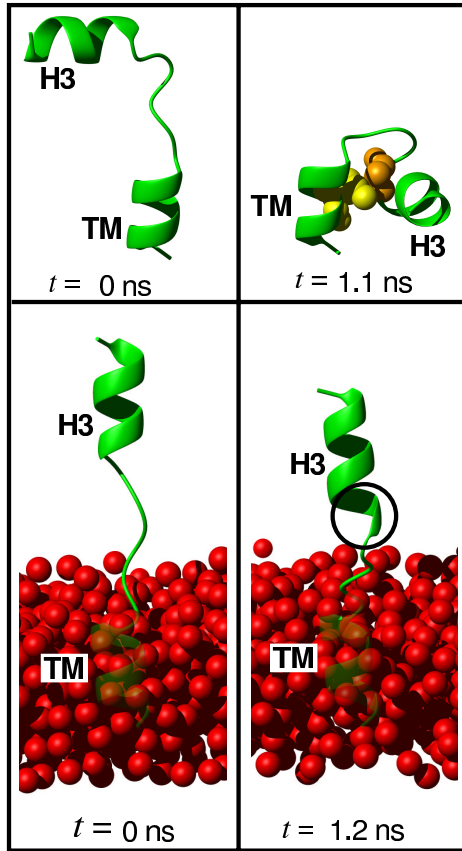


Figure 3.2: Starting peptide structures (*left*) and intermediate structures (*right*) of the two pilot simulations described in the text, without lipid environment (*top*) and with simplified lipid environment (*bottom*). In the top right figure, the spheres show the residue pair forming a hydrophobic contact which stabilized the final structure of the peptide, i.e., the linker residue Ala-261 (*orange*) and the TM residue Ile-270 (*yellow*). In the bottom panel, the red spheres show the position-restrained water oxygen atoms that mimic the steric effect of a bilayer. In the bottom right figure, the black circle marks the two linker residues which spontaneously folded from loop into α -helical conformation.

The system containing the simplified bilayer, WT^S/VdW (Fig. 3.2 *bottom left*), was set up in a similar manner. The simplified bilayer served to reduce the conformational space available for the peptide due to the presence of the lipid bilayer and was created by position-restraining (Sec. 2.2.8) all water molecules in a 5 Å layer perpendicular to the TM helix (*red spheres*). In order to 'anchor' the peptide in this artificial membrane, also the backbone atoms of the TM helix were position-restrained. The linker conformation was changed such that the side chains of the linker and the H3 helix did not penetrate the membrane layer.

The two systems were minimized to remove possible strains of the x-ray structure

(Sec. 2.2.6) and possible van der Waals overlaps within the peptide due to unfavorable side chain conformations or overlaps between the peptide and misplaced water molecules. The systems were subsequently equilibrated at 300 K and a pressure of 1 bar (Sec. 2.2.4). Here, light hydrogen atoms (Sec. 2.2.5) and a time step of 2 fs were chosen. To calculate the non-bonded forces, the twin-range cutoff was used (Sec. 2.2.5). Snapshots of the system were recorded every 0.2 ps for further analysis.

As can be seen in Fig. 3.2 (*top*), in the absence of a membrane the solvated linker peptide folded within 1.1 ns (trajectory WT^S/–/300K) such that the H3 helix fragment contacted the TM helix fragment. Closer inspection revealed that the folding was driven by the hydrophobic contact between the H3-adjacent linker residue Ala-261 (*orange*) and the TM residue Ile-270 (*yellow*). The linker residues did not adopt any secondary structure. In contrast, when the simple membrane model was included (Fig. 3.2 *bottom*, *red spheres*) (trajectory WT^S/VdW/300K), the H3 adjacent linker residue Ala-261 spontaneously folded into α -helical conformation after about 350 ps, as did Arg-262 after 400 ps (*black circle*, Fig. 3.2 *bottom right*). Also, the orientation of the H3 helix remained stable and parallel to the TM helix. The helical conformation of Arg-262 appeared to be only marginally stable and it unfolded again after 1.2 ns.

The main conclusion from this pilot study is that the structure of the linker and the orientation and fluctuation of the H3 helix is presumably strongly affected by the presence of and interaction with the membrane. Therefore, a (computationally more expensive) explicit and accurate membrane model was used in all subsequent simulations.

3.2 Peptide with explicit lipid environment

In the simulation WT^S/VdW/300K (Sec. 3.1), after 0.3 ns two residues of the linker, namely Ala-261 and Arg-262, adopted an α -helical conformation (Fig. 3.2 *bottom right*, *black circle*) which remained stable for 0.9 ns. Therefore the linker structure after 1.2 ns was taken as the start structure of the first simulation with an explicit lipid environment, N₁₀^{TL}/POP⁰/300K (Fig. 3.1, *gray arrow*).

The simulated wild type peptide (WT) again comprised the five-residue linker, this time the full TM domain, and cytosolic residues of the H3 helix; it was embedded in an explicit lipid and solvent environment. Also a mutant prolonged by ten asparagine

residues (N_{10}) was studied. Fig. 3.3 shows the wild type peptide (WT) with the TM domain (Ile-266 – Gly-288, *yellow*), the 5-residue linker (Ala-261 – Lys-265, *red*), and the cytosolic H3 helix (Asp-250 – Lys-260, *cyan*) embedded within a explicit lipid (*green*) and a solvent (*blue*) environment. The phosphor, nitrogen, and oxygen atoms of the lipid molecules are pictured as spheres, whereas for the remaining part of the lipid and water environment bonds are shown as sticks (ions are not shown). The magenta rectangle indicates the position of the N_{10} prolongation.

The TM helix was modeled using MolMol;¹⁵⁶ the side-chain dihedrals were set to the default values provided by MolMol.

In order to avoid the creation of charges by the artificial truncation of the peptides at the N-termini, these were modeled neutral as NH_2 groups. The C-termini were modeled charged as COO^- groups. Similar to Sec. 3.1, the secondary structure of the H3 helix was stabilized by 1-4 distance restraints. The simulated peptides are characterized in Tab. 3.2.

Table 3.2: Simulated peptides

Peptide	N_r	Residues	q [e]	N_a
WT	39	250 – 288	+6	373
N_{10}	49	WT + Asn ₁₀	+6	483

A wild type peptide with a full TM domain (WT) and a prolonged mutant (N_{10}) were simulated. Given are the respective number of residues (N_r), the net charge (q), and the number of atoms (N_a).

This approach allowed to study not only the linker properties, but also the properties of the TM domain, such as membrane anchoring, TM helix tilt, and the stability of the TM helix.

3.2.1 Lipid environment

Biological membranes consist of a large variety of — mainly — lipid and protein molecules; their precise composition depends on the organelle or cell type which the membrane belongs to.¹ Phospholipids, the most abundant lipid molecules, consist of

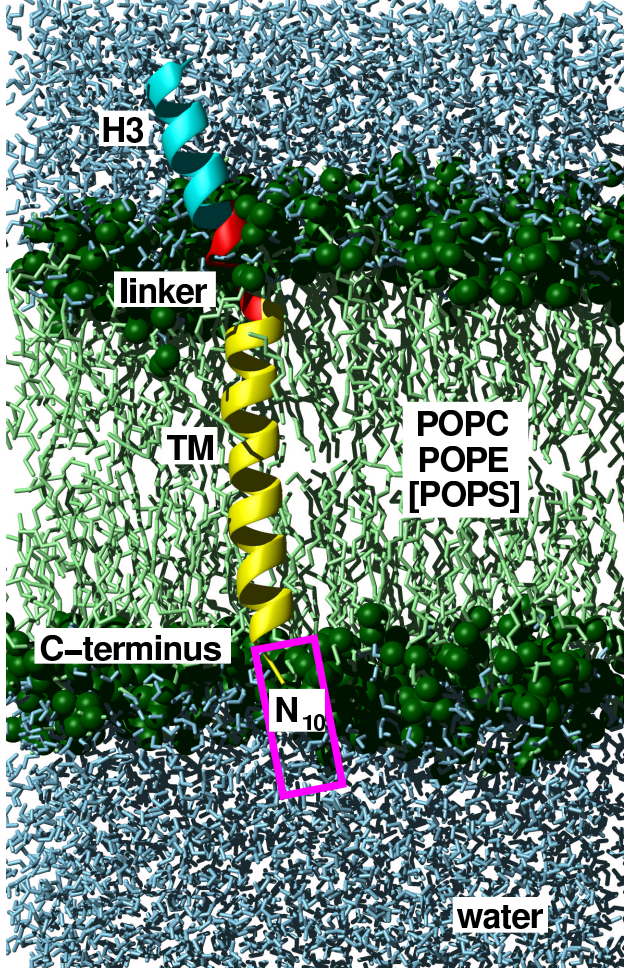


Figure 3.3: Simulation system setup. Shown is the C-terminal segment of syntaxin, comprising an 11-residue segment of the H3 helix (Asp-250–Lys-260, *cyan*), the 5-residue basic linker (Ala-261–Lys-265, *red*), and the 23-residue TM helix (Ile-266–Gly-288), embedded in a lipid bilayer (*green*, the green spheres indicate the phosphor, oxygen, and nitrogen atoms of the polar regions), with an explicit solvent environment (water molecules are shown in blue, ions are not shown). The magenta rectangle indicates the position of the 10-asparagine prolongation present in some of the simulations.

a hydrophilic headgroup and two hydrophobic hydrocarbon tails. The tails differ in length, typically between 14 and 24 carbon atoms; the 16- and 18-carbon chains are the most common ones. One tail usually has one or more *cis* double bonds (i.e., is unsaturated), which produces a bend, while the other tail has not (i.e., is saturated). The headgroup is typically zwitterionic or acidic.

In simulation studies of membrane proteins, the explicit lipid environment is usually composed of a single lipid species. To obtain a more realistic model, in the present work two mixtures of three abundant phospholipids were chosen (see Fig. 3.4). The respective lipid molecules each consist of a saturated 16-hydrocarbon chain (*palmitoyl residual*), an unsaturated 18-hydrocarbon chain with the *cis* double bond in the chain center (*oleoyl*), a glycerol, a phosphate (acidic), and an alcohol residue. The chosen alcohol residuals were choline, ethanolamine, and serine. Accordingly, the simulated lipids were palmitoyl-oleoyl-phosphatidylcholine (POPC) and palmitoyl-oleoyl-phosphatidylethanolamine (POPE), both zwitterionic and palmitoyl-oleoyl-phosphatidylserine (POPS), acidic, i.e., negatively charged at neutral pH.

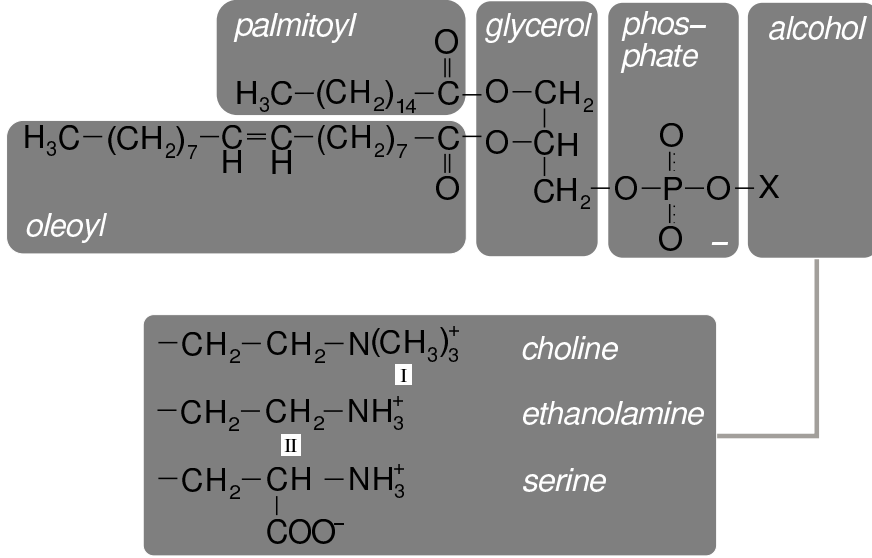


Figure 3.4: Chemical structure of simulated phospholipids. The roman numbers (*I* and *II*) indicate positions at which atoms were changed to mutate a given lipid into another one.

Tab. 3.3 specifies the two lipid compositions which were chosen to study the influence of the lipid environment on the peptide properties. As binary mixture of POPC and POPE a neutral bilayer (POP^0) was modeled. A more physiological^{1,157} acidic bilayer (POP^-) was modeled as a ternary mixture of POPC, POPE, and POPS molecules.

Bilayer	POPC	POPE	POPS	q [e]	N_a
POP^0	70	46	–	0	6032
POP^-	70	34	12	-12	6068

Table 3.3: Simulated bilayers. A neutral (POP^0) and an acidic bilayer (POP^-) were simulated containing the zwitterionic lipids POPC and POPE, and the acidic lipid POPS. The net charge of the bilayer is denoted by q , and the number of lipid atoms by N_a .

The POPC force field originated from Berger et al.,¹⁵⁸ parameters for the unsaturated carbons and the partial charges of the POPE headgroup were chosen from the GROMOS-87⁸⁸ force field.¹⁵⁹ The POPS force field was obtained as follows (cf. Fig. 3.4). Starting from the POPE force field, the CH_2 compound atom at position II was changed to a CH compound atom. To this atom, a COO^- group was appended. The partial charges (Fig. 3.5) were chosen from the serine force field for the

COO⁻ group and from the POPE force field for all other atoms. Lennard Jones, bond length, bond angle, and dihedral parameters were adopted from the POPE parameters, except those for interactions involving the changed compound atom or the added group; these were obtained via comparison with other chemical groups which are already parameterized in the GROMOS-87 force field.

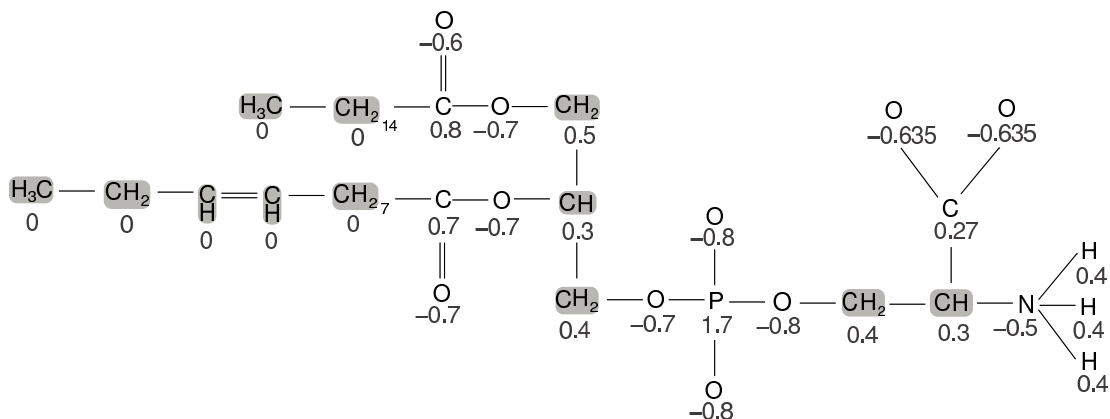


Figure 3.5: Chemical structure of POPS and associated partial charges which were derived from the POPE charges using serine as a template. The gray boxes indicate compound atoms.

3.2.2 Peptide insertion

3.2.3 Modeling

For the lipid environment, an equilibrated bilayer of 128 POPC molecules in a rectangular box, kindly provided by Peter Tieleman^{159,160} was used. For peptide insertion, a cylindrical hole of radius 7 Å was created by removing those four lipid molecules from each layer whose headgroups were located within the hole region. Subsequently, a weak repulsive and radially acting force centered at the vacated region was applied to the lipid molecules during a short MD run to drive any lipid tail atoms out of the cylinder into the bilayer.¹⁵⁹

Complete peptide insertion was prohibited due to severe steric conflicts between the linker of the peptide (Fig. 3.3, *red*) and several lipid headgroups (*green*); this hindrance could not be removed by minor changes of the backbone configuration of the three remaining non-helical residues. As a result, the TM helix protruded at its

N-terminal side into the polar region of the bilayer by about 5 \AA , whereas, at the C-terminus, a hole within the hydrophobic core of the bilayer of about the same length remained. A “prosequence” of ten α -helical asparagine residues, was appended to the C-terminus (‘N₁₀’ mutant). It was expected that the peptide would relax and shift downwards during the equilibration phase to fully bury the apolar TM residues in the hydrophobic core of the bilayer, such that the prosequence could then be removed. For the prosequence, the choice of asparagines was motivated by the expectation that their high polarity⁷ should drive them quickly out of the hydrophobic region of the bilayer. Furthermore, the neutral asparagines should disturb the system only slightly.

Two POPC molecules of each layer still overlapped with the peptide and were removed. The desired lipid composition of the neutral bilayer was obtained by mutating 46 uniformly distributed POPC into POPE molecules by changing the CH₃ compound atoms at position I (Fig. 3.4) into hydrogen atoms. The system was solvated for charge compensation (cf. Sec. 2.2.2). The composition of the system (N₁₀/POP⁰) is shown in Tab. 3.4.

Table 3.4: Simulation systems for production runs

Simulation system	Peptide	Bilayer	N_w	Ions	N_a	a	\times	b	\times	c
								[\AA]		
WT/POP ⁰	WT	POP ⁰	4718	6 Cl ⁻	20565	56.9	\times	61.8	\times	88.0
WT/POP ⁻	WT	POP ⁻	4725	6 Na ⁺	20622	56.5	\times	61.3	\times	84.2
N ₁₀ /POP ⁰	N ₁₀	POP ⁰	5292	6 Cl ⁻	22397	60.0	\times	61.8	\times	88.0
N ₁₀ /POP ⁻	N ₁₀	POP ⁻	5046	6 Na ⁺	21695	57.0	\times	61.8	\times	88.0

Peptides are specified in Tab. 3.2, bilayers in Tab. 3.3. Given are the respective number of water molecules (N_w), the number of atoms (N_a), and the initial box size ($a \times b \times c$).

3.2.4 Equilibration

The system was minimized and equilibrated for 5 ns at 300 K and 1 bar (N₁₀^{TL}/POP^{0/-}300K); the superscripts denote 1-4 distance restraints for the TM-helix (‘T’) and two linker residues Ala-261 and Arg-262 (‘L’). The simulation protocol was chosen similarly as in Sec. 3.1. Here, as in all subsequent simulations, heavy hydrogen atoms

were used such that a timestep of 4 fs could be chosen (cf. Sec. 2.2.5). Snapshots of the system were recorded every 0.4 ps for further analysis.

During the first 40 ps of the equilibration phase a fast relaxation motion perpendicular to the membrane surface was seen, where the peptide penetrated the bilayer by 2 Å (see Fig. 3.6); a slower relaxation by further 2.5 Å occurred during the subsequent 450 ps. In contrast to the simple membrane model used in the pilot study, the TM-adjacent linker residue Lys-265 folded into a stable α -helical conformation. This remarkable result is presumably due to the increased hydrophobicity of the lipid headgroup region¹⁶¹ which is now described more realistically than in the pilot study. As will be analyzed in more detail below, this interaction is indeed quite complex. During the subsequent 1.4 ns, after a temporal backward movement, the peptide finally moved further towards the membrane center by 0.5 Å and reached a stable position, which was apparently independent of the chosen start position. For the next 3.2 ns, only a slow drift is detectable, hence we assume the z -position of the TM-helix to be close to equilibrium. The motion of the peptide brought the linker into the polar region of the bilayer. The TM helix, initially perpendicular to the bilayer, stabilized at tilts around 10°.

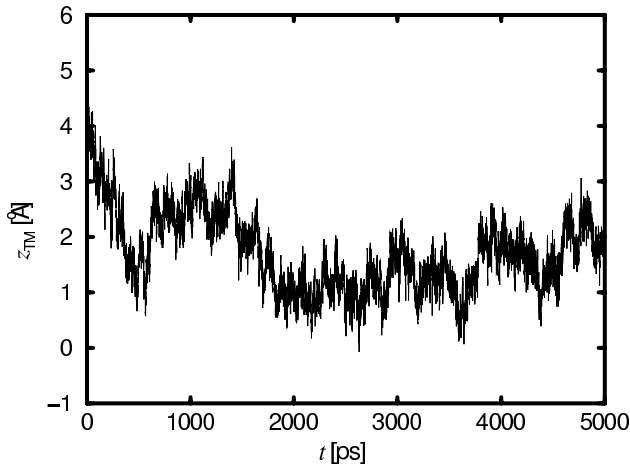


Figure 3.6: Relaxation motion of linker position perpendicular to the membrane surface with respect to average position of phosphate atoms during simulation $N_{10}^{TL}/POP^0/300K$.

3.2.5 Production runs

The set of the four possible combinations of lipid environment and peptide type (Tab. 3.4) was obtained from the final structure of the trajectory $N_{10}^{TL}/POP^0/300K$ (Sec. 3.2.4) as denoted in Fig. 3.1. The system N_{10}/POP^0 was transformed into WT/POP^0 by removing the prosequence and solvent environment, modeling a new C-terminus, and re-solvating the system.

The two POP⁰ systems (WT/POP⁰ and N₁₀/POP⁰) were transformed into respective POP⁻ systems (WT/POP⁻ and N₁₀/POP⁻) as follows: First the solvent environment was removed. Selected POPE molecules were changed into POPS molecules. The four basic linker residues Arg-262–Lys-265 were assumed to bind four acidic lipids, therefore four of the 12 POPS molecules were located in the vicinity of the linker; the remaining POPS molecules were chosen uniformly distributed. Subsequently the system was re-solvated, and ions for charge compensation were added by replacing selected water molecules in shells of radius 10 Å around oppositely charged groups ('Debye criterion'), and each of the modified systems was energy-minimized.

The four systems POP⁰ and POP⁻ with wild type and extended peptide (Tab. 3.4) were evolved in free dynamics simulations of 5 ns (*four blue boxes in Fig. 3.1*), using similar simulation protocols as those in Sec. 3.2.4 without 1-4 distance restraints on the linker and TM residues. Two final structures (taken from WT/POP⁰/300K and N₁₀/POP⁰/300K) served as starting structures for subsequent high temperature runs (*red boxes*).

A further room temperature simulation with the acidic lipid environment was performed. From the equilibrated system WT/POP⁻, a system with intracellular salt conditions (WT/POP⁻/SALT, see Tab. 3.5) was created by changing the Na⁺ into K⁺ ions and inserting excess K⁺ and Cl⁻ ions according to the Coulomb criterion. Here a more accurate calculation of the electrostatic forces was necessary; therefore the — computationally more expensive — PME method (Sec. 2.2.5) was used here.

In order to check for a possible bias of the chosen linker start structure, an independent line of simulations was performed. This started with simulation WT_H^{PD}/POP⁰/300K (Fig. 3.1 *second box, left column*) with the linker now modeled in fully α -helical conformation (subscript 'H'). As no steric hindrance occurred in the polar region and the peptide could be readily inserted, no membrane-stabilizing prosequence had to be appended. Otherwise, the simulation system was set up similar to N₁₀^{TL}/POP⁰/300K. To equilibrate the lipid environment, the peptide was first immobilized by position restraints on the backbone atoms of the TM domain (superscript 'P'). The superscript 'D' denotes a 1-4 distance restraints on the linker and the TM domain. In subsequent simulations, position restraints (WT_H^D/POP⁰/300K) and the distance restraints on the linker and the TM domain (WT_H/POP⁰/300K) were successively removed.

Table 3.5: WT peptide simulation systems for additional annealing runs

Simulation system	Bilayer	N_w	N_-	N_+	N_a	a	\times	b [Å]	\times	c
WT/POP ⁻ /SALT	POP ⁻	4697	11	17	20560	56.5	\times	61.3	\times	84.2
WT _H /POP ⁰	POP ⁰	4055	6	–	18576	65.8	\times	71.4	\times	107.1

The WT peptide is specified in Tab. 3.2, bilayers in Tab. 3.3. Given are the respective number of water molecules (N_w), the number of Cl⁻ (N_-) and K⁺ (N_+) ions, the total number of atoms (N_a), and the initial box size ($a \times b \times c$).

3.2.6 Linker stiffness

During the two WT simulations (WT/POP⁰/300K and WT/POP⁻/300K), two of the five linker residues remained in random coil configurations providing a hinge region between the H3 and the TM helix. Unexpectedly, visual inspection of the trajectories already suggested that the linker was quite stiff as opposed to, e.g., the highly flexible lipid tails. To quantify the stiffness, Fig. 3.7 A shows the H3 helix tilt θ during the WT simulations (*blue and green curve*). The red and magenta curves describe H3 helix tilts from N₁₀ simulations.

For the wild type peptide in the neutral bilayer (POP⁰, *blue curve*), after about 600 ps, the tilt angle stabilizes quickly at small values. For the acidic bilayer (POP⁻, *green curve*), the tilt angle starts at higher values and shows a slow drift, until, after 3 ns, it appears to be nearly equilibrated. Therefore the interval between 3 ns and 5 ns (*gray*) was chosen for the free energy estimates according to Eq. 2.21. The H3 helix tilts from the N₁₀ simulations are discussed below.

The obtained free energy landscapes are shown in Fig. 3.7 B. Both WT simulations show a narrow energy minimum located at small angles (*blue and green curves*); angles larger than 25° are rarely encountered. Accordingly, the H3 helix remains nearly parallel to the bilayer normal with a small average tilt angle and considerable tilt stiffness. To quantify these two properties, a harmonic potential (Eq. 2.22) was fitted to the observed ensemble of tilt angles θ using Eqs. 2.23 and 2.25 yielding equilibrium angles θ_0 and effective stiffnesses k_θ (see Tab. 3.6). Whereas the equilibrium angles are similar for the two WT simulations, the additional charges of the acidic bilayer (POP⁻) seem to increase the stiffness of the linker by a factor of two.

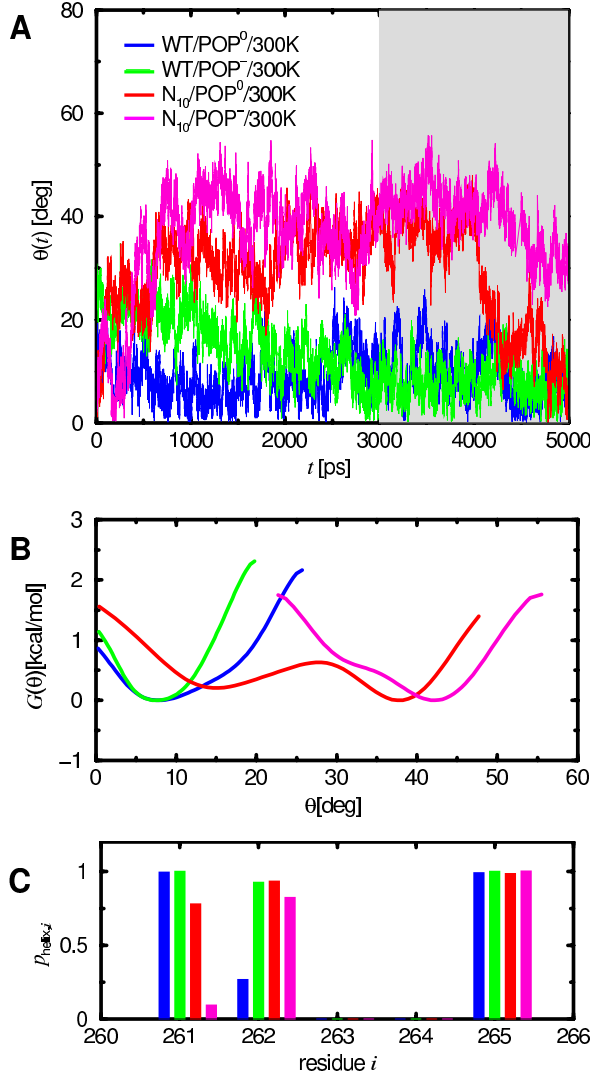


Figure 3.7: (A) Tilt angle θ of the H3 helix with respect to the bilayer normal during room temperature free dynamics runs of the wild type (WT) and the prosequence mutant (N₁₀), both embedded within uncharged (POP⁰) and charged (POP⁻) bilayer. The period which was used for the free energy landscape estimate, $G(\theta)$, is shaded gray. (B) Smoothed free energy landscape for the H3 helix tilt angle, derived from the four free dynamics runs of 2 ns length each, according to Eq. 2.21. (C) Linker helicities determined from the four 2 ns free dynamics runs. Shown are the relative frequencies $p_{\text{helix},i}$ that each of the five linker residues is in helical configuration, given that one of its neighbors is helical.

3.2.7 Effects of acidic lipids

In order to check if the increased stiffness for POP⁻ correlates with an increased linker helicity, the conditional probability p_i of helix formation in the presence of a helical neighbor residue was estimated for each linker residue i using Eq. 2.28 (Fig. 3.7 C). As can be seen, residues Ala-261 and Lys-265 are in a stable helical conformation for both bilayer types, whereas Arg-263 and Lys-264 remain in a random coil conformation. The only — albeit very pronounced — difference is seen for Arg-262, which is helical for POP⁻, but only marginally so for POP⁰. This suggests that the larger stiffness is caused by the increased helicity, which, in turn, is induced by the lipid charges. In particular, changing a single residue into helical configuration can increase the tilt stiffness of the H3 helix considerably.

Table 3.6: Parameters of harmonic fits

System	θ_0	k_θ	$\theta_{\text{TM},0}$	$k_{\theta,\text{TM}}$	$z_{\text{link},0}$	$k_{z,\text{link}}$	$z_{\text{TM},0}$	$k_{z,\text{TM}}$
WT/POP ⁰	9.9	25	16.7	71	-5.4	4.9	-3.8	4.7
WT/POP ⁻	8.1	50	12.9	74	-4.4	2.9	-3.0	4.0
N ₁₀ /POP ⁰	27.2	4.2	16.7	59	-0.03	2.6	0.75	3.1
N ₁₀ /POP ⁻	40	17	19.3	95	-1.7	3.7	-0.61	6.4

Parameters for H3 helix tilt (θ_0 , k_θ), TM helix tilt ($\theta_{\text{TM},0}$, $k_{\theta,\text{TM}}$), linker position ($z_{\text{link},0}$, $k_{z,\text{link}}$), and TM helix position ($z_{\text{TM},0}$, $k_{z,\text{TM}}$), as estimated by Eqs. 2.23 and 2.25. For θ and θ_{TM} , the equilibrium values are given in degrees and the force constants in $\text{cal mol}^{-1}\text{deg}^{-2}$. For z_{link} and z_{TM} , the equilibrium values are given in Å and the force constants in $\text{kcal mol}^{-1}\text{Å}^{-2}$. The definition of the observables is sketched in Fig. 2.4, the systems are listed in Tab. 3.4.

3.2.8 Effects of prolongation

The 5-ns simulations of the mutant (Sec. 3.2.5) both for neutral (N₁₀/POP⁰/300K) and for the acidic (N₁₀/POP⁻/300K) bilayer (Fig. 3.7 A, *red*, *magenta*) were carried out, as the tilt angle behaved quite differently already in the N₁₀^{TL}/POP⁰/300K run. This observation led us to suspect that the prosequence has a pronounced impact on the mechanical properties of the linker; due to the considerable distance between prosequence and linker region this effect was not expected.

Indeed, even though they start at small tilt angles, both systems show much larger angles and larger fluctuations than the wild type already after 800 ps. Straight-forward calculation of the respective free energy landscapes is complicated, due to the notorious sampling problem. In particular, the N₁₀/POP⁰ system (*red*) jumps back to smaller angles after 4.2 ns and remains in that (meta-stable) state for the remaining simulation, such that, due to insufficient statistics, the computed free energy landscapes (Fig. 3.7 B) have to be judged with care. In particular, the relative height of the two apparent minima cannot be estimated unless multiple transitions are observed. In Chap. 4 this problem will be approached more systematically by multiple simulated annealing runs.

Table 3.6 summarizes the results of the — in this case necessarily rough — harmonic fits to the ensembles of N₁₀ tilt angles. As can be seen, for the neutral bilayer the

average tilt angle of the linker of the mutant is about three times larger than that of the wild type, whereas the stiffness decreased by a factor of five — mainly due to the fact that two meta-stable states are encountered. For the acidic bilayer, an even larger (by a factor of four with respect to the wild type) average tilt is seen and the stiffness is about three times smaller. Although the individual fit parameters are likely not very accurate at the present stage of analysis, the qualitative difference between the mutant and the wild type is evident and thus deserves closer inspection.

In the following we studied the linker helicity for the mutant as possible cause for the changed stiffness (Fig. 3.7 *C*, *red*, *magenta*). For both bilayer types the conformations of Arg-263, Lys-264, and Lys-265 are similar to the WT systems. In contrast, the quite stable helical conformation of Ala-261 for the WT systems is destabilized for the mutant in both bilayers, particularly for N₁₀/POP[−] (*magenta*), which also showed the largest average tilt. Apparently, the helicity of Ala-261 and hence the stability of the backbone hydrogen bond between the backbone NH group of Ala-261 and the backbone CO group of Tyr-257 is a critical determinant for the spontaneous H3 helix tilt. The observed correlation is also seen in the time domain, e.g., for N₁₀/POP⁰. Here, the pronounced and abrupt decrease of the tilt angle from approx. 40° to 15° at 4200 ps (Fig. 3.7 *A*, *red curve*) followed, as shown in Fig. 3.8 (*black symbols*), a transition of Ala-261 from an equilibrium between helical and non-helical conformation to a stable helical one at 3070 ps where it remained for the rest of the trajectory. Also, at 3200 ps, Arg-262 (*gray curve*) folded into a stable helical conformation which was shown to be crucial for the H3 helix tilt stiffness in the wild type. Moreover, the observed sequence of events in this case rules out the possibility that helix formation is the *consequence* of tilt angle changes rather than their cause. Although an (unknown) common cause can not be strictly ruled out, we attribute for both mutant systems the increased average tilt and decreased tilt stiffness to the reduced linker helicity.

3.2.9 Linker embedding

The previous result that inclusion of a realistic membrane environment can change the helical content of the linker suggested a mechanism for the initially unexpected long-distance impact of the prolongation: By changing the *z*-position of the TM-helix, the prolongation could expose the linker region to a more hydrophilic environment and thereby destabilize the backbone hydrogen bond between Ala-261 and

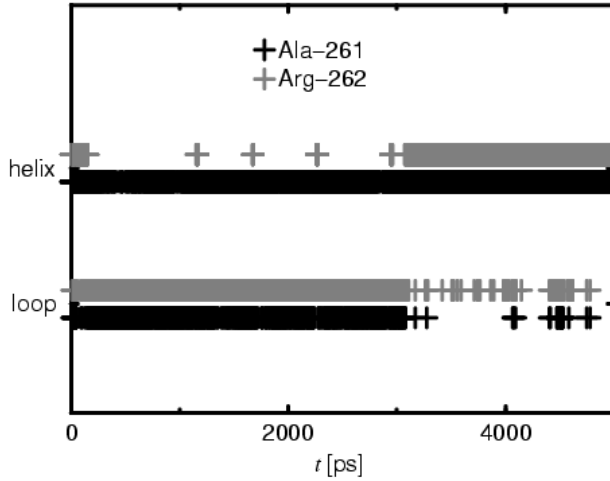


Figure 3.8: Secondary structure of residues Ala-261 (*black*) and Arg-262 (*gray*) during simulation N₁₀/POP⁰/–300K.

Tyr-257 which, in turn, affects the mechanical properties of the linker. To check this hypothesis, the vertical linker position z_{link} with respect to the average positions of the phosphor atoms of the proximate polar region (see Fig. 2.4) was monitored for all four systems and the respective free energy landscapes were determined using Eq. 2.21. As can be seen in Fig. 3.9 *A* and from the harmonic fits listed in Tab. 3.6 ($z_{\text{link},0}$, $k_{z,\text{link}}$) all four systems exhibit narrow energy minima; accordingly, the z position of the linker is well-defined. As expected, the position of the wild type (*blue*, *green*) is shifted with respect to that of the mutant (*red*, *magenta*) in such a way that the linker becomes buried deeper within the membrane, thus supporting our hypothesis. This effect is particularly strong for the neutral bilayer with a shift of 5.4 Å and less pronounced for the charged bilayer with a shift of 2.7 Å. Interestingly, compared to the neutral bilayer, the lipid charges shift the linker positions of wild type and mutant in opposite directions by approx. 1 Å. As shown in Tab. 3.6, the linker of the N₁₀ mutant is located roughly at the z -position of the phosphate groups, whereas the linker of the wild type resides unexpectedly deep in the membrane suggesting that the membrane environment strongly influences the linker properties in this case.

For POP[–], the difference of $z_{\text{link},0}$ between WT and N₁₀ is decreased as compared to the respective POP⁰ systems by a shift of 1 Å for WT and a shift of 1.7 Å for N₁₀ (see Tab. 3.6) towards intermediate values. This may reflect strong electrostatic interactions between the basic linker residues and acidic lipids which should be strongest near a particular linker position $z_{\text{link},\text{el}}$. This position apparently resides between the equilibrium positions of WT/POP[–] and N₁₀/POP[–], presumably closer to the value for WT/POP[–], as judged from the lower shift induced by the lipid

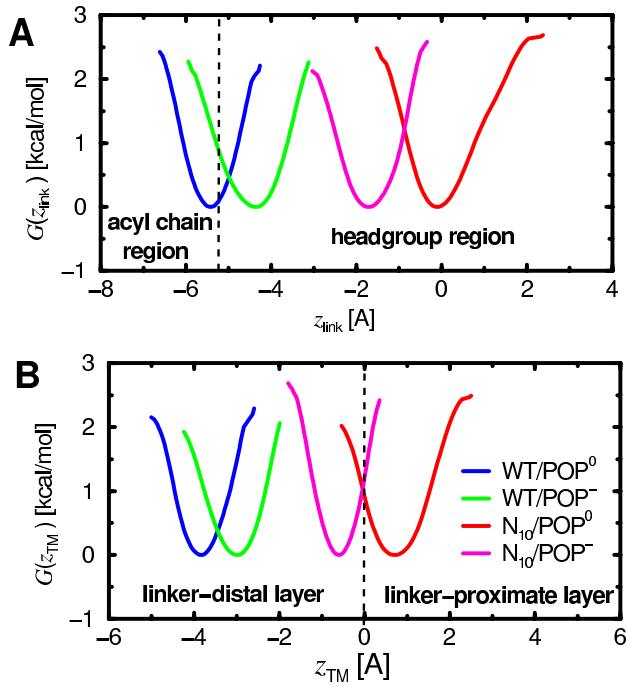


Figure 3.9: Smoothed free energy landscapes (A) for the linker position z_{link} with respect to phosphate groups and (B) for the position z_{TM} of the TM helix center with respect to membrane center (*dashed line*), both derived from the four free dynamics runs of 2 ns length according to Eq. 2.21. In (A), the polar region is indicated is defined via the distribution of phosphate group positions, using a cutoff (*dashed line*) at two standard deviations around the average position.¹⁶¹

charges for WT; i.e. $z_{\text{link,el}} \leq -3 \text{ \AA}$.

3.2.10 Hydrogen bonds

Generally, the lipid charges are expected to strengthen the interactions between the lipids and the peptide. On the other hand, the prolongation, reducing the peptide penetration, may weaken the peptide-lipid interactions (and thereby increase tilt flexibility). In order to check these hypotheses, the average number of hydrogen bonds between linker and H3 domain to surrounding lipid molecules, as well as its fluctuations (Eq. 2.30), were determined for each system. As shown in Fig. 3.10, the POP^- systems show indeed more frequent hydrogen bonding than the respective POP^0 systems. This may contribute to the increased tilt stiffness observed for the POP^- systems. For POP^- , a small decrease in the number of hydrogen bonds for N_{10} , as compared to WT, can be observed. For POP^0 , unexpectedly, the average number of hydrogen bonds between peptide and lipids is similar for WT and N_{10} .

3.2.11 Hydrophobic anchoring of the TM helix

Fig. 3.9 B shows that the observed shifts of the linker z -position are actually due to a shifted TM helix; the Figure shows the free energy landscape for position of the

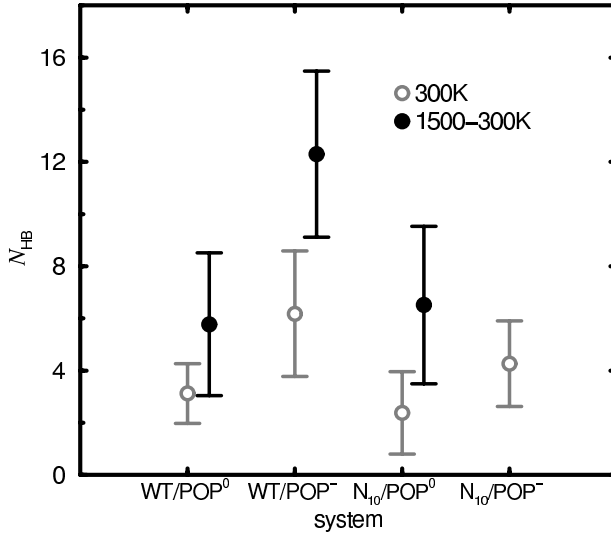


Figure 3.10: Average number N_{HB} of hydrogen bonds between the peptide (H3 and linker residues) and lipid headgroups determined from production phases of free dynamics runs, and from ensembles of annealing final structures. The bars denote fluctuations (Eq. 2.30). Note that the error bars are much smaller than these fluctuations.

TM helix center measured with respect to the membrane center (cf. also Fig 2.4). Indeed, the close similarity of Fig. 3.9, *B* and *A*, confirms that the TM domain is nearly rigid such that, as expected, the position of the TM helix within the bilayer determines that of the linker. Remarkably, the mutants hydrophobic TM helix is optimally centered within the hydrophobic region of the bilayer ($z_{TM} \approx 0$), whereas it is shifted out of this symmetrical position by 4 Å for the wild type. Apparently, there is a trade-off between the partial hydrophobic mismatch of the TM helix and the linker and the need to fill the hole in the distal lipid headgroup region which would be present for the symmetrical TM position. Therefore we assume that also many other hydrophilic prosequences with different structures would have similar effects as the one chosen here initially for purely technical reasons.

Table 3.6 lists the average positions $z_{TM,0}$ and stiffnesses $k_{z,TM}$ obtained from harmonic fits for the TM positions. As can be seen from the table, as well as from Fig. 3.9*B*, also the mutant, anchored in the neutral bilayer, is slightly shifted out of the symmetric position in the inverse direction by approx. 1 Å. One likely reason is the sequence asymmetry between linker and prosequence and, in particular, the presence of the four positive charges of the linker. That the asymmetry is inverted for the acidic bilayer, which changes the electrostatic environment of the linker, further supports the relevance of the interaction between linker and lipid headgroup region discussed above. The stiffnesses are, overall, very large, corresponding to a force of about 300 pN for a 1 Å deflection. Such stiffness is actually indispensable for the proposed membrane fusion mechanism, because it is required to keep the peptide tightly anchored within the bilayer, so that it can withstand the strong repulsion

forces that occur when two membranes are pulled towards each other.

3.2.12 TM helix tilt and structure

The second important requirement, as mentioned in the introduction, is that the TM helix must be able to withstand tilting with respect to the membrane normal. To study whether this is actually the case, free energy landscapes have been computed from the simulations also for the TM tilt angle θ_{TM} (see Fig. 2.4). Within the equilibration phase of the simulation ($\text{N}_{10}^{\text{TL}}/\text{POP}^0/300\text{K}$), θ_{TM} departed from its initially chosen value of 0° towards values around 10° (data not shown). The minima of the free energy landscapes (see Fig. 3.11) are significantly narrower than those of $G(\theta)$, indicating that θ_{TM} is more strongly restrained than θ . Table 3.6 lists the corresponding average tilts $\theta_{\text{TM},0}$ and the tilt stiffnesses $k_{\theta,\text{TM}}$ obtained from harmonic fits. Overall, the stiffnesses of the TM helix angle are larger than the ones of the linker angle, such that the mechanics should be mainly determined by the stiffness of the linker.

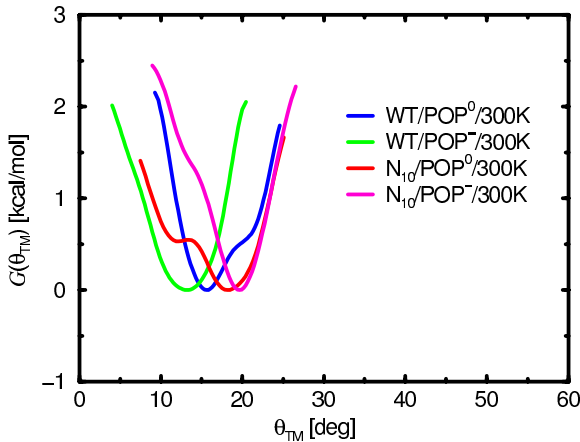


Figure 3.11: Free energy landscapes of TM helix tilt θ_{TM} with respect to the membrane normal from room temperature production runs.

Both the TM domain and the prosequence were initially modeled in α -helical configuration. To check if this configuration is maintained during the free dynamics runs, the secondary structures of the TM domain (residues 266-288) and of the prosequence (residues 289-298) were monitored (data not shown). For WT/ POP^0 (see Fig. 3.12 *left, gray bar*), the TM residues 266-286 remained helical, and only the C-terminal residues Phe-287 and Gly-288 adopted a random coil configuration. Also WT/ POP^- remained helical (*black curve*); only residue Gly-288 adopted a random coil configuration. Apparently, like for the linker residues, the lipid charges also increased the helicity of the TM C-terminus. For the N_{10} systems (see Fig. 3.12 *right*),

due to the juxtaposed prosequence, the entire TM domain remained α -helical for both lipid types. Also residues 289-294 of the prosequence showed a stable helix conformation; residues 295-296 were only marginally helical, and residues 297-298 adopted a random coil conformation. For N_{10}/POP^- (*black curve*), the helicity of residue Asn-295 and Asn-296 was increased with respect to N_{10}/POP^0 , thus providing a further example that the charged bilayer tends to stabilize helical conformations. Although the remaining helical structure of the prosequence was stable during the two 5-ns production runs, no solid evidence can be provided that this would also be true for longer time scales. The main effect of the (hydrophilic) prosequence of dragging the (hydrophobic) TM domain into a centered position should, however, not critically depend on the helical structure of the prosequence and therefore the predicted effect on the mechanical properties of the linker should be observable in experiments.

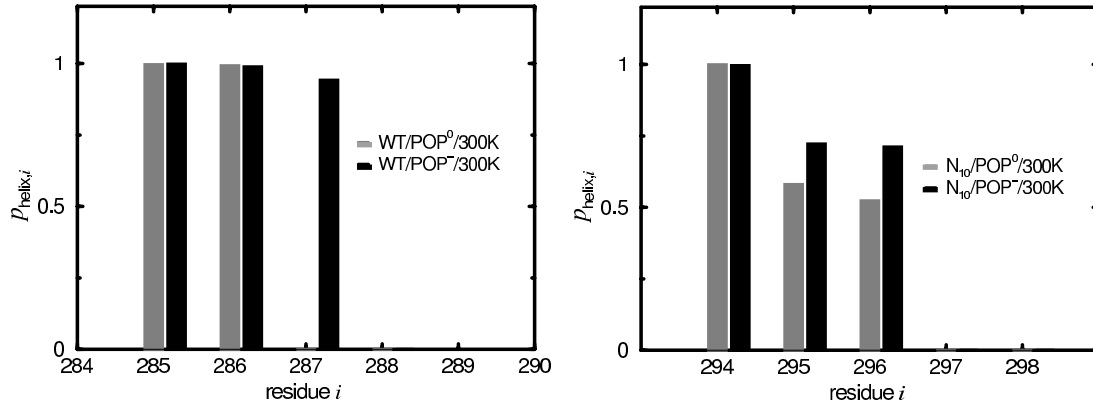


Figure 3.12: Helicity of C-terminal linker residues in production phase of wild type (*left*) and mutant (*right*) anchored in POP^0 (*gray*) and POP^- (*black*), respectively.

3.2.13 Immersion depths of individual residues

The linker position for the wild type agreed well with recent data from EPR measurements of Shin and co-workers.⁷⁶ In these experiments the positions of the syntaxin linker and nearby H3 and TM residues with respect to the phosphate groups of a lipid bilayer were determined from the accessibility of a nitroxide spin label to a water-soluble paramagnetic reagent and nonpolar oxygen by comparison to a standard sample (bacteriorhodopsin) with known immersion depths. The bilayer contained POPC and the acidic lipid palmitoyl-oleoyl-phosphatidylglycerol (POPG)

in a molar mixing ratio of 4:1, and therefore resembled the acidic bilayer (POP⁻) chosen for present simulations.

In order to compare the EPR measurements and the present simulation study in more detail, the average position of each C_α atom of the simulated peptide with respect to the phosphate atoms (immersion depth), as well as respective fluctuations (Eq. 2.30), during the 2-ns production phase of the wild type trajectories (WT/POP⁰/300K and WT/POP⁻/300K) were determined. As can be seen in Fig. 3.13 *left*, the results for the acidic bilayer (*black curve*) agree well with the EPR results (*brown curve*). In particular, both MD and EPR data show the whole linker region to reside below the phosphate groups. This suggests that the C-terminal end of the core complex sticks within the headgroup region, which might contribute to a strong coupling between the SNARE core and the membrane, as argued.⁷⁶

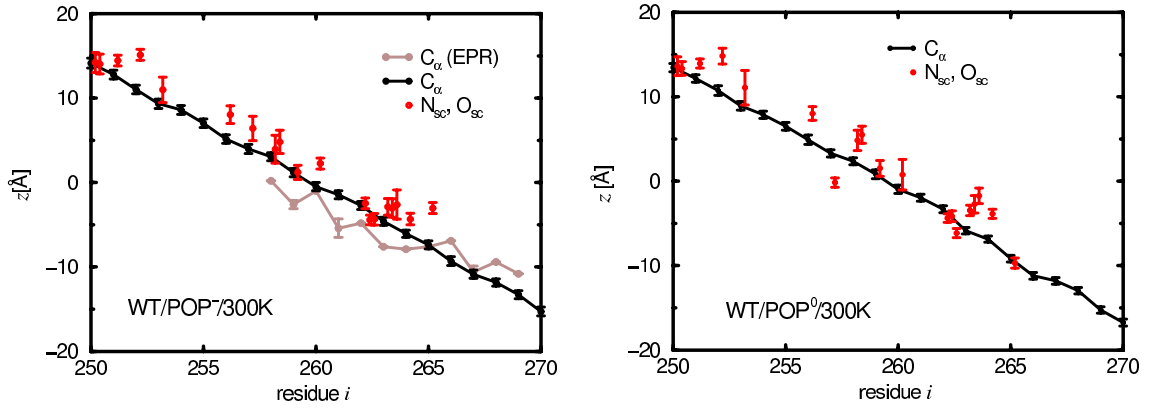


Figure 3.13: Average positions and respective fluctuations (Eq. 2.30) of C_α (*black*) and side-chain nitrogen and oxygen atoms ('N_{sc}', 'O_{sc}', *red*) during the 2-ns production phases of WT/POP⁰/300K (*left*) and WT/POP⁻/300K (*right*). In the right figure, also the positions of the residues as determined by EPR measurements⁷⁶ are shown (*brown*).

In the simulations, the average positions of most residues (258, 259, 261–264, 266) are shifted towards the aqueous phase by 1–2.5 Å. This effect may reflect an artifact of the EPR experiments;⁷⁶ here, as stated by the authors, due to the hydrophobic nature of the nitroxide, the peptide might be shifted towards the lipidic phase.

The EPR curve is shallower than the MD curve; this may indicate that the H3 and TM helix tilt was larger in the experiment than observed in the simulations. Furthermore, the MD simulations do not reproduce the plateau region for residues 263–266 which was seen in the EPR measurements and suggesting that, here, those linker and TM residues were unstructured.

The differences of the EPR and MD data might result from the different lipid compositions, or indicate artifacts of the simulations: Here, due to the sampling problem, the linker structure might not be fully relaxed towards the native structure. Alternatively, as denoted in Sec.1.3, the linker structure seen in the EPR experiments might not be the native structure, since the required mutations of the linker region, as well as the spin label itself, possibly altered the linker structure.

In order to monitor the positions of polar and charged groups of the side chains, average position and respective fluctuations were also determined for each side-chain nitrogen and oxygen atom (*red symbols*). Remarkably, as hypothesized,⁷⁶ the side chains of linker residues 263–265 orient such that the positively charged groups at the side-chain termini reside in a more hydrophilic environment than the C_α atoms from which they branch off; the strongest effect is seen for Lys-265. Also most polar or charged H3 residues show this 'snorkeling' effect which, apparently, facilitates the observed deep penetration of 'cytosolic' peptide domains into the membrane, relevant for its mechanical coupling to the SNARE core complex.

As shown in Fig. 3.13 *right*, for the neutral bilayer, except that here no snorkeling is seen for residues Tyr-257 and Lys-265, similar results for C_α (*black curve*) and side-chain nitrogen and oxygen positions (*red symbols*) are obtained as for the acidic bilayer.

Chapter 4

Simulated Annealing Results

Concerning the linker structure and tilt angle, the room temperature simulations suffer from an apparent sampling problem, as can be seen, e.g., from the fact that only one major structural transition is seen for N₁₀/POP⁰ (Fig. 3.7 A, *red* and Fig. 3.8). Thus one cannot exclude the possibility that the linker structures seen in the simulations could be biased by the chosen start structure. Furthermore, the physiological membrane fusion time scales are likely three orders of magnitude longer than the nanosecond simulation times.¹⁶² For these reasons, also the calculated average tilt angles and, in particular, the obtained stiffnesses, may be inaccurate due to insufficient sampling.

To reduce this problem and to improve the sampling, we have carried out high temperature runs followed by multiple simulated annealing runs (Fig. 3.1, *red boxes*) for different solvated peptide-membrane systems. Each annealing set consists of a high temperature (1500 K) sampling run (see Fig. 2.2, *brown curve*) and multiple annealing runs (*blue*) and was generated as follows. An equilibrated start system was stabilized by (a) position restraints on the TM helix backbone and lipid tail atoms using a force constant of 359 kcal mol⁻¹ Å⁻², (b) 1-4 distance restraints (Sec. 2.2.8) on the H3 and the TM helices (plus the prosequence if present) with a force constant of 837 kcal mol⁻¹ Å⁻², and (c) backbone dihedral restraints on the H3 and the TM helices (and of the prosequence, if present), and the ω angles (torsion of peptide bond C-N, Fig. 1.3 *left*) of the linker. Subsequently, for the high temperature sampling run, the peptide, each lipid type, the water molecules, and the salt ions were separately coupled to a heat bath of 1500 K using a coupling time constant of 10 ps, and simulated for 1 ns. To avoid expansion of the box due to vaporization

of the water, pressure coupling was switched off such that an isochorous ensemble was simulated. Because of the faster atomic motions at high temperature, a smaller integration time step of 2 fs had to be used.

As indicated by the green circles in Fig. 2.2, 27 structures were chosen from the sampling trajectory, each of which was cooled down to 300 K linearly in time within 400 ps (*sloped blue lines*), using a coupling constant of 0.1 ps. Subsequently, water molecules that had moved into the hydrophobic core of the bilayer were removed to provide a preferably well equilibrated lipid and solvent environment. The resulting 27 structures were equilibrated for 200 ps each (*horizontal blue lines*). In these simulations, all restraints except the 1-4 distance restraints on the H3 helix were removed, an integration time step of 4 fs was used, and pressure coupling was switched on. The 27 final structures thus obtained (*red crosses*) were used for further analysis.

As indicated in Fig. 3.1, simulated annealing runs were carried out for the systems WT/POP⁰, N₁₀/POP⁰ (Tab. 3.4), WT_H/POP⁰, and WT/POP⁻/SALT (Tab. 3.5). For the latter, the PME method (Sec. 2.2.5) was used for the calculation of the electrostatic forces, and a time step of 1 fs was chosen for the high temperature simulations. For WT/POP⁰, three different annealing periods (400, 800, and 1600 ps) were chosen using the same set of high temperature start structures.

The restraints on the TM helix are not expected to severely limit the sampling of the linker structure and the linker tilt angle, since the position z_{TM} of this helix along and its tilt θ_{TM} with respect to the membrane normal are expected to be much better sampled and show only small fluctuations as compared to the H3 helix tilt angle (cf. Figs. 3.9 A and 3.11). These assumptions are supported by results from recent measurements on the membrane immersion of the syntaxin linker⁷⁶ which are consistent with our results in Chap. 3.

Fig. 4.1 A shows the results of a set of WT/POP⁰ annealing runs (cf. Fig. 2.2) compared with the respective room temperature production trajectory (*blue*). Rather than the tilt angle θ , here the projection of the (normalized) H3 helix axis onto the xy bilayer plane has been plotted; the center corresponds to $\theta = 0^\circ$. As can be seen, the 1 ns 1500 K sampling run (*brown dots*) provided a much broader distribution of H3 helix orientations than the 2 ns room temperature production phase. Furthermore, the region covered by the room temperature run is only rarely visited within the sampling run, suggesting that the free energy of other regions is lower, at least at this high temperature. This finding can be explained by the fact that

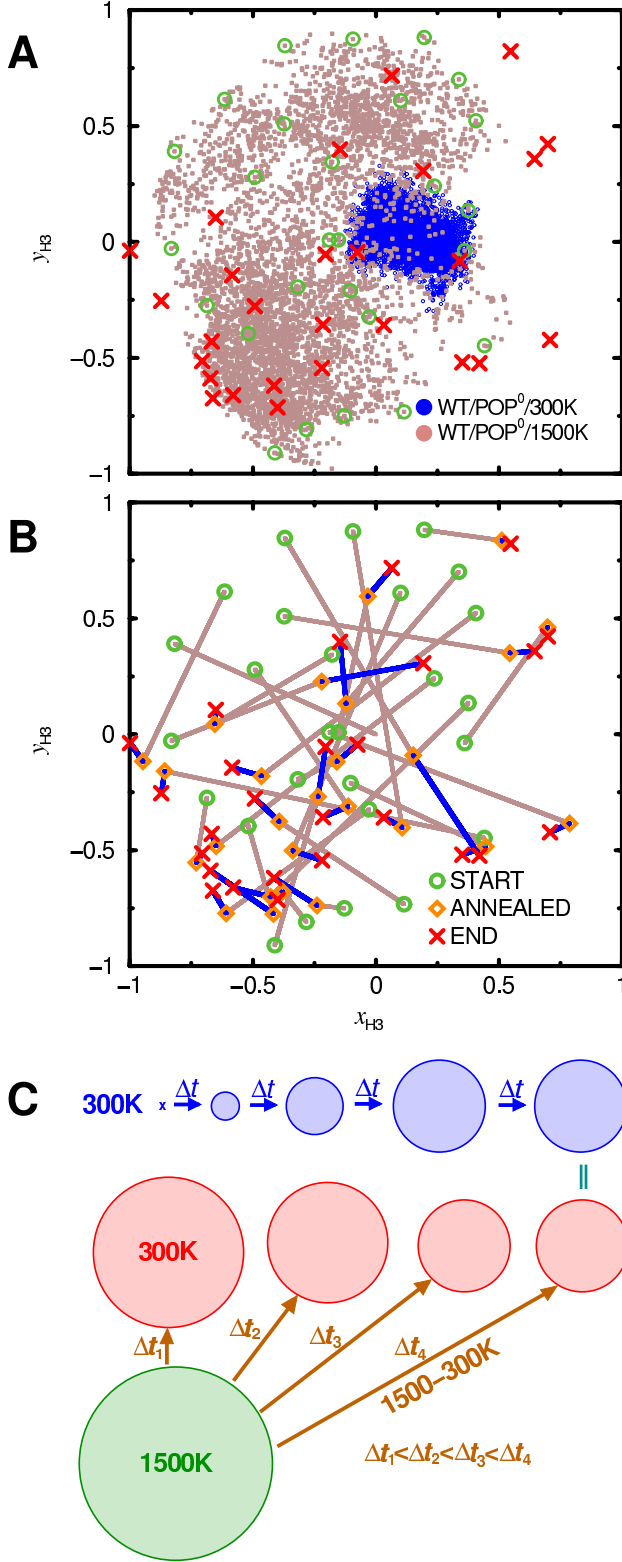


Figure 4.1: Projection of WT/POP⁰ H3 helix orientations (unit vectors) onto the xy bilayer plane, the azimuth is plotted relative to the TM helix. (A) 2ns room temperature trajectory (*blue*), high temperature trajectory (*brown*), selected annealing start structures (*green*), and obtained annealing and free dynamics final structures (*red*). (B) Distances traversed during individual annealing (*brown*) and equilibration (*blue*) phases. (C) Sketch of expected convergence behavior of room temperature dynamics and simulated annealing distributions. The circles symbolize distributions of H3 helix orientations, in a similar representation as in the top Figure. See text for explanations.

the distributions of H3 helix orientations are governed by respective *free* energy landscapes, $G = H - TS$, which, in addition to the enthalpic contribution H , also include temperature-dependent entropic contributions, $-TS$, which generally tend

to smoothen the distribution for increased temperatures.

4.1 Convergence

To approximate the room temperature distribution of interest, 27 uniformly distributed structures (*green circles*) were selected from the high temperature trajectory. Each of these was annealed to room temperature and subsequently subjected to free dynamics as described above. In Fig. 4.1 *A*, the obtained final structures are shown in red. The distances traversed during these two steps are shown in Fig. 4.1 *B* (*brown, blue*). If both the room temperature sampling and the relaxation during the annealing and subsequent room temperature runs were complete, the distribution of final structures (*red*) and of the room temperature trajectory (*blue*) should agree. In contrast, the annealing final structures show a relatively broad distribution with clusters similar to the high temperature distribution (e.g., within the lower left corner). Also several outliers are seen in regions that were not covered from the high temperature sampling run. Two or three structures reside within the region sampled by the room temperature run.

Fig. 4.1 *C* provides a possible explanation for these findings. With increasing simulation time (multiples of Δt), the room temperature distribution tends to broaden (and may also shift position), as indicated by the blue areas, as increasing volumes in the configuration space are sampled. Eventually, if the simulation time were long enough for sufficient sampling, the distribution would converge towards the equilibrium distribution (*right*). Thus, insufficient sampling typically underestimates the width of the equilibrium distribution and therefore yields an *upper limit* for the stiffness of the underlying effective potential. In contrast, and assuming that the sampling during the high temperature run is nearly complete, the obtained distribution (*green area*) will typically be broader than the equilibrium distribution due to the dominance of the entropic contribution to the underlying free energy landscape. This will also be true for the final structures of very short (Δt_1) annealing runs (*red area, left*) that started from structures taken from the high temperature ensemble. The structures cannot relax towards their room temperature equilibrium and rather get trapped in local energy minima. With increasing annealing periods $\Delta t_1, \Delta t_2, \Delta t_3, \Delta t_4$, increasingly complete relaxation takes place, and the width of the distribution narrows. For very long annealing periods, it would converge towards its

equilibrium value (*right*). Thus, for annealing, the equilibrium width will typically be approached from above which should yield a *lower limit* for the stiffness of the underlying effective potential.

To check if this setting applies for the case at hand, annealing sets with varying annealing periods ($t = 400, 800, 1600$ ps, cf. Fig. 3.1) were created. From the resulting sets of final structures, free energy landscapes were determined from Eq. 2.21. In contrast to the 5000 structures obtained from the room temperature ensembles, the annealing final sets provided only 27 structures each, thus limiting the accuracy and resolution of the obtained energy landscapes. But since subsequent annealing final structures should, by construction, be nearly uncorrelated (unlike subsequent structures from normal MD trajectories, which are highly correlated), accurate confidence intervals for the free energies can be calculated, using Eqs. 2.48 and 2.21.

4.2 Linker stiffness

Fig. 4.2 *A* shows the resulting free energy landscapes (*red, blue, and green*) for the three different annealing periods, together with 95 % confidence intervals. Additionally, to detect a possible bias by the chosen linker start structure, a fourth energy curve (*orange*) has been calculated from a separate series of simulations (Fig. 3.1, *top row*) which started with the linker in fully helical configuration. Overall, the energy minima show similar widths and tilt angles which are both considerably larger than those derived from the room temperature free dynamics run (*brown*). Fig. 4.2 *B* depicts these values as calculated, like the ones for the room temperature runs, from harmonic fits. Assuming uncorrelated data, 95% confidence intervals were estimated for θ_0 from Eq. 2.46 and for k_θ from Eqs. 2.47 and 2.25 and are also shown in the Figure.

As expected, increasing the annealing period from 400 ps (*blue curve*) to 800 ps (*green curve*) narrowed the derived energy landscape. However, a further increase to 1600 ps (*red curve*) *broadens* the width of the distribution to even above the 400 ps value. One possible explanation is that the sampling during the high temperature run was still insufficient and, therefore, is further improved during the annealing runs; the resulting broadening of the distribution could partially compensate the originally expected narrowing. The annealing final structure outliers (Fig. 4.1 *top left, red*) could in fact indicate regions that were accessible but not fully covered

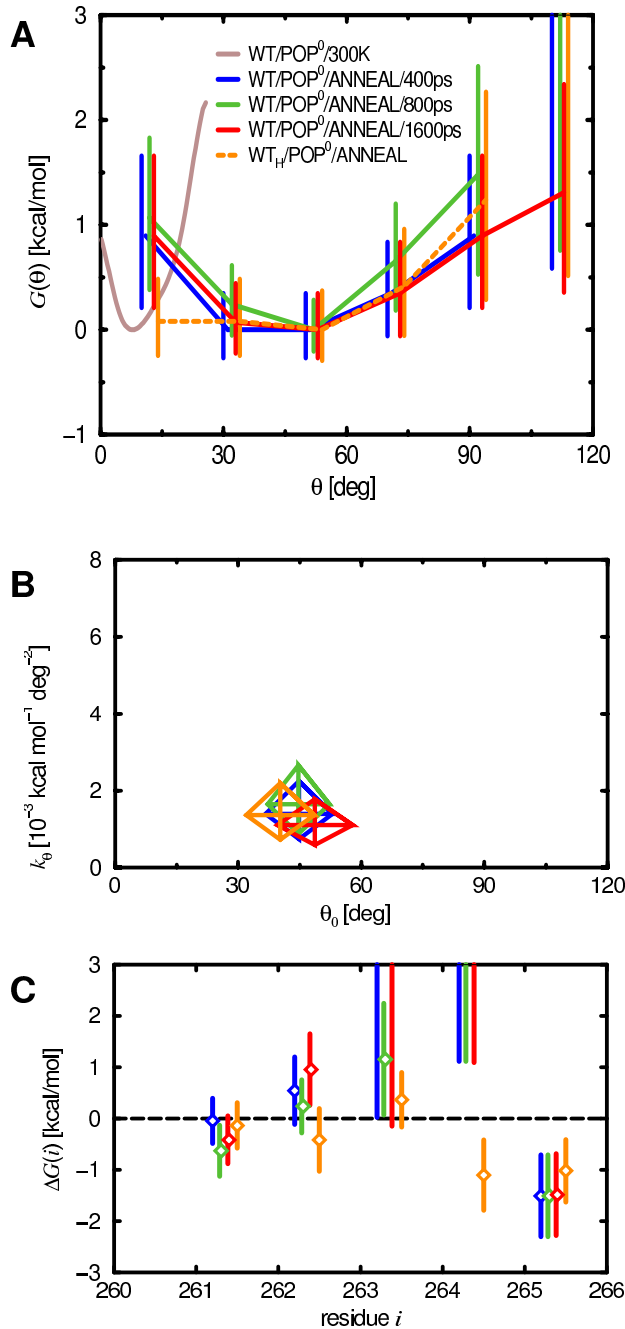


Figure 4.2: Influence of annealing lengths (*blue, green, red*), as well as partly and fully helical linker start structure (*blue, orange*) on structure and mechanical properties of the linker for WT/POP⁰, obtained from the final structures of respective simulated annealing sets. (A) Free energy landscapes for H3 helix tilt estimated using Eq. 2.21, with 95% confidence intervals from Eq. 2.48; for comparison, the free energy landscape obtained from the room temperature simulations is also shown (*brown*). (B) Parameters θ_0 and k_θ of harmonic fits to H3 helix tilt θ ; the centers of the rhombi indicate estimates according to Eqs. 2.23 and 2.25, the diagonals 95% confidence intervals for θ_0 (Eq. 2.46) and k_θ (Eq. 2.47). (C) Free energy of helix formation as estimated from Eq. 2.27, with 95% confidence intervals as estimated from Eqs. 2.48 and 2.27.

during the high temperature sampling run. However, the large overlap of the error bars in Fig. 4.2, A and B suggests, at this point of analysis, statistical fluctuations as the more likely explanation. Indeed, when estimated using the bootstrap mean and variance test respectively (Sec. 2.4.2), the significances of the pairwise differences for θ_0 and k_θ (Tab. 4.1, *left two columns*) turn out to be rather low (i.e., large α -values, Sec. 2.4) for the three different annealing lengths (*upper three rows*). In this case, the mechanical linker properties obtained from the annealing sets may either be

already close to their equilibrium values, or alternatively, their convergence might be so slow that even for an increase of the sampling time by a factor of four, no improvement can be detected.

Table 4.1: Significances of H3 helix tilt and linker helicity differences

$t_{\text{cool},1}$	\leftrightarrow	$t_{\text{cool},2}$	θ_0	k_θ	p_{261}	p_{262}	p_{263}	p_{264}	p_{265}
400	\leftrightarrow	800	0.98	0.61	0.13	0.51	0.63	1.00	1.00
800	\leftrightarrow	1600	0.49	0.33	0.66	0.12	0.63	1.00	0.91
400	\leftrightarrow	1600	0.52	0.62	0.26	0.46	1.00	1.00	0.91
WT/POP ⁰	\leftrightarrow	WT _H /POP ⁰	0.42	0.67	0.74	0.04	0.19	0.00	0.35
WT/POP ⁰	\leftrightarrow	WT/POP ⁻	0.02	0.03	0.13	0.00	0.61	1.00	0.03
WT/POP ⁰	\leftrightarrow	N ₁₀ /POP ⁰	0.20	0.55	0.32	0.59	0.30	0.01	0.00

Respective *alpha*-values (Sec. 2.4) for various pairs of annealing sets, as estimated by applying the appropriate bootstrap hypothesis tests described in Sec. 2.4.2. The mean test was used for the average tilt θ_0 , the variance test for tilt stiffness k_θ , the probability test for helicity p_i of residue i ($i = 261, \dots, 265$). The upper three lines list pairs obtained for system WT/POP⁰ with various annealing lengths; the lower three lines list comparisons of the 400 ps WT/POP⁰ annealing set with the specified sets.

In summary, the stiffness values shown in Fig. 4.2 *B* provide a lower limit for the tilt stiffness which is smaller than the upper limit obtained from the room temperature run by a factor of 15. We note that also the values for the other stiffnesses listed in Tab. 3.6 represent, in principle, upper limits. For $k_{\theta,\text{TM}}$, $k_{z,\text{link}}$, and $k_{z,\text{TM}}$, however, we have already seen above that the sampling is expected to be nearly complete, so that the obtained values should already be close to their equilibrium values. This suggests that no further simulated annealing runs for these observables are required.

The average tilt angle θ_0 (approx. 40°) obtained from the annealing runs is four times larger than the one obtained from the room temperature run. We attribute this difference to an entropic effect: For given tilt interval centers at θ , the accessible solid angle increases with θ as $\sin \theta$, implying larger entropy. Thus, for higher temperatures, the minimum of the free energy landscape tends to move to larger tilt angles, which may not fully relax to the room temperature values during annealing. Therefore, we consider it likely that the average tilt angle for the wild type is smaller than 40° .

Note finally that rarely H3 helix tilt angles above 90° are obtained for annealing runs, which give rise to the finite free energy values at 105° in Fig. 4.2 A. Under physiological conditions, the presence of the cytosolic core complex, which is not included in our simulations, prohibits such large tilts.

4.3 Linker structure

To characterize the linker structure, for each linker residue i , the probability p_i and the free energy ΔG_i of helix formation were estimated from the ensembles of final structures of different annealing sets using Eq 2.27. Assuming uncorrelated data, confidence intervals were determined from Eqs. 2.48 and 2.27. As shown in Fig. 4.2 C, the annealing yielded a quite similar helicity pattern as the one obtained from the respective room temperature run (Fig. 3.7 C, *blue bars*). An exception is Ala-261, which was helical in the room temperature run but only marginally so for the annealing sets. Given the large difference in $G(\theta)$ between the room temperature and annealing sets, the fact that only a single amino acid is affected is remarkable. The results obtained for WT/POP⁰ and N₁₀/POP⁰, however, reveal a similar trend namely that reduced helicity of Ala-261 implies increased average angle θ_0 and reduced tilt stiffness k_θ . Moreover, the change in helicity between WT/POP⁰ and N₁₀/POP⁰ is smaller for the room temperature simulations than for the annealing runs and so is the change in the mechanical properties of the linker (see below).

The linker properties obtained from annealing sets of varying length were found to change only slightly. However, also here, comparison of Ala-261 helicity (Fig. 4.2 C, *left*) with the tilt parameters (Fig. 4.2 B) reveals the same trend as seen above. Some of the individual α -values for the difference in helicity of Ala-261 and Arg-262 (Tab. 4.1) show even larger significances (albeit still above the 5%-level) than those for the tilt parameters. Moreover, also the helicities of Arg-262 and Arg-263 follow this trend, so that the joint significance should be well below 5%. Overall, the helicities of the individual linker residues are a more sensitive indicator for changes in the simulation set-up than the mechanical properties of the linker.

As seen for the linker parameters (Fig. 4.2 B), also the helicities show no monotonous variation with the length of the annealing periods, presumably for similar reasons, namely a near compensation of the effects of enhanced high temperature sampling

(which decreases the helicity) and of improved low temperature relaxation (which increases the helicity). Because the helicities of *all three* linker residues (Ala-261, Arg-262, and Arg-263) increase from WT/POP⁰/ANNEAL/400ps to WT/POP⁰/ANNEAL/800ps, whereas they collectively decrease from WT/POP⁰/ANNEAL/800ps to WT/POP⁰/ANNEAL/1600ps, the former change is likely dominated by improved relaxation and the latter by enhanced sampling. We note that the same was seen for the mechanical properties of the linker which renders it unlikely that these results are purely due to statistical fluctuations, and thus substantiates the compensation argument tentatively given above.

That the helicities obtained from the room temperature simulations and the ones from the annealing sets are strikingly similar can have two reasons. First, both approaches could yield structures close to equilibrium; second, there may be a bias due to the chosen (non-helical) start structure. The simulations starting with fully helical linker conformation served to detect such possible bias (Tab. 3.5, WT_H). The initial room temperature equilibration run (WT_H/POP⁰/300K, see Fig. 3.1) showed transitions to random coil and back to helical configurations (data not shown). Fig. 4.2 *C* shows the helicities obtained from the subsequent annealing set (*orange*). Comparison to WT/POP⁰/ANNEAL (*blue*) shows a significantly increased helicity particularly for Lys-264 (see Tab. 4.1 for the respective α -value), which renders a certain bias due to the chosen start structure indeed very likely for this residue. A small influence is also seen for Arg-262 and Arg-263. Nearly unaffected by that possible bias are the other helicities and, most importantly, the energy landscape for the tilt angle, $G(\theta)$, (Fig. 4.2 *A*, *orange*) and hence also the linker tilt stiffness k_θ (cf. Fig 4.2 *B*). This finding confirms the previous observation that the mechanical properties of the linker are mainly determined by the conformation of Ala-261 and underscores the reliability of the stiffness estimates.

We note that the confidence intervals and significance estimates discussed above rely on the assumption of uncorrelated samples. To check this assumption, for each annealing set (see Fig. 2.2), the correlation of subsequent start structures (*green*) and final structures (*red*) was estimated using Eq. 2.58, as well as the significance of this correlation using the bootstrap correlation test (Tab. 4.2). Indeed, WT/POP⁰ turns out to yield nearly uncorrelated structures, whereas WT_H/POP⁰ does show significant correlations for both start and final structures. We attribute these correlations to the increased linker helicity which can slow down the dynamics of the H3 helix tilt angles. Since the observed correlations of about 0.5 reduce the respective

effective sample size by roughly a factor of two, the confidence intervals and α -values calculated above are actually larger by a factor of about $\sqrt{2}$. This effect reduces the bias discussed above somewhat.

Table 4.2: Correlations of H3 tilt angles

System	r_s	p_s	r_e	p_e
WT/POP ⁰	0.13	0.52	0.12	0.65
WT _H /POP ⁰	0.77	0.00	0.28	0.19
WT/POP ⁻	0.39	0.07	-0.34	0.08
N ₁₀ /POP ⁰	0.44	0.02	0.47	0.01

Correlations of tilt angles from subsequent start (r_s) and end structures (r_e) from four different annealing sets (Eq. 2.58) and respective α -values estimated from the bootstrap correlation test.

We summarize the results obtained so far from the annealing runs. For the wild type embedded within neutral bilayer, the linker is helical at its termini with decreasing helicity towards the linker center. As evident from Fig. 4.2 *A*, and using Eq. 2.26, an energy of about 0.9 kcal/mol (with 95% confidence interval [0.5,1.8] kcal/mol) is required to tilt the linker to 80° which is the angle expected for fully assembled *trans*-complex geometry.

4.4 Effects of acidic lipids

To study the effects of the lipid composition on the mechanical properties of the linker, a set of high temperature and annealing runs was carried out also for system WT/POP⁻/SALT (WT/POP⁻/ANNEAL, see respective red box in Fig. 3.1). The obtained energy landscape for the H3 helix tilt angle (*green curve*, Fig. 4.3 *A*) shows, compared to WT/POP⁰ (*blue curve*), a very steep minimum which is located at a large tilt angle. The parameters of the harmonic fit (see Fig. 4.3 *B*, *green rhombus*) quantify this effect. The tilt stiffness k_θ is larger by about a factor of 2.5, which confirms the increase by a factor of two that was already obtained from the room temperature simulations (see Tab. 3.6). As compared to WT/POP⁰ (*blue rhombus*),

the average tilt angle θ_0 is larger by 15° . Table 4.1 shows that this effect of the lipid charges on the linker properties is significant.

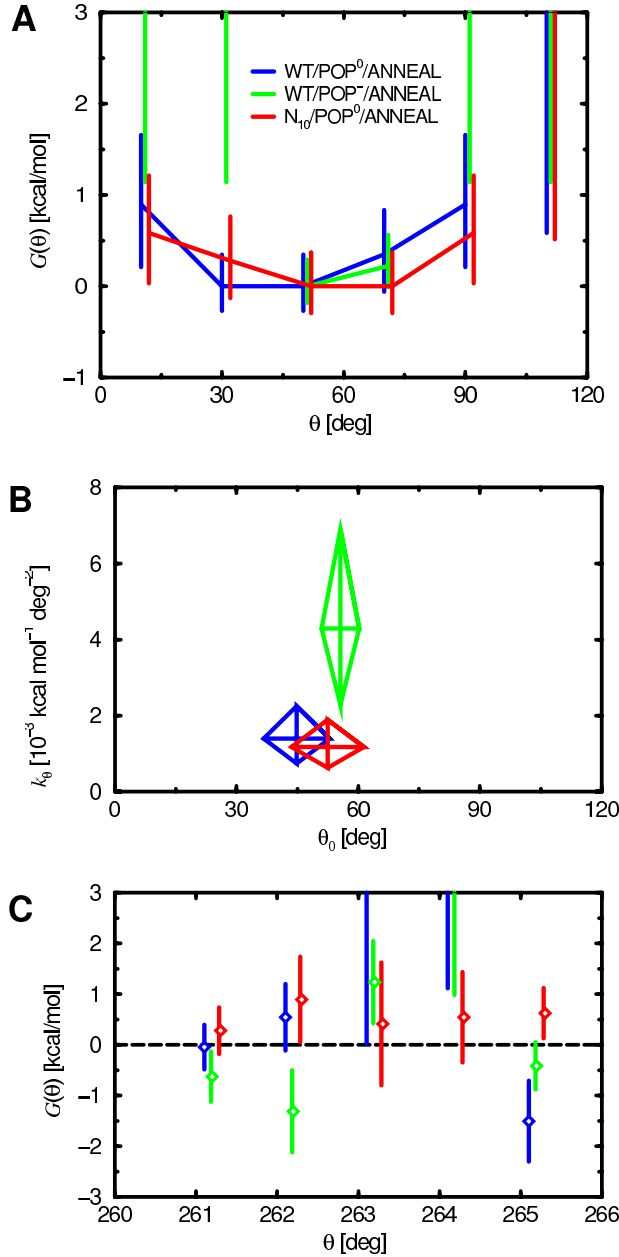


Figure 4.3: Structure and mechanical properties of the linker for WT embedded in POP⁰ (blue) and POP⁻ (green), as well as for N₁₀/POP⁰ (red). (A) Free energy of H3 helix tilt angles, (B) average H3 helix tilt θ_0 and tilt stiffness k_θ . (C) Free energy of helix formation.

These tilt property changes are related to changes in linker structure as shown in Fig. 4.3 C (green symbols). Similar to the room temperature runs (Fig. 3.7 C, green bars), as compared to WT/POP⁰ (Fig. 4.3 C blue symbols), the helicity of Arg-262 is significantly increased. The helicity of Ala-261 is also larger, in agreement with the room temperature simulations, whereas the helicity of Lys-265 is smaller. At this point of analysis, the latter finding may, as shown in Fig 4.4, be explained by the reduced peptide penetration (by approx. 1 Å) seen for the charged bilayer system

(*black, solid*) with respect to the neutral bilayer (*black, dashed*); the gray curve (as also Tab. 3.6) shows that this effect is insensitive to salt concentration. This could mean that the larger average tilt angle is due to the changed conformation of Lys-265 and that the larger helicity of Ala-261 and Arg-262 dominates the stiffness increase of the linker. An alternative explanation for the increase of the average tilt angle will be discussed in Sec. 4.6.

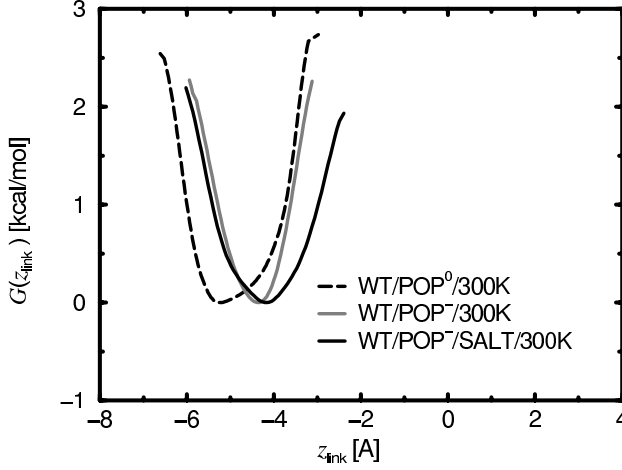


Figure 4.4: Free energy landscape $G(z_{\text{link}})$ of linker position z_{link} with respect to lipid phosphates for WT embedded in POP^0 (*black, dashed*) and in POP^- with low (*gray*) and physiological (*black, solid*) salt concentration, respectively.

In light of the conformational coupling assumption, the increase of θ_0 is expected to reduce fusion efficiency, whereas the increase of k_θ should have the opposite effect. To judge which of the two effects dominates, the energy necessary to tilt the H3 helix to the 80° expected for the fully assembled *trans*-complex was estimated. Compared to POP^0 , a slightly increased tilt energy of 1.2 kcal/mol was obtained with a 95 % confidence interval of [0.8, 2.4] kcal/mol (see Fig. 5.1) which suggests an increased fusion efficiency. Although the error bars overlap, these results may indicate an effect which should be looked on more closely in further studies.

4.5 Effects of prolongation

A set of high temperature and annealing runs as described above was carried out also for system $\text{N}_{10}/\text{POP}^0$ to study the effect of the prosequence on the linker stiffness (see Fig. 3.1). Here, the main effect is a shift of the obtained energy landscape for the tilt angle to larger values (Fig. 4.3 A, *red curve*) as compared to WT/POP^0 (*blue curve*). This is reflected in the increased average tilt angle obtained from the harmonic fit (Fig. 4.3 B, *red*), which was also seen for the room temperature simulations. The tilt stiffness is unchanged.

The relation between decreased helicity of Lys-265 (Fig. 4.3 *C*, *red*) and increased average tilt follows the same pattern as seen for the charged bilayer and therefore provides a plausible cause of the increased tilt. Furthermore, the helicity of Ala-261 is also reduced with respect to the wild type (neutral bilayer), albeit with only little significance, see Tab. 4.1. On the contrary, the helicity of Lys-264 and, to a smaller extent, that of Arg-263 became larger.

Overall, the helix is significantly weakened at the linker ends and stabilized for the central residues. Here, the change of the linker environment is solely due to the reduced peptide penetration (Fig. 3.9 *A*, *red curve*) rather than the charged bilayer but has an even larger effect on the structure of the linker. Table 4.2 lists the correlations of subsequent annealing structures which fall into the range discussed for the other annealing sets with similar implications for the confidence intervals and α -values.

Qualitatively, the changes of the linker structure seen in the annealing runs confirm and extend those of the room temperature simulations. In the context of the conformational coupling assumption, the energy required to tilt the H3 helix into *trans*-complex configuration of 0.4 kcal/mol ([0.2, 0.8] kcal/mol) is considerably reduced with respect to the wild type by more than a factor of two, which suggests a correspondingly reduced fusion rate.

4.6 Hydrogen bonds

To further characterize the interaction between the peptide and its environment, the average numbers N_{HB} of hydrogen bonds between H3 helix/linker residues and adjacent lipid molecules, as well as the respective fluctuations, were determined for the final structures of the three annealing sets discussed above. As can be seen in Fig. 3.10 (*black symbols*), N_{HB} increased by a factor of two for each system with respect to the room temperature runs. In particular, many of these additional hydrogen bonds are formed by the H3 helix due to the occurrence of large helix tilt angles and the resulting penetration of the helix into the bilayer. Particularly many hydrogen bonds are seen for the charged bilayer, and no significant difference between WT and N₁₀ is observed, as was also the case for the room temperature simulations.

To obtain a more detailed picture, the hydrogen bond probability of each donor

and acceptor respectively, of the linker and of the H3 helix, was determined (here, equivalent hydrogen atoms such as the three hydrogen atoms of an amino group were not distinguished). This probability is color-coded in Fig. 4.5, which shows a representative structure from the annealing final ensemble of WT/POP⁰. The colors denote frequent (*red*), intermediate (*yellow, green*), and rare (*blue*) bonding, respectively. As can be seen, virtually all polar residues of the H3 helix and of the linker form hydrogen bonds to the lipid molecules. These are particularly frequent for side-chain amino groups of residues Lys-260 and Arg-262 which are centered within the polar region of the bilayer, and gradually decrease in frequency with increasing distance from these residues. Linker residues also form backbone hydrogen bonds to the lipid molecules, which compete with the helix-stabilizing intramolecular hydrogen bonds like in bulk water and, therefore, destabilize the helix, albeit to a lesser extent.

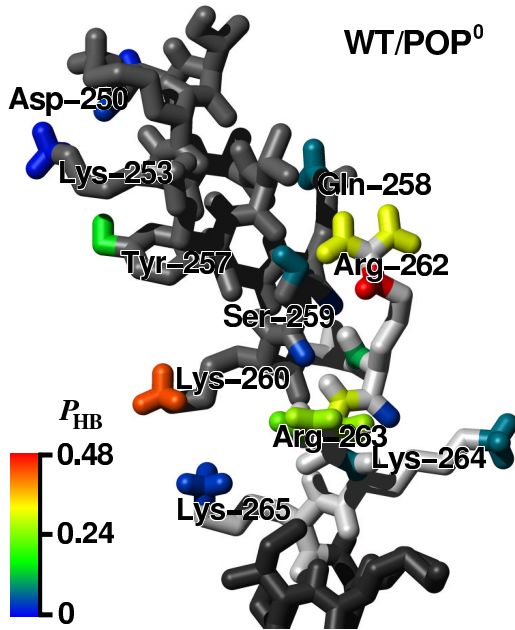


Figure 4.5: Color-coded frequencies p_{HB} of hydrogen bond formation between the H3 helix (*gray, top*) or the linker region (*light gray, mid*), respectively, and adjacent lipid molecules (not shown). The structure is taken from the WT/POP⁰ annealing set (final structure) and is close to the average orientation. Part of the TM helix is shown in dark gray (*bottom*).

To identify significant differences of observed hydrogen bonding frequencies seen for WT/POP⁻ (see Fig. 4.6 A) and N₁₀/POP⁰ (see Fig. 4.6 B) with respect to WT/POP⁰, for each acceptor and donor respectively, the significances of the observed probability differences were calculated using the bootstrap probability test. The colors denote decreased bonding frequency (*red, yellow*), or increased frequency (*green, cyan*), respectively. In the Figure, representative structures are shown. Overall, WT/POP⁻ shows increased hydrogen bonding frequencies, particularly so for the side-chain amino groups of Arg-263, Lys-264, and Lys-265.

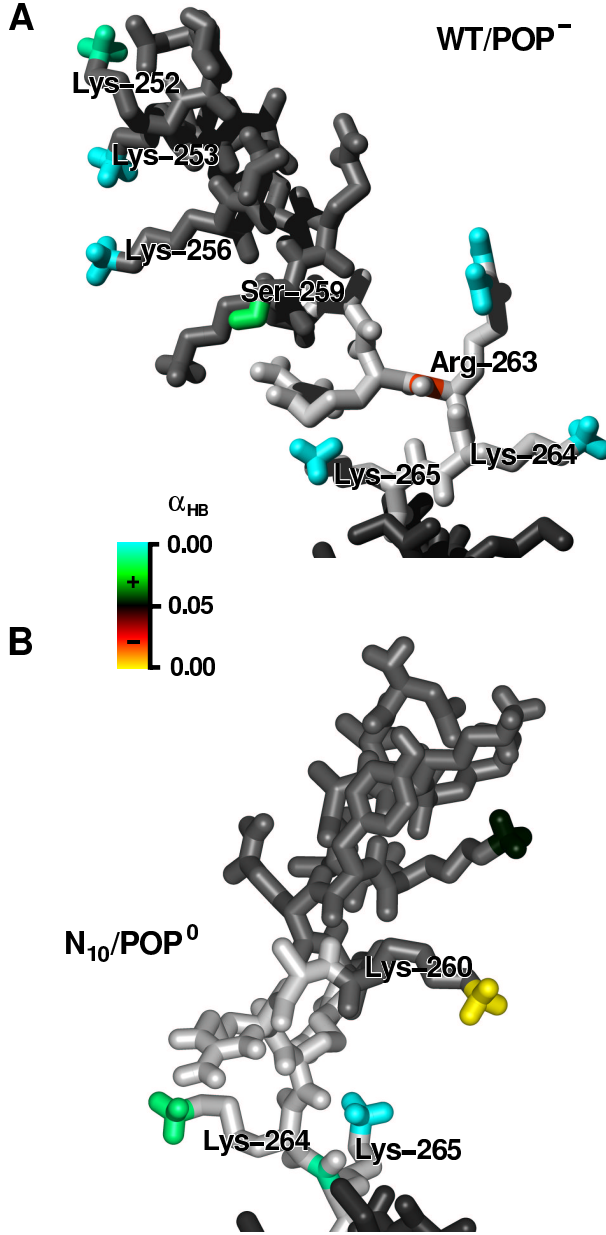


Figure 4.6: Color-coded significances (α -values) of hydrogen bond frequency differences of WT/POP⁻ (*top*) and N₁₀/POP⁰ (*bottom*), compared to WT/POP⁰, denoting significant ($p < 0.5$) increase (*green*), certain ($p \approx 0$) increase (*cyan*), significant decrease (*red*), and certain decrease (*yellow*), respectively, as determined by the bootstrap probability test. The structures are taken from the WT/POP⁻ and the N₁₀/POP⁰ annealing set, respectively, and are close to the respective average orientations. Atoms not involved in hydrogen bonding are shown in gray (H3 helix), light gray (linker), and dark gray (TM region).

The increased hydrogen bonding frequencies of the side-chain amino groups of the H3 helix residues Lys-253 and Lys-256, and the orientation of these residues (in particular that of Lys-253) in the pictured structure, suggest that these amino groups are pulled towards the lipid bilayer which could contribute to — or even cause — the increased average H3 helix tilt. In this view, the observed decreased helicity of residue Lys-265 could be determined by the tilt angle increase, rather than being its cause and rather than being determined by the reduced peptide penetration. Support for this interpretation comes from the fact that the observed peptide shift is rather small (unlike the shift observed between WT and N₁₀) and may thus not

fully explain the helicity decrease of residue Lys-265.

For N₁₀/POP⁰, the region of strongest hydrogen bonding is shifted from Lys-260 and Arg-262 towards Lys-264 and Lys-265 which closely matches the 5 Å vertical peptide shift induced by the prosequence and can explain the reduced helicity seen for Lys-265 (cf. Fig. 4.3 *C*). Due to the large peptide shift, the hydrogen bonds to the H3-proximal part of the linker are replaced by stronger ones to water molecules explaining the reduced helicity in that region.

Chapter 5

Summary

For the conformational coupling of SNARE-protein promoted membrane fusion, the mechanical properties of the juxtamembrane linker region of syntaxin-1A are essential but unknown. To characterize these properties of the linker in different lipid environments, we have performed a number of molecular dynamics (MD) simulations with explicit solvent and lipid environments. Particular focus was put on the stiffness that governs the bending of the linker as well as its average bending angle. To overcome the sampling problem, simulated annealing was applied. Apart from the wild type peptide, a mutant was also studied for which ten polar residues were appended to the C-terminus.

The bending properties of the linker were studied by calculating free energy landscapes for the tilt angle between the H3 helix of the core complex and the membrane normal from their equilibrium fluctuations. Particularly relevant for the conformational coupling scenario are the lower limits for the free energy required to tilt the H3 helix by 80°. These were estimated from annealing simulations. The results are summarized in Fig. 5.1. For the wild type, embedded within a neutral POPC/POPE bilayer, a value between 0.5 and 1.8 kcal/mol was obtained. Assuming that at least three SNARE complexes are involved in each fusion event¹⁶³ with two linkers each, we estimate that the linker stiffness reduces the fusion energy barrier ΔG^\ddagger (from membrane repulsion¹¹ and rigidity^{164,165}) by 3 to 8 kcal/mol. Assuming that the fusion rate r is proportional to the probability that the transition state is reached,

$$r \propto e^{-\Delta G^\ddagger/k_B T}, \quad (5.1)$$

with Boltzmann's constant $k_B = 1.99 \text{ kcal mol}^{-1}$ and the temperature $T = 300 \text{ K}$,

we estimate that this rate is correspondingly increased by two to five orders of magnitude.

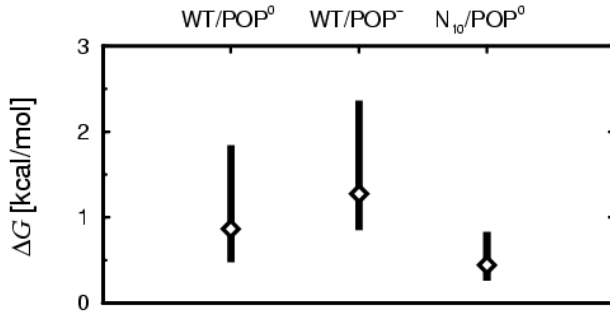


Figure 5.1: Free energies required to tilt the H3 helix of syntaxin-1A by 80° , as estimated from a number of annealing runs (Eq. 2.26). The bars indicate 95% confidence intervals.

We note that, strictly speaking, the notion of a stiffness implies a harmonic energy landscape for the H3 helix tilt. However, for the linker system at hand, and from the results of our simulations, this energy landscape is most likely more complicated and, e.g., composed of multiple, not necessarily harmonic, minima. Therefore, the given stiffness values provide an *effective* description, obtained from sampling many different linker conformations.

To check if the transmembrane helical domain of syntaxin-1A is anchored sufficiently tight within the bilayer, as required for the proposed fusion mechanism, position and tilt of the transmembrane helix were also studied. For the wild type, the equilibrium position of the helix is found to be shifted from a symmetrical position by $3 - 4 \text{ \AA}$ towards the C-terminal direction. As a result, as revealed by an analysis of hydrogen bond formation, and consistent with recent EPR measurements,⁷⁶ the linker region is deeply embedded within the polar headgroup region of the bilayer, partly even reaching into the hydrophobic core. This suggests, as reasoned,⁷⁶ that core complex formation leads to close proximity of the membranes with an inter-membrane distance well below the SNARE complex thickness.

The fluctuations of the transmembrane helix position in the direction of the membrane normal were found to be very small, implying a stiffness of $4 - 5 \text{ kcal mol}^{-1} \text{ \AA}^{-2}$ for the wild type. A force of 300 pN would thus move the helix by only 1 \AA . This result suggests that the peptide is anchored tightly enough within the membrane to withstand the high inter-membrane repulsion forces and to avoid that the peptide is pulled out of the membrane. Inversely, displacing the membrane anchor could transduce additional energy to the membrane by dragging out adjacent lipids towards the fusion contact area of the two bilayers. The amount of energy that is actually transmitted depends on the pulling force acting on the syntaxin anchor

during the initial stage of SNARE association which should therefore be studied in more detail.

For the conformational coupling model, the transmembrane helix must also resist larger tilting with respect to the bilayer normal. The stiffness coefficient of $70 \times \text{cal mol}^{-1} \text{deg}^{-2}$ obtained from our room temperature simulations is sufficiently large for that purpose. An average tilt of approx. 15° is seen for the transmembrane helix, which apparently compensates a mismatch of the hydrophobic sequence and the thickness of hydrophobic core of the bilayer,^{166–168} which could be fully spanned by a 17-residue TM helix.¹⁶⁹

The overall linker structure is found to be marginally helical. Relatively stable α -helical conformations are seen for the residues that are close to the H3 helix (Ala-261 and, partly, Arg-262) or to the transmembrane helix (Lys-265). The helicity decays towards the linker center. The bending stiffness of the linker is found to correlate with its helicity, albeit to a lesser extent than expected. A particularly strong correlation is seen for the helicity of the residues Ala-261 and Lys-265. The essential role of residue 261 could be tested experimentally by mutating the alanine to a glycine, which, due to its smaller side group (a single hydrogen), may be more flexible and show a less stable α -helical conformation. This effect is expected to decrease proteoliposome fusion efficiency.³ The configuration of the other linker residues Arg-262 – Lys-264 seems less important. Thus considerable bending stiffness can be achieved also without fully intact α -helix.

The simulations also show that the structure of the linker is strongly affected by its lipid environment. Charged lipids (POPS), for example, not only slightly increased the helicity of the linker and its stiffness, but also its average tilt angle. For the assumed 80° tilt, a corresponding increase in bending energy by approx. 0.4 kcal/mol is seen (Fig. 5.1, *mid*), which would enhance the fusion rate by a further order of magnitude as compared to the neutral bilayer. Note, however, that the changed electrostatic interaction between the approaching bilayers typically has a much stronger effect in this case.¹⁷⁰ Inversely, this interaction should simultaneously increase the deflection of the TM anchors and accordingly accelerate fusion.

The deep embedding of the linker within the polar region implies stronger hydrogen bonding between the peptide (mainly basic linker and H3 helix residues) and lipid molecules. On average, the wild type formed 3 – 6 of these bonds in the neutral bilayer. Acidic lipids increase the number of hydrogen bonds by a factor of two; this

may explain the measured decrease in lateral mobility of reconstituted syntaxin-1A/SNAP-25 complexes in the presence of acidic lipids.¹⁷¹

Quite unexpected was the strong effect caused by the addition of ten asparagine residues to the (distal) C-terminal end of the peptide. This shifted the transmembrane helix by 5 Å into a symmetrical position which, in contrast to the wild type, nicely matches the hydrophobicity profile of the membrane. As a result, the linker was exposed to a more hydrophilic environment, which could be checked by EPR experiments.⁷⁶ Accordingly, the helicity of the linker is found to be reduced and so is its bending stiffness. For the 80° tilt, a significantly decreased bending energy of 0.3 – 0.8 kcal/mol is found; the fusion efficiency is therefore expected to be reduced accordingly by roughly an order of magnitude. A further reduction of the fusion efficiency is expected due to the shifted transmembrane helix, which should increase the intermembrane distance by 5 Å. Since the inter-bilayer repulsion forces strongly decrease with increasing distance,¹¹ also a smaller deflection of the TM anchor is expected, which would further reduce fusion efficiency. We therefore suggest the Ala261Gly and N₁₀ mutants as experimental tests for the proposed SNARE fusion mechanism.

An opposite effect is expected for truncations of the TM domain. Here, the transmembrane domain should pull the linker region further towards the membrane interior, thereby reducing its accessibility to putative binding partners. In addition, its helicity could be further increased. We propose this as an explanation for the observed impaired binding of synaptobrevin, synaptotagmin,¹⁷² and α/β -SNAP,¹⁷³ to the cytosolic domain of syntaxin mutants with truncated TM domains.¹⁷⁴

Noting that cholesterol increases the thickness of the membrane,¹⁷⁵ the observed 15° tilt of the TM helix caused by a hydrophobic mismatch also could explain why syntaxin accumulates in cholesterol-rich regions.^{176,177} This could be tested by analyzing the distribution of syntaxin mutants with truncated TM domains, which is expected to be more uniform.

Due to the cholesterol-rich native environment, the hydrophobic mismatch between transmembrane helix and the membrane is likely reduced and, therefore, also its tilt with respect to the membrane normal.¹⁷⁸ The linker is expected to reside more deeply in the polar region; this effect could enhance the efficiency of the conformational coupling mechanism.

The hydrophobic mismatch could further facilitate the observed dimerization of

syntaxin TM domains.⁷² This may be tested experimentally by analyzing syntaxin dimerization in liposomes⁷² of varying composition; here the fraction of dimers is expected to anti-correlate with lipid chain length or cholesterol content, respectively.

An even higher TM helix tilt of 30° was obtained from spectroscopic studies for peptide mimics of the syntaxin TM domain.¹⁷⁹ The observed reduction of the TM helix tilt in the simulations may be attributed to the presence of the linker and the H3 segment, as these deeply penetrate the polar region of the membrane; thus, smaller tilts would be preferred because they imply less lipid perturbations¹¹³ in the headgroup region.

In summary, our simulations render the conformational coupling model physically plausible in quantitative terms. Our results suggest that, via conformational coupling, each linker can transfer mechanical energy of about 1 kcal/mol or larger to the membrane.

A few caveats are appropriate, however. Note that we have *not* shown that the transduced energy is actually used to bend opposing membranes in such a way as to reduce their mutual distance. Note also that possible effects on the mechanical properties of the linker due to the second, opposing membrane and due to membrane repulsion, are not described by our single membrane simulation. These will become increasingly important as fusion proceeds and might, e.g., include further stiffening of the linker due to dehydration of its environment. Alternatively, the stiffness might be *decreased* by the (unknown) forces that act on the TM helix during fusion and thereby pull the linker into a more hydrophilic, helix-destabilizing lipid/solvent interface environment. In addition, the pulling forces may directly destabilize an α -helical linker conformation by stretching backbone hydrogen bonds. Further work is required to elucidate the subsequent fusion steps at atomic detail.

Appendix

Table 5.1: Peptide sequence

H3	linker	TM	prosequence
DTKKAVKYQSK	ARRKK	IMIIICCVILGIIIASTIGGIFG	NNNNNNNNNN

Sequence of WT (H3 + linker + TM) and N₁₀ (H3 + linker + TM + prosequence) from the N- to the C-termini of the peptides. The one-letter code is explained in Tab. 5.2.

Table 5.2: Polarity of amino acids at neutral pH

name	3B-symbol	1B-symbol	polarity at pH 7
alanine	Ala	A	0
arginine	Arg	R	+
asparagine	Asp	N	↑
aspartate	Asn	D	−
cysteine	Cys	C	0
glutamine	Gln	Q	↑
glutamate	Glu	E	−
glycine	Gly	G	0
isoleucine	Ile	I	0
leucine	Leu	L	0
lysine	Lys	K	+
methionine	Met	M	0
phenylalanine	Phe	F	0
serine	Ser	S	↑
threonine	Thr	T	↑
tyrosine	Tyr	Y	↑
valine	Val	V	0

The signs denote nonpolar ('0'), polar ('↑'), positively charged ('+'), and negatively charged ('−'), respectively.

Danksagung

Zum Abschluss möchte ich all denen Personen danken, die zum Gelingen dieser Arbeit beigetragen haben.

Mein besonderer Dank gilt PD Dr. Helmut Grubmüller für die Möglichkeit, diese Arbeit in seiner Arbeitsgruppe für Theoretische Molekulare Biophysik am Max-Planck-Institut für biophysikalische Chemie in Göttingen durchzuführen. Ich bedanke mich für die ausgezeichnete Arbeitsatmosphäre, die erstklassige Betreuung und Unterstützung während meiner gesamten Promotionszeit, die zahlreichen Diskussionen und Anregungen, die entscheidende Impulse für meine Arbeit lieferten, und für seine Hilfe und Geduld beim Korrigieren der Arbeit. Ihm verdanke es auch, dass mir ein ausgezeichnetes Arbeitsumfeld samt hervorragender Rechnerausstattung zur Verfügung stand.

Großer Dank gebührt auch Frau Prof. Dr. Annette Zippelius, die die Doktormutterschaft übernahm und mir so ermöglichte, an der Georg-August-Universität in Göttingen zu promovieren.

Bedanken möchte ich mich bei allen derzeitigen und ehemaligen Mitgliedern unserer Gruppe für die gute Arbeitsatmosphäre, die vielen Diskussionen, Teerunden, und natürlich für das geduldige Korrekturlesen der Arbeit. Im einzelnen bedanke ich mich bei Dr. Rainer Böckmann, Peer Geisendorf, Dr. Bert de Groot, Evi Heinemann, Dr. Berthold Heymann, Oliver Lange, Jr-Hung Lin, Dr. Matthias Müller, Uwe Nolte, Gunnar Schröder, Oliver Slawik und Dr. Holger Wagner.

Für anregende Diskussionen über SNARE Proteine, Kommentare und/oder Korrekturlesen einer Veröffentlichung danke ich Dr. Dirk Fasshauer, Jaydev Jethwa, Prof.

Dr. Reinhardt Jahn, Prof. Dr. Erwin Neher, Dr. Martin Margittai, Prof. Dr. Dieter Langosch, Prof. Dr. José Rizo und Prof. Dr. Julio Fernandez. Für weitere wichtige Diskussionen danke ich Dr. Sebastian Domhof, Prof. Dr. Thomas Heimbürg, Prof. Dr. Bradley Efron, Prof. Dr. Udo Seifert, PD Dr. Jürgen Schlitter, Matthias Schneider und Dr. Karin Wieligmann.

I thank numerous subscribers of the *allstat* statistics mailing list for discussions on statistical problems: Dr. John Wittington, Cliff Lunneborg, Paul Johnson, Dr. Robert G. Newcombe, Dr. Cor Stolk, Paul Seed, Kevin McConway, Dr. Stephane Heritier, Dennis Chanter, and Kathy May. I further thank the following *allstat*'ers for valuable tips: Joachim Schwartz, Prof. Fortunato Pesarin, David McNulty, Julian Wells, Philip McShane, W. Mike Patefield, Quentin L. Burrell, Richard Lowry, Tony Swan, and Jay Warner.

Für die Finanzierung meiner Promotion danke ich der Volkswagen-Stiftung, und für die Bereitstellung zusätzlicher Rechenzeit dem PC² Paderborn, vertreten durch Axel Keller und Andreas Krawinkel.

Ein persönlicher Dank gilt vielen Freunden, insbesondere Dr. Michael Kersten und Michael Klein, und meiner Freundin Senta Kilb, die mir ein angenehmes und wichtiges Umfeld schufen.

Bibliography

- [1] B. Alberts, A. Johnson, J. Lewis, M. Raff, K. Roberts, and P. Walter, editors. *Molecular biology of the cell*. Garland Science, New York, 4th edition, 2002.
- [2] Y. A. Chen and R. H. Scheller. SNARE-mediated membrane fusion. *Nature Reviews*, 2(2):98–106, 2001.
- [3] J. A. McNew, T. Weber, D. M. Engelman, T. H. Söllner, and J. E. Rothman. The length of the flexible SNAREpin juxtamembrane region is a critical determinant of SNARE-dependent fusion. *Mol. Cell.*, 4(3):415–421, 1999.
- [4] J. A. McNew, T. Weber, F. Parlati, R. J. Johnston, T. J. Melia, T. H. Söllner, and J. E. Rothman. Close is not enough: SNARE-dependent membrane fusion requires an active mechanism that transduces force to membrane anchors. *J. Cell Biol.*, 150(1):105–117, 2000.
- [5] V. Knecht and H. Grubmüller. Mechanical coupling via the membrane fusion SNARE protein syntaxin-1a: a molecular dynamics study. *Biophys. J.*, 2003. in press.
- [6] W. F. van Gunsteren and H. J. C. Berendsen. Computer simulation of molecular dynamics: Methodology, applications, and perspectives in chemistry. *Angew. Chem. Int. Ed. Engl.*, 29:992–1023, 1990.
- [7] L. Stryer. *Biochemistry*. W. H. Freeman and co., New York, 3rd edition, 1988.
- [8] G. E. Schultz and R. H. Schirmer. *Principles of Protein Structure*. Springer, New York, 1979.
- [9] O. G. Mouritsen and M. Bloom. Mattress model of lipid-protein interactions in membranes. *Biophys. J.*, 46(2):141–153, 1984.
- [10] S. Leikin, V. A. Parsegian, D. C. Rau, and R. P. Rand. Hydration forces. *Annu. Rev. Phys. Chem.*, 44:369–395, 1993.

- [11] R. Lipowsky. Generic interactions of flexible membranes. In R. Lipowsky and E. Sackmann, editors, *Structure and Dynamics of Membranes*, pages 521–602, Amsterdam, 1995. Elsevier.
- [12] V. Malhotra, L. Orci, B. S. Glick, M. R. Block, and J. E. Rothman. Role of an N-ethylmaleimide-sensitive transport component in promoting fusion of transport vesicles with cisternae of the Golgi stack. *Cell*, 54(2):221–227, 1988.
- [13] L. Orci, V. Malhotra, M. Amherdt, T. Serafini, and J. E. Rothman. Dissection of a single round of vesicular transport — sequential intermediates for intercisternal movement in the Golgi stack. *Cell*, 56(3):357–368, 1989.
- [14] D. O. Clary and J. E. Rothman. Purification of 3 related peripheral membrane-proteins needed for vesicular transport. *J. Biol. Chem.*, 265(17):10109–10117, 1990.
- [15] N. Brose, A. G. Petrenko, T. C. Südhof, and R. Jahn. Synaptotagmin — a calcium sensor on the synaptic vesicle surface. *Science*, 256:1021–1025, 1992.
- [16] T. Söllner, S. W. Whitehart, M. Brunner, H. Erdjumentbromage, S. Geromanos, P. Tempst, and J. E. Rothman. SNAP receptors implicated in vesicle targeting and fusion. *Nature*, 362(6418):318–324, 1993.
- [17] A. J. Bean, R. Seifert, Y. A. Chen, R. Sacks, and R. H. Scheller. Hrs-2 is an ATPase implicated in calcium-regulated secretion. *Nature*, 385(6619):826–829, 1997.
- [18] Y. Fujita, H. Shirataki, T. Sakisaka, T. Asakura, T. Ohya, H. Kotani, S. Yokoyama, H. Nishioka, Y. Matsuura, A. Mizoguchi, R. H. Scheller, and Y. Takai. Tomosyn: a syntaxin-1-binding protein that forms a novel complex in the neurotransmitter release process. *Neuron*, 20(5):905–915, 1998.
- [19] J. M. Ilardi, S. Mochida, and Z. H. Sheng. Snapin: a SNARE-associated protein implicated in synaptic transmission. *Nat. Neurosci.*, 2(2):119–124, 1999.
- [20] R. Jahn. Sec1/munc18 proteins: mediators of membrane fusion moving to center stage. *Neuron*, 27(2):201–204, 2000.
- [21] G. F. Lao, V. Scheuss, C. M. Gerwin, Q. N. Su, S. Mochida, J. Rettig, and Z. H. Sheng. Syntaphilin: a syntaxin-1 clamp that controls SNARE assembly. *Neuron*, 25(1):191–201, 2000.
- [22] L. S. Chin, R. D. Nugent, M. C. Raynor, J. P. Vavalle, and L. Li. SNIP, a novel SNAP-25-interacting protein implicated in regulated exocytosis. *J. Biol. Chem.*, 275(2):1191–1200, 2000.

- [23] M. J. Clague and A. Herrmann. Membrane transport: deciphering fusion. *Current Biology*, 10(20):R750–R752, 2000.
- [24] K. A. Hu, J. Carroll, C. Rickman, and B. Davletov. Action of complexin on SNARE complex. *J. Biol. Chem.*, 277(44):41652–41656, 2002.
- [25] S. Ferro-Novick and R. Jahn. Vesicle fusion from yeast to man. *Nature*, 370:191–193, 1994.
- [26] J. C. Hay and R. H. Scheller. SNAREs and NSF in targeted membrane fusion. *Curr. Opin. Cell Biol.*, 9(4):505–512, 1997.
- [27] P. I. Hanson, J. E. Heuser, and R. Jahn. Neurotransmitter release — four years of SNARE complexes. *Current Opinion in Neurobiology*, 7:310–315, 1997.
- [28] J. M. Edwardson. Membrane fusion: all done with SNAREpins? *Curr. Biol.*, 8(11):R390–R393, 1998.
- [29] P. A. B. Harbury. Springs and zippers: coiled coils in SNARE-mediated membrane fusion. *Struct. Fold. Des.*, 6(12):1487–1491, 1998.
- [30] J. B. Bock and R. H. Scheller. SNARE proteins mediate lipid bilayer fusion. *Proc. Natl. Acad. Sci. U. S. A.*, 96(22):12227–12229, 1999.
- [31] R. Jahn and T. C. Südhof. Membrane fusion and exocytosis. *Annu. Rev. Biochem.*, 68:863–911, 1999.
- [32] P. Pountourios, R. J. Center, K. A. Wilson, B. E. Kemp, and B. Kobe. Evolutionary conservation of the membrane fusion machine. *IUBMB Life*, 48(2):151–156, 1999.
- [33] A. Mayer. Intracellular membrane fusion: SNAREs only? *Curr. Opin. Cell Biol.*, 11(4):447–452, 1999.
- [34] E. I. Pecheur, O. Maier, and D. Hoekstra. On the mechanism of intracellular membrane fusion: in search of the genuine fusion factor. *Biosci. Rep.*, 20(6):613–631, 2000.
- [35] A. T. Brunger. Structural insights into the molecular mechanism of Ca^{2+} -dependent exocytosis. *Curr. Opin. Neurobiol.*, 10(3):293–302, 2000.
- [36] B. R. Lentz, V. Malinin, M. E. Haque, and K. Evans. Protein machines and lipid assemblies: current views of cell membrane fusion. *Cur. Opin. in Struct. Biol.*, 10(5):607–615, 2000.

- [37] S. Mochida. Protein-protein interactions in neurotransmitter release. *Neurosci. Res.*, 36(3):175–182, 2000.
- [38] K. M. S. Misura, A. P. May, and W. I. Weis. Protein-protein interactions in intracellular membrane fusion. *Curr. Opin. Struct. Biol.*, 10(6):662–671, 2000.
- [39] R. C. Lin and R. H. Scheller. Mechanisms of synaptic vesicle exocytosis. *Annu. Rev. Cell Dev. Biol.*, 16:19–49, 2000.
- [40] A. Mayer. What drives membrane fusion in eukaryotes? *Trends Biochem.Sci.*, 26(12):717–723, 2001.
- [41] R. Jahn and H. Grubmüller. Membrane fusion. *Curr. Opin. Cell Biol.*, 14:488–495, 2002.
- [42] D. Bruns and R. Jahn. Molecular determinants of exocytosis. *Pflug. Arch. Eur. J. Phy.*, 443(3):333–338, 2002.
- [43] M. K. Bennett and R. H. Scheller. The molecular machinery for secretion is conserved from yeast to neurons. *Proc. Natl. Acad. Sci. U. S. A.*, 90(7):2559–2563, 1993.
- [44] C. Ungermann, K. Sato, and W. Wickner. Defining the functions of trans-SNARE pairs. *Nature*, 396(6711):543–548, 1998.
- [45] M. Tahara, J. R. Coorssen, K. Timmers, P. S. Blank, T. Whalley, R. Scheller, and J. Zimmerberg. Calcium can disrupt the SNARE protein complex on sea urchin egg secretory vesicles without irreversibly blocking fusion. *J. Biol. Chem.*, 273(50):33667–33673, 1998.
- [46] M. Bmert, P. R. Maycox, F. Navone, P. Decamilli, and R. Jahn. Synaptobrevin — an integral membrane-protein of 18000 daltons present in small synaptic vesicles of rat-brain. *EMBO J.*, 8(2):379–384, 1989.
- [47] G. A. Oyler, G. A. Higgins, R. A. Hart, E. Battenberg, M. Billingsley, F. E. Bloom, and M. C. Wilson. The identification of a novel synaptosomal-associated protein, SNAP-25, differentially expressed by neuronal subpopulations. *J. Cell Biol.*, 109(6):3039–3052, 1989.
- [48] M. K. Bennett, N. Calakos, K. G. Miller, and R. H. Scheller. Syntaxin — a synaptic protein implicated in docking of synaptic vesicles at presynaptic active zones. *Mol. Biol. Cell*, 3(Suppl. S):A3, 1992.
- [49] C. Montecucco and G. Schiavo. Structure and function of tetanus and botulinum neurotoxins. *Q. Rev. Biophys.*, 28:423–472, 1995.

- [50] J. Blasi, T. Binz, S. Yamasaki, E. Link, H. Niemann, and R. Jahn. Inhibition of neurotransmitter release by clostridial neurotoxins correlates with specific proteolysis of synaptosomal proteins. *J. Physiol.-Paris*, 88(4):235–241, 1994.
- [51] T. Söllner, M. K. Bennett, S. W. Whiteheart, R. H. Scheller, and J. E. Rothman. A protein assembly-disassembly pathway in vitro that may correspond to sequential steps of synaptic vesicle docking, activation, and fusion. *Cell*, 75:409–418, 1993.
- [52] D. Fasshauer, H. Otto, W. K. Eliason, R. Jahn, and A. T. Brünger. Structural changes are associated with soluble N-ethylmaleimide-sensitive fusion protein attachment protein receptor complex formation. *J. Biol. Chem.*, 272(44):28036–28041, 1997.
- [53] J. M. Canaves and M. Montal. Assembly of a ternary complex by the predicted minimal coiled-coil-forming domains of syntaxin, SNAP-25, and synaptobrevin — a circular dichroism study. *J. Biol. Chem.*, 273(51):34214–34221, 1998.
- [54] M. Margittai, D. Fasshauer, S. Pabst, R. Jahn, and R. Langen. Homo- and heterooligomeric SNARE complexes studied by site-directed spin labeling. *J. Biol. Chem.*, 276(16):13169–13177, 2001.
- [55] T. Xu, B. Rammner, M. Margittai, A. R. Artalejo, E. Neher, and R. Jahn. Inhibition of SNARE complex assembly differentially affects kinetic components of exocytosis. *Cell*, 99:713–722, 1999.
- [56] Z. P. Xia, Q. Zhou, J. L. Lin, and Y. C. Liu. Stable SNARE complex prior to evoked synaptic vesicle fusion revealed by fluorescence resonance energy transfer. *J. Biol. Chem.*, 276(3):1766–1771, 2001.
- [57] K. M. Fiebig, L. M. Rice, E. Pollock, and A. T. Brunger. Folding intermediates of SNARE complex assembly. *Nat. Struct. Biol.*, 6(2):117–123, 1999.
- [58] E. R. Chapman, S. An, N. Barton, and R. Jahn. SNAP-25, a t-SNARE which binds to both syntaxin and synaptobrevin via domains that may form coiled coils. *J. Biol. Chem.*, 269(44):27427–27432, 1994.
- [59] P. I. Hanson, R. Roth, H. Morisaki, R. Jahn, and J. E. Heuser. Structure and conformational changes in NSF and its membrane receptor complexes visualized by quick-freeze/deep-etch electron microscopy. *Cell*, 90(3):523–535, 1997.
- [60] M. A. Poirier, W. Xiao, J. C. Macosko, C. Chan, Y. K. Shin, and M. K. Bennett. The synaptic SNARE complex: a parallel four-stranded helical bundle. *Mol. Biol. Cell*, 9:482–, 1998.

- [61] L. Katz, P. I. Hanson, J. E. Heuser, and P. Brennwald. Genetic and morphological analyses reveal a critical interaction between the C-termini of two SNARE proteins and a parallel four helical arrangement for the exocytic SNARE complex. *EMBO J.*, 17(21):6200–6209, 1998.
- [62] T. Weber, B. V. Zemelman, J. A. McNew, B. Westermann, M. Gmachl, F. Parlati, T. H. Söllner, and J. E. Rothman. SNAREpins: minimal machinery for membrane fusion. *Cell*, 92(6):759–772, 1998.
- [63] W. Nickel, T. Weber, J. A. McNew, F. Parlati, T. H. Söllner, and J. E. Rothman. Content mixing and membrane integrity during membrane fusion driven by pairing of isolated v-SNAREs and t-SNAREs. *Proc. Natl. Acad. Sci. U. S. A.*, 96(22):12571–12576, 1999.
- [64] K. C. Sritharan, A. S. Quinn, D. J. Taatjes, and B. P. Jena. Binding contribution between synaptic vesicle membrane and plasma membrane proteins in neurons: an AFM study. *Cell Biol. Int.*, 22(9-10):649–655, 1998.
- [65] S. J. Cho, M. Kelly, K. T. Rognlien, J. A. Cho, J. K. H. Horber, and B. P. Jena. SNAREs in opposing bilayers interact in a circular array to form conducting pores. *Biophys. J.*, 83(5):2522–2527, 2002.
- [66] R. B. Sutton, J. A. Ernst, and A. T. Brünger. Crystal structure of the cytosolic C2A-C2B domains of synaptotagmin III: implications for Ca^{+2} -independent SNARE complex interaction. *J. Cell Biol.*, 147(3):589–598, 1999.
- [67] C. R. Cantor and P. R. Schimmel. *Biophysical Chemistry*. W. H. Freeman and Company, New York, 1980.
- [68] T. E. Creighton. *Proteins*. W. H. Freeman and Company, San Francisco, 1984.
- [69] C. Branden and J. Tooze. *Introduction to Protein Structure*. Garland Publishing, Inc., New York, 1991.
- [70] R. B. Sutton, D. Fasshauer, R. Jahn, and A. T. Brünger. Crystal structure of a SNARE complex involved in synaptic exocytosis at 2.4 Å resolution. *Nature*, 395:347–353, 1998.
- [71] N. Calakos and R. H. Scheller. Synaptic vesicle biogenesis, docking, and fusion: a molecular description. *Physiol. Rev.*, 76(1):1–29, 1996.
- [72] R. Laage, J. Rohde, B. Brosig, and D. Langosch. A conserved membrane-spanning amino acid motif drives homomeric and supports heteromeric assembly of presynaptic SNARE proteins. *J. Biol. Chem.*, 275(23):17481–17487, 2000.

- [73] C. A. Helm, J. N. Israelachvili, and P. M. McGuiggan. Role of hydrophobic forces in bilayer adhesion and fusion. *Biochemistry*, 31(6):1794–1805, 1992.
- [74] K. V. Shaitan, M. G. Mikhailyuk, K. M. Leont’ev, S. S. Saraikin, and A. A. Belyakov. Molecular dynamics of bending fluctuations of the elements of protein secondary structure. *Biofizika*, 47(3):411–419, 2002.
- [75] C. R. Cantor and P. R. Schimmel. *Biophysical Chemistry — Part II: Techniques for the study of biological structure and function*. W. H. Freeman and Company, New York, 1980.
- [76] D. H. Kweon, C. S. Kim, and Y. K. Shin. The membrane-dipped neuronal SNARE complex: A site-directed spin labeling electron paramagnetic resonance study. *Biochemistry*, 41(29):9264–9268, 2002.
- [77] R. Llinas, I. Z. Steinberg, and K. Walton. Relationship between presynaptic calcium current and postsynaptic potential in squid giant synapse. *Biophys. J.*, 33(3):323–351, 1981.
- [78] B. L. Sabatini and W. G. Regehr. Timing of neurotransmission at fast synapses in the mammalian brain. *Nature*, 384(6605):170–172, 1996.
- [79] B. L. Sabatini and W. G. Regehr. Timing of synaptic transmission. *Annu. Rev. Physiol.*, 61:521–542, 1999.
- [80] Y. Wang, I. Dulubova, J. Rizo, and T. C. Sudhof. Functional analysis of conserved structural elements in yeast syntaxin Vam3p. *J. Biol. Chem.*, 276(30):28598–28605, 2001.
- [81] P. H. Hünenberger and W. F. van Gunsteren. Empirical classical interaction functions for molecular systems. In W. F. van Gunsteren, P. K. Weiner, and A. J. Wilkinson, editors, *Computer Simulation of Biomolecular Systems, theoretical and experimental applications*, volume 3, pages 3–82. Kluwer/Escom, Dordrecht, The Netherlands, 1997.
- [82] M. Born and R. Oppenheimer. Zur Quantentheorie der Molekeln. *Ann. Phys. (Leipzig)*, 84:457, 1927.
- [83] J. A. McCammon, P. G. Wolynes, and M. Karplus. Picosecond dynamics of tyrosine side chains in proteins. *Biochemistry*, 18:927–942, 1979.
- [84] D. Van der Spoel, H. J. C. Berendsen, A. R. Van Buuren, E. Apol, P. J. Meulenhoff, A. L. T. M. Sijbers, and R. Van Drunen. *Gromacs User Man-*

- ual.* Nijenborgh 4, 9747 AG Groningen, The Netherlands. Electronic access: <http://md.chem.rug.nl/~gmx>, 1995.
- [85] M. Diraison, G. J. Martyna, and M. E. Tuckerman. Simulation studies of liquid ammonia by classical ab initio, classical, and path-integral molecular dynamics. *J. Chem. Phys.*, 111(3):1096–1103, 1999.
- [86] J. E. Lennard-Jones. *Proc. Roy. Soc. London Ser. A.*, 106:463, 1924.
- [87] B. R. Brooks, R. E. Bruccoleri, B. D. Olafson, D. J. States, S. Swaminathan, and M. Karplus. CHARMM: A program for macromolecular energy, minimization, and dynamics calculations. *J. Comp. Chem.*, 4(2):187–217, 1983.
- [88] W. F. van Gunsteren and H. J. C. Berendsen. *Gromos-87 manual*. BIOMOS b.v., Nijenborgh 4, 9747 AG Groningen, The Netherlands, 1987.
- [89] Scott J. Weiner, Peter A. Kollman, Dzong T. Nguyen, and David A. Case. An all atom force field for simulations of proteins and nucleic acids. *J. Comp. Chem.*, 7(2):230–252, 1986.
- [90] J. Tiradorives and W. L. Jorgensen. The OPLS force-field for organic and biomolecular systems. *Abstr. Pap. Am. Chem. Soc.*, 204:43–COMP, Part 1, 1992.
- [91] R. Lavery, K. Zakrzewska, and H. Sklenar. JUMNA (junction minimization of nucleic-acids). *Comput. Phys. Commun.*, 91(1-3):135–158, 1995.
- [92] P. Derreumaux, M. Dauchez, and G. Vergoten. The structures and vibrational frequencies of a series of alkanes using the SPASIBA force-field. *J. Mol. Struct.*, 295:203–221, 1993.
- [93] K. Rasmussen. How to develop force fields: An account of the emergence of potential energy functions for saccharides. *J. Mol. Struct.*, 395-396:81–90, 1997.
- [94] N. L. Allinger, Y. H. Yuh, and J. H. Lii. Molecular mechanics. The MM3 force fields for hydrocarbons. *J. Am. Chem. Soc.*, 111:8551–8566, 1989.
- [95] A. R. van Buuren, S. J. Marrink, and H. J. C. Berendsen. A molecular-dynamics study of the decane water interface. *J. Phys. Chem.*, 97(36):9206–9212, 1993.
- [96] S. Kirkpatrick, C. D. Gelatt, and M. P. Vecchi. Optimization by simulated annealing. *Science*, 220:671–680, 1983.
- [97] M. P. Allen and D. J. Tildesley. *Computer Simulation of Liquids*. Clarendon Press, Oxford, 1987.

- [98] Bronstein and Semendjajew. *Taschenbuch der Mathematik*. Harry Deutsch, Thun, Frankfurt (Main), 21th edition, 1981.
- [99] M. F. Perutz. Electrostatic effects in proteins. *Science*, 201(4362):1187–1191, 1978.
- [100] N. T. Southall, K. A. Dill, and A. D. J. Haymet. A view of the hydrophobic effect. *J. Phys. Chem. B*, 106(3):521–533, 2002.
- [101] D. Eisenberg and A. D. McLachlan. Solvation energy in protein folding and binding. *Nature*, 319(6050):199–203, 1986.
- [102] T. Ooi, M. Oobatake, G. Nemethy, and H. A. Scheraga. Accessible surface-areas as a measure of the thermodynamic parameters of hydration of peptides. *Proc. Natl. Acad. Sci. U. S. A.*, 84(10):3086–3090, 1987.
- [103] W. C. Still, A. Tempczyk, R. C. Hawley, and T. Hendrickson. Semianalytical treatment of solvation for molecular mechanics and dynamics. *J. Am. Chem. Soc.*, 112:6127–6129, 1990.
- [104] L. Wesson and D. Eisenberg. Atomic solvation parameters applied to molecular dynamics of proteins in solution. *Prot. Sci.*, 1:227–235, 1992.
- [105] C. A. Schiffer, J. W. Caldwell, R. M. Stroud, and P. A. Kollman. Inclusion of solvation free-energy with molecular mechanics energy — alanyl dipeptide as a test case. *Protein Sci.*, 1(3):396–400, 1992.
- [106] C. A. Schiffer, J. W. Caldwell, P. A. Kollman, and R. M. Stroud. Protein-structure prediction with a combined solvation free energy-molecular mechanics force-field. *Mol. Simul.*, 10(2-6):121, 1993.
- [107] P. Ferrara, J. Apostolakis, and A. Caflisch. Evaluation of a fast implicit solvent model for molecular dynamics simulations. *Proteins*, 46(1):24–33, 2002.
- [108] A. Hiltpold, P. Ferrara, J. Gsponer, and A. Caflisch. Free energy surface of the helical peptide y(meara)(6). *J. Phys. Chem. B*, 104(43):10080–10086, 2000.
- [109] K. Sharp. Incorporating solvent and ion screening into molecular-dynamics using the finite-difference Poisson-Boltzmann method. *J. Comput. Chem.*, 12(4):454–468, 1991.
- [110] B. Z. Lu, W. Z. Chen, C. X. Wang, and X. J. Xu. Protein molecular dynamics with electrostatic force entirely determined by a single Poisson-Boltzmann calculation. *Proteins*, 48(3):497–504, 2002.

- [111] G. Löffler. Poisson-Boltzmann calculations versus molecular dynamics simulations for calculating the electrostatic potential of a solvated peptide. *Theor. Chem. Acc.*, 101(1-3):163–169, 1999.
- [112] P. C. Biggin and M. S. P. Sansom. Interactions of alpha-helices with lipid bilayers: a review of simulation studies. *Biophys. Chem.*, 76(3):161–183, 1999.
- [113] N. Bental, A. Benshaul, A. Nicholls, and B. Honig. Free-energy determinants of alpha-helix insertion into lipid bilayers. *Biophys. J.*, 70(4):1803–1812, 1996.
- [114] P. Larocca, Y. Shai, and M. S. P. Sansom. Simulation studies of membrane-active peptides. *Biophys. J.*, 74(2):A304–A304, 1998.
- [115] O. Edholm and F. Jähnig. The structure of a membrane-spanning polypeptide studied by molecular-dynamics. *Biophys. Chem.*, 30(3):279–292, 1988.
- [116] J. Hermans, H. J. C. Berendsen, W. F. van Gunsteren, and J. P. M. Postma. A consistent empirical potential for water-protein interactions. *Biopolymers*, 23(8):1513–1518, 1984.
- [117] M. Berkowitz and J. A. Mccammon. Molecular-dynamics with stochastic boundary-conditions. *Chem. Phys. Lett.*, 90(3):215–217, 1982.
- [118] R. Kossmann. Entwicklung eines effektiven Randpotentials für Molekulardynamik-simulationen wäßriger Lösungen. Master’s thesis, Ludwig-Maximilians-Universität München, 1997.
- [119] W. Weber, P. H. Hünenberger, and J. A. McCammon. Molecular dynamics simulations of a polyalanine octapeptide under ewald boundary conditions: influence of artificial periodicity on peptide conformation. *J. Phys. Chem. B*, 104(15):3668–3675, 2000.
- [120] E. Neher. Biophysik von Sinnesrezeptoren. Universität Göttingen, 1998. Lecture notes.
- [121] W. Greiner, L. Neise, and H. Stöcker. *Thermodynamik und Statistische Mechanik*. Verlag Harri Deutsch, Thun and Frankfurt am Main, 2nd edition, 1993.
- [122] S. Nose. A molecular-dynamics method for simulations in the canonical ensemble. *Mol. Phys.*, 52(2):255–268, 1984.
- [123] W. G. Hoover. Canonical dynamics — equilibrium phase-space distributions. *Phys. Rev. A*, 31(3):1695–1697, 1985.

- [124] H. J. C. Berendsen, J. P. M. Postma, W. F. van Gunsteren, A. DiNola, and J. R. Haak. Molecular dynamics with coupling to an external bath. *J. Chem. Phys.*, 81(8):3684–3690, Oct. 1984.
- [125] W. F. van Gunsteren and M. Karplus. Effect of constraints on the dynamics of macromolecules. *Macromolecules*, 15(6):1528–1544, 1982.
- [126] B. Hess, H. Bekker, H. J. C. Berendsen, and J. G. E. M. Fraaije. LINCS: A linear constraint solver for molecular simulations. *J. Comp. Chem.*, 18:1463–1472, 1997.
- [127] S. Miyamoto and P. A. Kollman. SETTLE: An analytical version of the SHAKE and RATTLE algorithms for rigid water models. *J. Comp. Chem.*, 13:952–962, 1992.
- [128] K. A. Feenstra, B. Hess, and H. J. C. Berendsen. Improving efficiency of large time-scale molecular dynamics simulations of hydrogen-rich systems. *J. Comput. Chem.*, 20(8):786–798, 1999.
- [129] W. F. van Gunsteren, J. E. H. Köhler, and W. Saenger. On the difference between molecular conformation and hydrogen bonding in solution and in crystalline state. In *Proceedings of the XXXV-th Colloquium Protides of the Biological Fluids, Brussels, April 1987*, pages 489–492, Oxford, 1987. Pergamon.
- [130] W. F. van Gunsteren, S. R. Billeter, A. A. Eising, P. H. Hünenberger, P. Krüger, A. E. Mark, W. R. P. Scott, and I. G. Tironi. *Biomolecular Simulation: The GRO-MOS96 Manual and User Guide*. vdf Hochschulverlag AG an der ETH Zürich, Zürich, Switzerland, 1996.
- [131] P. P. Ewald. Die Berechnug optischer und elektrostatischer Gitterpotentiale. *Annalen der Physik*, IV(64):253–287, 1920.
- [132] T. Darden, D. York, and L. Pedersen. Particle mesh Ewald: an $N \cdot \log(N)$ method for Ewald sums in large systems. *J. Chem. Phys.*, 98:10089–10092, 1993.
- [133] K. Kholmurodov, W. Smith, K. Yasuoka, T. Darden, and T. Ebisuzaki. A smooth-particle mesh ewald method for dLpoly molecular dynamics simulation package on the Fujitsu VPP700. *J. Comput. Chem.*, 21(13):1187–1191, 2000.
- [134] M. Levitt and S. Lifson. Refinement of protein conformations using a macromolecular energy minimization procedure. *J. Mol. Biol.*, 46(2):269–279, 1969.
- [135] A. T. Brunger and P. D. Adams. Molecular dynamics applied to x-ray structure refinement. *Accounts Chem. Res.*, 35(6):404–412, 2002.

- [136] H. Frauenfelder, P. J. Steinbach, and R. D. Young. Conformational relaxation in proteins. *Chem. Scr.*, 29A:145–150, 1989.
- [137] B. G. Schulze, H. Grubmüller, and J. D. Evanseck. Functional significance of hierarchical tiers in carbonmonooxy myoglobin: conformational substates and transitions studied by conformational flooding simulations. *J. Am. Chem. Soc.*, 122(36):8700–8711, 2000.
- [138] R. C. van Schaik, W. F. van Gunsteren, and H. J. C. Berendsen. Conformational search by potential-energy annealing — algorithm and application to cyclosporine-A. *J. Comput.-Aided Mol. Des.*, 6(2):97–112, 1992.
- [139] R. C. van Schaik, H. J. C. Berendsen, A. E. Torda, and W. F. van Gunsteren. A structure refinement method based on molecular-dynamics in 4 spatial dimensions. *J. Mol. Biol.*, 234(3):751–762, 1993.
- [140] T. C. Beutler, A. E. Mark, R. C. van Schaik, P. R. Gerber, and W. F. van Gunsteren. Avoiding singularities and numerical instabilities in free-energy calculations based on molecular simulations. *Chem. Phys. Lett.*, 222(6):529–539, 1994.
- [141] T. C. Beutler and W. F. van Gunsteren. Molecular-dynamics free-energy calculation in 4 dimensions. *J. Chem. Phys.*, 101(2):1417–1422, 1994.
- [142] D. Byrne, J. Li, E. Platt, B. Robson, and P. Weiner. Novel algorithms for searching conformational space. *J. Comput.-Aided Mol. Des.*, 8(1):67–82, 1994.
- [143] Helmut Grubmüller. Predicting slow structural transitions in macromolecular systems: Conformational flooding. *Phys. Rev. E.*, 52:2893–2906, 1995.
- [144] Xiongwu Wu and Shaomeng Wang. Self-guided Molecular Dynamics simulation for efficient conformational search. *J. Phys. Chem. B*, 102:7238–7250, 1998.
- [145] Y. Pak and S. M. Wang. Folding of a 16-residue helical peptide using molecular dynamics simulation with Tsallis effective potential. *J. Chem. Phys.*, 111(10):4359–4361, 1999.
- [146] J. A. Rahman and J. C. Tully. Puddle-skimming: an efficient sampling of multidimensional configuration space. *J. Chem. Phys.*, 116(20):8750–8760, 2002.
- [147] Wolfgang Kabsch and Christian Sander. Dictionary of protein secondary structure: pattern recognition of hydrogen-bonded and geometrical features. *Biopolymers*, 22:2577–2637, 1983.

- [148] D. L. Beveridge and F. M. DiCapua. Free energy via molecular simulation: A primer. In W. F. van Gunsteren and P. K. Weiner, editors, *Computer Simulation of Biomolecular Systems: Theoretical and Experimental Applications*, volume 1, pages 1–26. ESCOM, Leiden, 1989.
- [149] W. F. van Gunsteren. Methods for calculation of free energies and binding constants. In W. F. van Gunsteren and P. K. Weiner, editors, *Computer Simulation of Biomolecular Systems: Theoretical and Experimental Applications*, volume 1, pages 27–59. ESCOM, Leiden, 1989.
- [150] E. Brunner. Angewandte Statistik, Teil I. Universität Göttingen, December 1998. Lecture notes.
- [151] E. B. Wilson. Probable inference, the law of succession, and statistical inference. *J. Am. Stat. Assoc.*, 22:209–212, 1927.
- [152] R. G. Newcombe. Two-sided confidence intervals for the single proportion: comparison of seven methods. *Stat. Med.*, 17(8):857–872, 1998.
- [153] B. Efron and R. J. Tibshirani. *An introduction to the bootstrap*. Chapman & Hall, New York, 1993.
- [154] F. C. Bernstein, T. F. Koetzle, G. J. B. Williams, E. F. Meyer, M. D. Brice, J. R. Rodgers, O. Kennard, T. Shimanouchi, and M. J. Tasumi. The protein data bank: A computer-based archival file for molecular structures. *J. Molec. Biol.*, 112:557, 1977.
- [155] MSI. InsightII user guide, October 1995.
- [156] R. Koradi, M. Billeter, and K. Wüthrich. Molmol: a program for display and analysis of macromolecular structures. *J. Mol. Graph.*, 14(1):51–55, 1996.
- [157] R. B. Gennis. *Biomembranes: Molecular Structure and Function*. Springer, New York, 1989.
- [158] O. Berger, O. Edholm, and F. Jähnig. Molecular dynamics simulations of a fluid bilayer of dipalmitoylphosphatidylcholine at full hydration, constant pressure, and constant temperature. *Biophys. J.*, 72(5):2002–2013, 1997.
- [159] D. P. Tieleman. *Theoretical studies of membrane models — Molecular dynamics of water, lipids and membrane proteins*. PhD thesis, Rijksuniversiteit Groningen, 1998.
- [160] D. P. Tieleman, 2000. electronic publication, <http://moose.bio.ucalgary.ca/-download.html,popc128a.pdb>.

- [161] F. Zhou and K. Schulten. Molecular-dynamics study of a membrane water interface. *J. Phys. Chem.*, 99(7):2194–2207, 1995.
- [162] G. Cevc and H. Richardsen. Lipid vesicles and membrane fusion. *Adv. Drug Deliv. Rev.*, 38(3):207–232, 1999.
- [163] Y. Y. Hua and R. H. Scheller. Three SNARE complexes cooperate to mediate membrane fusion. *Proc. Natl. Acad. Sci. USA*, 98(14):8065–8070, 2001.
- [164] L. V. Chernomordik and J. Zimmerberg. Bending membranes to the task — structural intermediates in bilayer fusion. *Curr. Opin. Struct. Biol.*, 5(4):541–547, 1995.
- [165] P. I. Kuzmin, J. Zimmerberg, Y. A. Chizmadzhev, and F. S. Cohen. A quantitative model for membrane fusion based on low-energy intermediates. *Proc. Natl. Acad. Sci. USA*, 98(13):7235–7240, 2001.
- [166] L. Y. Shen, D. Bassolino, and T. Stouch. Transmembrane helix structure, dynamics, and interactions: multi-nanosecond molecular dynamics simulations. *Biophys. J.*, 73(1):3–20, 1997.
- [167] J. A. Killian. Hydrophobic mismatch between proteins and lipids in membranes. *Biochim. Biophys. Acta-Rev. Biomembr.*, 1376(3):401–416, 1998.
- [168] S. Morein, J. A. Killian, and M. M. Sperotto. Characterization of the thermotropic behavior and lateral organization of lipid-peptide mixtures by a combined experimental and theoretical approach: effects of hydrophobic mismatch and role of flanking residues. *Biophys. J.*, 82(3):1405–1417, 2002.
- [169] S. Sharpe, K. R. Barber, C. W. M. Grant, D. Goodyear, and M. R. Morrow. Organization of model helical peptides in lipid bilayers: insight into the behavior of single-span protein transmembrane domains. *Biophys. J.*, 83(1):345–358, 2002.
- [170] D. Andelman. Electrostatic properties of membranes: The Poisson-Blotzmann theory. In R. Lipowsky and E. Sackmann, editors, *Structure and Dynamics of Membranes*, pages 603–642. Elsevier, Amsterdam, 1995.
- [171] M. L. Wagner and L. K. Tamm. Reconstituted syntaxin1-a/SNAP-25 interacts with negatively charged lipids as measured by lateral diffusion in planar supported bilayers. *Biophys. J.*, 81(1):266–275, 2001.
- [172] E. R. Chapman, P. I. Hanson, S. An, and R. Jahn. Ca^{2+} regulates the interaction between synaptotagmin and syntaxin 1. *J. Biol. Chem.*, 270:23667–23671, 1995.

- [173] Y. Kee, R. C. Lin, S. C. Hsu, and R. H. Scheller. Distinct domains of syntaxin are required for synaptic vesicle fusion complex-formation and dissociation. *Neuron*, 14(5):991–998, 1995.
- [174] J. L. Lewis, M. Dong, C. A. Earles, and E. R. Chapman. The transmembrane domain of syntaxin 1a is critical for cytoplasmic domain protein-protein interactions. *J. Biol. Chem.*, 276(18):15458–15465, 2001.
- [175] R. Rukmini, S. S. Rawat, S. C. Biswas, and A. Chattopadhyay. Cholesterol organization in membranes at low concentrations: effects of curvature stress and membrane thickness. *Biophys. J.*, 81(4):2122–2134, 2001.
- [176] L. H. Chamberlain, R. D. Burgoyne, and G. W. Gould. SNARE proteins are highly enriched in lipid rafts in PC12 cells: implications for the spatial control of exocytosis. *Proc. Natl. Acad. Sci. USA*, 98(10):5619–5624, 2001.
- [177] T. Lang, D. Bruns, D. Wenzel, D. Riedel, P. Holroyd, C. Thiele, and R. Jahn. SNAREs are concentrated in cholesterol-dependent clusters that define docking and fusion sites for exocytosis. *EMBO J.*, 20(9):2202–2213, 2001.
- [178] J. H. Ren, S. Lew, Z. W. Wang, and E. London. Transmembrane orientation of hydrophobic alpha-helices is regulated both by the relationship of helix length to bilayer thickness and by the cholesterol concentration. *Biochemistry*, 36(33):10213–10220, 1997.
- [179] D. Langosch, J. M. Crane, B. Brosig, A. Hellwig, L. K. Tamm, and J. Reed. Peptide mimics of SNARE transmembrane segments drive membrane fusion depending on their conformational plasticity. *J. Mol. Biol.*, 311(4):709–721, 2001.

LEBENS LAUF

Name	Volker Knecht
Geburtsdatum	06.01.1970
Geburtsort	Kaiserslautern
Staatsangehörigkeit	deutsch
Familienstand	ledig
Grundschule	1976 – 1980 in Niederkirchen
Gymnasium	1980 – 1989 Staatliches Gymnasium an der Burgstraße, Kaiserslautern
Allgemeine Hochschulreife	Mai 1989
Wehrdienst	1989 – 1990 in Kusel
Studium der Physik	WS 1990/91 bis WS 1996/97 Universität Kaiserslautern
Diplomarbeit	Dezember 1995 – Dezember 1996 Theoretische Physik Thema: “Computergestützte Renormierungsgruppenuntersuchung des zweidimensionalen xy-Modells”
Diplom	Februar 1997
Praktika	September/Okttober 1995 BASF Ludwigshafen, Computeranalyse kristallographischer Daten Juni – Dezember 1997 TECMATH GmbH Kaiserslautern, Automatisierung von Software-Tests, Softwareentwicklung
Berufliche Tätigkeit	Januar 1998 – Juli 1999 LMS Durability Technologies GmbH, Kaiserslautern. Softwareentwicklung
Dissertation	seit August 1999
Göttingen, 14.02.2003	